Immunotherapy-based targeting of senescent cells

Doctoral thesis

to obtain a doctorate (PhD)

from the Faculty of Medicine

of the University of Bonn

Yushuang Deng
from Sichuan, China
2025

Written with authorization of
the Faculty of Medicine of the University of Bonn

First reviewer: PD Dr. Dan Ehninger
Second reviewer: Prof. Dr. med. Johannes Oldenburg

Day of oral examination: 10.02.2025

From the German Centre for Neurodegenerative Diseases (DZNE e.V.)

Table of Contents

List of abbreviations

AD	Alzheimer's disease
ADC	Antibody-drug conjugate
AGA	N(4)-(beta-N-acetylglucosaminyl)-L-asparaginase
ANOVA	Analysis of variance
APC	Allophycocyanin
AST	Astrocytes
B2MG	Beta-2-microglobulin
Bcl-2	B-cell lymphoma 2
BSA	Bovine serum albumin
CAR	Chimeric antigen receptor
CDK	Cyclin-Dependent Kinase
CDKN	Cyclin-dependent kinase inhibitor
CS	Cellular senescence
CT	Cycle threshold
CYB5R1	Cytochrome b5 reductase 1
CYP	Cytoplasmic
DAP10	DNAX-activating protein 10
DAPI	4′,6-diamidino-2-phenylindole
DEP	Differentially expressed protein
DMEM	Dulbecco’s modified Eagle’s medium
DMSO	Dimethyl sulfoxide
DNA	Deoxyribonucleic acid
DPP4	Dipeptidyl-peptidase 4
DTT	Dithiothreitol
E: T	Effector-to-target
ECM	Extracellular matrix
EDTA	Ethylenediamine tetraacetic acid
EF1α	Elongation factor 1-alpha
EPO	Epoxomicin
ETO	Etoposide

FBS	Fetal bovine serum
FC	Fold change
FCM	Flow cytometry
FDR	False discovery rate
FITC	Fluorescein isothiocyanate
FMR1	Fragile X messenger ribonucleoprotein 1
GAPDH	Glyceraldehyde-3-phosphate dehydrogenase
GLB1	Galactosidase beta 1
GO	Gene Ontology
GPX7	Glutathione peroxidase 7
H2O2	Hydrogen peroxide
H60	Histocompatibility antigen 60
HBSS	Hanks' Balanced Salt Solution
HEK293T	Human embryonic kidney 293T
HPM	Human Proteome Map
HRP	Horseradish peroxidase
HUVEC	Human umbilical vein endothelial cell
IAA	Iodoacetic acid
ICAM1	Intercellular adhesion molecule-1
IL	Interleukin
IRES	Internal ribosomal entry site
ITR	Inverted terminal repeat
L-R	Ligand-receptor
LC-MS/MS	Liquid chromatography-tandem Mass Spectrometry
MEFs	Mouse embryonic fibroblasts
MFI	Mean-fluorescence intensity
MICA	MHC class I chain-related proteins A
mTOR	Mammalian Target of Rapamycin
Mult1	Murine UL16-binding-protein-like transcript 1
Neo	Neomycin resistance
NHLF	Human lung fibroblast
NKG2D	Natural killer group 2D

NKG2DLs	Natural killer group 2D ligands
OIS	Oncogene-induced senescence
PBS	Phosphate-buffered saline
PCA	Principal component analysis
PE	Phycoerythrin
PFA	Paraformaldehyde
PI3K	Phosphoinositide 3-Kinase
PLXNA1	Plexin A1
PLXNA3	Plexin A3
PSMs	Peptide spectral matches
PTK7	Protein tyrosine kinase 7
qPCR	Quantitative real-time PCR
Rae1	Retinoic acid early transcript 1
rhIL-2	Recombinant human IL-2
ROS	Reactive oxygen species
RS	Replicative senescence
SA-β-gal	Senescence associated-β-galactosidase
SAHF	Senescence-associated heterochromatin foci
SASP	Senescence-associated secretory phenotype
SCAMP4	Secretory carrier membrane protein 4
SD	Standard deviation
SDS	Sodium dodecyl sulfate
SDS-PAGE	Sodium dodecyl-sulfate polyacrylamide gel electrophoresis
SEM	Standard error of the mean
SIPS	Stress-induced premature senescence
T2A	Thosea asigna virus 2A
TEMED	Tetramethylethylenediamine
TFA	Trifluoroacetic Acid
uPAR	Urokinase plasminogen activator receptor
WT	Wild type
ZsGreen	Zoanthus sp. green fluorescent protein

1. Introduction

1.1 Aging and cellular senescence

1.1.1 The hallmarks of aging

In multicellular organisms, aging is characterized by a gradual and progressive decline at molecular, cellular, tissue, and organismal levels, serving as the primary risk factor for various chronic diseases (Niccoli and Partridge 2012), including cancer (Falandry et al. 2014), cardiovascular diseases (North and Sinclair 2012), and neurodegenerative disorders (Guo et al. 2022, Kritsilis et al. 2018). In mammals, this age-related degeneration gives rise to well-recognized pathologies, such as sarcopenia (Doherty 2003, McCormick and Vasilaki 2018), atherosclerosis (Tyrrell and Goldstein 2021), heart failure (Triposkiadis et al. 2019), osteoporosis (Jakob et al. 2014), diabetes (Longo et al. 2019), pulmonary diseases (Cho and Stout-Delgado 2020), renal failure (O'Sullivan et al. 2017), and neurodegeneration such as Alzheimer's disease (AD) and Parkinson's disease (Hou et al. 2019). Although the biological causes of aging and underlying mechanisms remain largely unknown, a multitude of studies over the last several years have identified common cellular and molecular signatures associated with aging and age-related diseases (López-Otín et al. 2023, Mc Auley et al. 2017, Titorenko 2019). Collectively, the aging process is characterized by twelve candidate hallmarks comprising genomic instability, telomere attrition, epigenetic alterations, deregulated nutrient-sensing, mitochondrial dysfunction, stem cell exhaustion, altered intercellular communication, loss of proteostasis, chronic inflammation, dysbiosis, disabled macroautophagy, and cellular senescence (CS) (López-Otín et al. 2023). These hallmarks are highly and intricately interdependent. For instance, genomic instability is linked to mitochondrial dysfunction and CS, while epigenetic alterations crosstalk to genomic instability. It remains a challenge to dissect their relative and individual contributions to aging. Accordingly, each hallmark offers a potential avenue for investigating the aging process and developing strategies to target aging and age-related pathologies. In this thesis, we focus on one of these hallmarks: CS.

1.1.2 Cellular senescence

CS is an evolutionarily conserved state of permanent cell cycle arrest accompanied by substantial macromolecular changes (Hayflick and Moorhead 1961, Kuilman et al. 2010).

Primary senescence can be initiated by a wide range of intrinsic and extrinsic cellular stressors, including DNA damage, hypoxia, mitochondrial dysfunction, oncogene activation, and nutrient deprivation. Furthermore, secondary senescence can be triggered by various extracellular mediators of inflammation and fibrosis (Admasu et al. 2021, Kuilman et al. 2010). The accumulation of damage stimulates the activities of cyclin-dependent kinase inhibitors p16Ink4a and/or p53/p21$^{Cip1/Waf1}$, which antagonize cyclin-dependent kinases to block cell cycle progression (Hernandez-Segura et al. 2018, Purvis et al. 2012, Sherr et al. 2016). An additional notable trait exhibited by senescent cells is the senescence-associated secretory phenotype (SASP), encompassing the secretion into the extracellular space of a broad spectrum of proteins, such as chemokines, growth factors, inflammatory cytokines, and matrix metalloproteases (Coppé et al. 2010, Tchkonia et al. 2013). The SASP can be both beneficial and detrimental. Transient SASP favors tissue remodeling during embryonic development and promotes the clearance of senescent cells by driving macrophage infiltration (Demaria et al. 2014, Muñoz-Espín et al. 2013, Storer et al. 2013). In contrast, persistent SASP has pro-inflammatory effects on the microenvironment, adversely affecting neighboring cells and contributing to marked tissue dysfunction (Childs et al. 2015).

CS exerts a range of effects on both physiological and pathological processes (Muñoz-Espín and Serrano 2014). Physiologically, CS contributes to tissue repair, where senescent cells induce localized fibrosis and attract immune cells to remove damaged cells, thus aiding in wound healing. In this scenario, senescence acts as a temporally beneficial compensatory response to damage. In addition, CS also serves as a tumor suppressor mechanism (He and Sharpless 2017). Pathologically, the accumulation of senescent cells is implicated in multiple age-related pathologies and phenotypes, such as cancer formation, osteoarthritis, impaired metabolic function, fibrosis, cardiac dysfunction, neurodegeneration, and infection (Childs et al. 2015, He and Sharpless 2017).

Senescence can be triggered by various stimuli, resulting in different types: telomere-dependent replicative senescence (RS), oncogene-induced senescence (OIS), and stress-induced premature senescence (SIPS), the latter arising from oxidative stress, genotoxic stress, proteotoxic stress, and others (Mohamad Kamal et al. 2020). While CS predominantly affects fibroblasts, endothelial cells, and immune cells (Gabai et al. 2023, Xu et al. 2022), post-mitotic or slowly proliferative cells, including brain cells (Sah et al.

2021) and heart cells (Anderson et al. 2019), can also undergo senescence in response to stressors. Notably, senescent cells exhibit significant heterogeneity and dynamism, influenced predominantly by their microenvironmental contexts (Casella et al. 2019, Hernandez-Segura et al. 2017).

1.1.3 The role of cellular senescence in aging

The excessive accumulation of senescent cells has been reported in tissues of aged humans (Dimri et al. 1995, Tchkonia et al. 2013), nonhuman primates (Herbig et al. 2006, Jeyapalan et al. 2007), and rodents (Baker et al. 2016, Wang et al. 2009). Of note, in humans, senescent cells accumulate in various tissues at different rates, ranging from a 2- to 20-fold increase when comparing healthy individuals younger than 35 years to those older than 65 years (Tuttle et al. 2020). This accumulation of senescent cells may be due to an increased rate of senescent cell generation and/or a decreased rate of clearance, potentially resulting from the compromised immune system (Song et al. 2020).

Several transgenic mouse models have been developed to explore the role of CS in aging. One notable model is the INK/ATTAC model, in which a suicide gene is inserted into the promoter of the $p16^{Ink4a}$ gene, enabling the elimination of p16-positive cells (Baker et al. 2011). An extension of lifespan as well as improvements in the age-related deterioration of several organs, including the brain, kidney, and heart, have been achieved by clearance of senescent cells using this mouse model (Baker et al. 2011), which strongly substantiated that CS can drive aging-associated changes *in vivo* and facilitate the development of a range of aging-related disorders. However, genetic tools used in mouse models are not translatable to humans.

Since senescent cells are resistant to intrinsic and extrinsic apoptosis, an emerging strategy to remove senescent cells potentially applicable to human treatments is based on senolytics. These drugs specifically target senescent cells by inducing apoptosis of senescent cells (Zhang et al. 2023). These senolytics mainly target the senescent cell anti-apoptotic pathways (SCAPs), including B-cell lymphoma 2 (Bcl-2) family proteins, heat shock protein 90, p53, and the phosphatidylinositol 3-kinase (PI3K)/protein Kinase B (Akt)/ mammalian target of rapamycin (mTOR) pathway (Chaib et al. 2022, Kirkland and Tchkonia 2017). Another pharmaceutical approach that counters the effects of senescent cells is based on senomorphics, which suppress the SASPs, such as inhibitors of IkB

kinase (IKK) and nuclear factor kappa B (NF-κB), scavengers of free radicals, and Janus kinase (JAK) pathway inhibitors (Zhang et al. 2023). In preclinical experiments, senolytic drugs have shown potential in mitigating several aging-associated health outcomes, such as atherosclerosis (Roos et al. 2016), pulmonary dysfunction (Schafer et al. 2017), osteoarthritis (Jeon et al. 2017), cancers (Baker et al. 2016), and cognitive decline (Zhang et al. 2019). In human clinical trials, senolytics have been demonstrated to improve physical dysfunction in patients with idiopathic pulmonary fibrosis (Justice et al. 2019). These findings underscore that senescent cells may represent a promising target for the development of new therapeutics and/or preventatives for age-related diseases. However, the pharmacological approaches outlined above are not specific to senescent cells and are, hence, associated with off-target effects, which limits their translational potential (Chaib et al. 2022).

1.2 Potential of immunotherapies based on senescent cell elimination

1.2.1 Antibody-based immunotherapies

To minimize the off-target effects of senotherapeutics, a promising alternative lies in immunotherapy-based targeting of senescence-specific surface antigens (senoantigens). For instance, a humanized antibody against dipeptidyl-peptidase 4 (DPP4) (Kim et al. 2017) and an antibody-drug conjugate (ADC) directed at beta-2-microglobulin (B2MG) (Poblocka et al. 2021) have been demonstrated *in vitro* to eliminate senescent cells expressing these antigens. Moreover, a vaccine designed against glycoprotein nonmetastatic melanoma protein B (GPNMB), another senescence-associated protein, was reported to improve age-related pathological changes in progeroid mice through the clearance of senescent cells (Suda et al. 2021).

1.2.2 Chimeric antigen receptor (CAR)-T cell therapy

In addition to these antibody-based immunotherapies, increasing evidence underscores the role of immune cells, including cytotoxic T cells, in the immunological surveillance of senescent cells in the context of cancer (Ovadya et al. 2018, Sagiv and Krizhanovsky 2013). Owing to their cytotoxic potency, effective migratory capacity, self-expansion, and memory abilities, T cells genetically engineered to express artificial receptors that target specific antigens on cancer cells, called CAR-T cells, have received FDA approval for the

treatment of various hematological malignancies, including lymphomas, certain leukemias, and multiple myeloma (Baker et al. 2023). The success of CAR-T cell therapy lies in the coupling of the intrinsic specificity of an antibody within a CAR and the efficient endogenous cytotoxicity potency of T cells. With these advantages that are unrivalled by current small-molecule approaches, CAR-T cell therapy is showing promise to treat other diseases beyond cancer, including autoimmune and inflammatory conditions such as systemic lupus erythematosus, chronic infections, and cardiac fibrosis (Baker et al. 2023). Strikingly, recent advances have demonstrated that CAR-T cells could also target senescent cells. The initial senolytic CAR target, urokinase plasminogen activator receptor (uPAR), was identified by RNA-sequencing analyses of three senescence models: chemotherapy-induced senescence in mouse lung adenocarcinoma cells, OIS in mouse hepatocytes, and RS in mouse hepatic stellate cells. Adoptive transferring of uPAR CAR-T cells not only prolonged survival in a mouse model of lung adenocarcinoma undergoing oncotherapy-induced senescence, but also mitigated liver fibrosis triggered by chemical or dietary factors (Amor et al. 2020). This observation provides the first proof-of-principle basis for the application of CAR-T cell immunotherapy in managing senescence-associated diseases.

1.3 Senescence surface markers as potential targets for immune-based senotherapy

Although CAR-T cells exhibit potential senolytic activity, the effectiveness of senolytic CAR-T cell therapy mainly depends on accurately detecting and identifying senescent cells in tissues based on unique and senescence-specific cell surface markers, thereby promising to offer heightened precision for *in vivo* senescent cell elimination while plausibly limiting the side effects on the normal, non-senescent cells.

1.3.1 Classic markers of cellular senescence

Senescent cells display a distinct enlarged and flattened morphology, linked to the expansion of the endoplasmic reticulum and the unfolded protein response (Druelle et al. 2016). At the molecular level, senescent cells are routinely characterized by the expression of several biomarkers. The most commonly used markers are upregulated negative cell cycle regulators, including p16 and/or p21/p53, which inhibit cyclin-

dependent kinase CDK4/6 or CDK2, simultaneously preventing retinoblastoma (RB) phosphorylation and thereby impeding the progression of the cell cycle from G1 to S phase (González-Gualda et al. 2021, Mijit et al. 2020, Sherr et al. 2016).

Increased activity of lysosome β-galactosidase (β–Gal), recognized as senescence associated-β-galactosidase (SA-β-gal), which is encoded by the gene Galactosidase beta 1 (GLB1) and detectable by staining at PH 6 in senescent cells, distinguishes senescent from healthy cells (Lee et al. 2006). Another senescence marker related to lysosomal dysfunction is the accumulation of lipofuscin in lysosomes, which is correlated with Bcl-2 stimulation (Georgakopoulou et al. 2013, González-Gualda et al. 2021).

A hallmark of DNA damage in senescent cells is the γ-H2AX, formed by the phosphorylation of histone protein H2AX at Ser139, playing a role in recruiting DNA repair molecules (Rodier et al. 2011). Additionally, CS is associated with alterations in chromatin features, such as chromatin condensation and the formation of senescence-associated heterochromatin foci (SAHFs) (Zhang et al. 2007). The secretion of components, such as pro-inflammatory cytokines Interleukin 1β (IL-1β), IL-6, and tumor necrosis factor-alpha (TNF-α), has been robustly observed in various senescent cell models, contributing to local and systemic aging-related dysfunctions and diseases (Coppé et al. 2010).

1.3.2 Novel markers of cellular senescence

Recent advances in unbiased RNA-sequencing-based transcriptome analyses (Casella et al. 2019, Hernandez-Segura et al. 2017) and mass spectrometry (MS)-based proteome analyses (Althubiti et al. 2014, Basisty et al. 2020) have substantially expanded our understanding of CS expression profiles. Single-cell transcriptome analyses of mouse embryonic fibroblasts (MEFs) revealed six subpopulations, each displaying unique senescence features, reflecting distinct cellular fates within senescent MEFs. Network analysis further highlighted Homeobox D8 (HOXD8) as a potential novel regulator of MEFs senescence (Chen et al. 2020). Additionally, using RS-induced human fibroblasts (HCA2) and single senescent cell sequencing, heterogeneity was demonstrated to occur in senescent cells induced by telomere erosion (Tang et al. 2019). To identify robust, shared markers of senescence, RNA-sequencing analyses were performed across eight diverse models of senescence triggered in human diploid fibroblasts (WI-38, IMR-90) and endothelial cells by replicative exhaustion, ionizing radiation, doxorubicin treatment, or

Harvey rat sarcoma virus (HRAS) oncogene expression. The intersection of the altered transcriptomes identified 50 RNAs consistently elevated and 18 RNAs consistently reduced across all senescence models (Casella et al. 2019). Furthermore, analysis of individual cells has revealed cell-to-cell variability following senescence induction and suggested that single markers are inadequate to identify senescent cells *in vivo* (Wiley et al. 2017).

Proteomics analyses across different types of senescence have uncovered 107 novel protein markers of CS with ten validated (DEP1, NTAL, EBP50, STX4, VAMP3, ARMX3, B2MG, LANCL1, VPS26A and PLD3) (Althubiti et al. 2014). This study suggested that a combination of these proteins could be used to specifically recognize senescent cells in culture. Moreover, with focus on CS surface markers, several molecules, including intercellular adhesion molecule-1 (ICAM1), DPP4, and secretory carrier membrane protein 4 (SCAMP4), were identified through screening of cell surface-associated proteins preferentially expressed in human RS fibroblasts (Kim et al. 2018, 2017, Mrazkova et al. 2018).

1.3.3 NKG2D receptor and ligands

In this thesis, we propose a class of well-characterized surface molecules differentially expressed in senescent cells, Natural killer group 2D (NKG2D) ligands (NKG2DLs), as a general hallmark of senescence. NKG2D is a type II transmembrane receptor expressed by NK cells and some subsets of T cells (Prajapati et al. 2018). The expression of its ligands is increased in several tumor cell types and virus-infected cells in response to cellular stressors while being generally absent in healthy cells (González et al. 2008). Notably, a consistent increase in NKG2DLs has been observed in a variety of senescence models originating from diverse cell types and inducers (Kim et al. 2008, Krizhanovsky et al. 2008, Sagiv et al. 2016, Soriani et al. 2009, Yang et al. 2023). These models include replicative senescent human fibroblasts (Krizhanovsky et al. 2008, Sagiv et al. 2016) and human umbilical vein endothelial cells (HUVECs) (Kim et al. 2008), oncogene-induced senescent human fibroblasts (Sagiv et al. 2016), chemotherapy-induced senescent human and mouse fibroblasts (Kim et al. 2017, Krizhanovsky et al. 2008, Yang et al. 2023), ultraviolet irradiation-triggered senescent mouse fibroblasts (Yang et al. 2023), and chemotherapy-induced senescent human hepatic stellate cells (Krizhanovsky et al. 2008,

Sagiv et al. 2016). Moreover, in elderly human individuals *in vivo*, senescent dermal fibroblasts exhibit high expression levels of NKG2DLs (Hasegawa et al. 2023). Notably, these ligands have been reported to be implicated in the immune surveillance by NK cells expressing the NKG2D receptor (Sagiv et al. 2016).

1.3.4 Challenges in the identification of senescent cells with current cellular senescence markers

Despite these critical advancements in the field of senescence biomarkers, translating these findings into effective senotherapeutic strategies remains challenging. The heterogeneity and dynamic nature of CS indicate that the utility of individual markers for their conclusive identification of senescent cells is limited (Casella et al. 2019, Hernandez-Segura et al. 2017). Additionally, most current senescence markers are not cell surface molecules, restricting their accessibility from the external environment. The comprehensive identification of surface proteins associated with CS is further constrained by the low solubility and abundance of cell membrane proteins. Moreover, the current repertoire of senescence surface markers established from models with limited cellular origins (e.g., primary fibroblasts), types of senescence-inducing stimuli, and species complicates the generalization of these markers across different contexts.

1.4 Aims of the study

Leveraging literature-supported senescence surface markers, the primary aim of this thesis was to develop an *in vitro* NKG2D-CAR T cell system and validate its targeting efficacy against senescent cells. Our approach was to genetically engineer mouse primary T cells to express NKG2D-CAR and construct genotoxic stress- and oxidative stress-induced senescence models using mouse forebrain astrocytes (AST) and MEFs. The expression of NKG2DLs on the surface of aforementioned senescent cells was confirmed, and the cytotoxicity of NKG2D-CAR T cells against these NKG2DLs-expressing senescent cells was subsequently carried out by co-culture experiments at different effector-to-target (E: T) ratios *in vitro*. With this investigation, we aimed to propose a novel targeted senolytic approach-CAR-T cell-based immunotherapy to address aging and age-associated diseases driven by CS.

The secondary aim of this thesis was to characterize the senescence-specific cell surface proteome, or “surfaceome”, in multiple models of senescence. Our approach was to enrich cell surface proteins via a cell-surface biotinylation method and conduct label-free quantitative MS-based proteomics analysis on normal human lung fibroblasts (NHLFs), HUVECs, MEFs, and mouse AST subjected to genotoxic, oxidative or proteasome stress. With this investigation, we sought to identify potential cell surface candidates for senotherapy. The enrichment of identified candidates was further validated in various tissues of naturally aged mice and in the brain of an AD mouse model. This study provides foundational work for potential future applications aimed at detecting and targeting senescent cells during natural aging and age-related diseases *in vivo*.

2. Materials and Methods

2.1 Materials

2.1.1 Instruments

Tab. 1: List of instruments used in the experiments and analysis of this thesis.

Instrument	Manufacturer	Specifications
Biological Safety Cabinet	Thermo Fisher Scientific	Safe 2020
Cell Counter	Thermo Fisher Scientific	Countess II FL Automated Cell Counter
Centrifuge	Thermo Fisher Scientific	Heraeus Fresco 21
ChemiDoc Imaging System	Bio-Rad	ChemiDoc MP Imaging System
CO2 incubator	Memmert	ICO240
Confocal Microscope	Carl Zeiss	LSM800
Fluorescence Activated Cell Sorting (FACS) sorter	Becton Dickinson	FACSAria III
Flow cytometry (FCM)	Becton Dickinson	Celesta
Fluorescence Microscope	Carl Zeiss	Epi-Scope1-Apotome
IncuCyte platform	Sartorius	IncuCyte S3
Liquid chromatography-tandem Mass Spectrometry (LC-MS/MS)	Thermo Fisher Scientific	Dionex Ultimate 3000 Rapid Separation Liquid Chromatography (RSLC) nanosystem and Orbitrap Exploris 480 MS
Quantitative real-time PCR (qPCR)	Thermo Fisher Scientific	QuantStudio6 Real-Time PCR System
Spectrophotometer	Thermo Fisher Scientific	NanoDrop 2000c
TECAN reader	TECAN	Infinite M Plex
Thermomixer	Eppendorf	Thermomixer comfort
Ultrasonic cleaner bath	VWR	VWR@USC Ultrasonic Cleaner

2.1.2 Reagents and consumables

Tab. 2: List of reagents and consumables used in the experiments of this thesis.

Reagent	Manufacturer	Catalog no.
1X insulin-transferrin-selenium (ITS)	Merck	13146
1X RBC Lysis Buffer	eBioscience	00-4333-57
2-Propanol, min. 99,8 %	Carl Roth	6752.2
4-(2-hydroxyethyl)-1-piperazineethanesulfonic acid (HEPES)	Carl Roth	HN78.1
4',6-diamidino-2-phenylindole (DAPI)	Carl Roth	6843.2
Acetic acid, optima™ LC/MS grade	Thermo Fisher Scientific	A113-50
Pierce Acetonitrile (ACN), LC-MS Grade	Thermo Fisher Scientific	51101
Ammonium bicarbonate	Merck	A6141-500g
Ammonium persulfate (APS)	Merck	A3678-25g
Bond-Breaker Tris(2-carboxyethyl) phosphine) (TCEP)	Thermo Fisher Scientific	77720
Bovine serum albumin (BSA)	Merck	A9418-100g
Bradford Dye Reagent Concentrate	Bio-Rad	5000006
Calcein-AM	Merck	56496
Calcium chloride ($CaCl_2$)	Carl Roth	HN04.2
CD90.2 microbeads	Miltenyi Biotec	130-121-278
Concanavalin A	Bio-Techne	C2010
Dithiothreitol (DTT)	Thermo Fisher Scientific	R0862
DNase I	Roche	10104159001
Ethanol, min. 99,8 %	Carl Roth	9065.2
Ethylenediamine tetraacetic acid (EDTA)	Applichem	A11030500
EZ-Link™ Sulfo-NHS-SS-Biotin	Thermo Fisher Scientific	21331
Formic acid (FA, modifier), LC/MS grade	Thermo Fisher Scientific	15655840
G418	Omnilab	1198774
Glycine	Carl Roth	3790.3
High-performance liquid chromatography (HPLC) water	Thermo Fisher Scientific	51140
Iodoacetic acid (IAA)	Thermo Fisher Scientific	35603
Lipofectamine 3000	Thermo Fisher Scientific	L3000001
Magnesium chloride ($MgCl_2$)	Thermo Fisher Scientific	AM9530G

Milk powder	Carl Roth	T145.3
Optima LC/MS ACN with 0.1 % (v/v) trifluoracetic acid	Thermo Fisher Scientific	LS121-1, 1 L
Optima LC/MS ACN with 0.1 % (v/v) FA	Thermo Fisher Scientific	LS120-1, 1 L
Optima LC/MS water with 0.1 % (v/v) FA	Thermo Fisher Scientific	LS118-1, 1 L
Optima LC/MS water with 0.1 % (v/v) trifluoro-acetic acid	Thermo Fisher Scientific	LS119-1, 1 L
PageRuler Plus Prestained Protein Ladder	Thermo Fisher Scientific	26619
4 % Paraformaldehyde (4 % PFA)	Santa Cruz	sc-281692
Pierce protease and phosphatase inhibitor mini tablets	Thermo Fisher Scientific	A32961
Pierce trypsin protease MS grade	Thermo Fisher Scientific	90058
Polybrene	Merck	TR-1003-G
Polyethylene glycol	BIOZOL	LV825A-1
Potassium chloride (KCl)	Carl Roth	6781.3
PowerUP SYBR Green Master Mix	Thermo Fisher Scientific	A25778
Recombinant human IL-2 (rhIL-2)	Bio-Techne	202-IL-010
Restriction enzymes	New England BioLabs	/
Retronectin	TaKaRa	T100A
RNase Inhibitor (2000 U)	Thermo Fisher Scientific	N8080119
Sodium Chloride (NaCl)	Carl Roth	3957.2
Sodium dodecyl sulfate (SDS)	Carl Roth	2326.2-500g
Sodium hydroxide (NaOH)	Carl Roth	9356.1
Streptavidin magnetic beads	Thermo Fisher Scientific	65601
T4 DNA Ligase	New England BioLabs	M0202L
Tetramethylethylenediamine (TEMED)	Carl Roth	2367.3
TRI Reagent	Merck	T9424-200ML
Trichloromethane/Chloroform	Carl Roth	3313.2
Trifluoroacetic Acid (TFA), LC/MS grade	Thermo Fisher Scientific	10723857
TRIS Hydrochloride (Tris-HCl)	Thermo Fisher Scientific	15568025
Triton X-100	Merck	X100-500
Trypsin-EDTA (0.05 %)	Thermo Fisher Scientific	25300096
Urea (Harnstoff)	Applichem	A1360,1000
VECTASHIELD Antifade Mounting Medium	Bio-Techne	13273694

Viobility 405/452 Fixable Dye	Miltenyi Biotec	130-109-816
Western Bright Chemiluminescence Substrate Quantum	Biozyme	541010
β-mercaptoethanol	Thermo Fisher Scientific	21985023
Dimethyl sulfoxide (DMSO)	AppliChem	A3672,0050
Consumable	**Manufacturer**	**Catalog no.**
Acclaim PepMap C18	Thermo Fisher Scientific	160454
Cell culture plates and flasks	Sarstedt	/
Cell Strainer 40 µm	Sarstedt	83.3945.040
Cell Strainer 70 µm	Sarstedt	83.3945.070
E. coli DH5α cell	Thermo Fisher Scientific	18265017
Eppendorf™ protein LoBind	Thermo Fisher Scientific	10708704
GeneJET Plasmid Miniprep Kit	Thermo Fisher Scientific	10242490
High-Capacity cDNA Reverse Transcription Kit	Thermo Fisher Scientific	639537
LC MS autosampler vials (100 pack)	Waters	186000384C
Lentiviral pHAGE construct	Addgene	114007
Magnetic-activated cell sorting (MACS) LS Columns	Miltenyi Biotec	130-042-401
MicroAmp Optical 384-Well Reaction Plate	Thermo Fisher Scientific	4309849
Microfuge Tube Polypropylene	Beckman Coulter	357448
Nitrocellulose Blotting Membrane (0.1 µm)	Merck	GE10600000
pCL-Eco construct	Addgene	12371
pCMV-dR8.2 dvpr construct	Addgene	8455
pCMV-VSV-G construct	Addgene	8454
Pierce C18 tips, 100 ul bed 96 tips	Thermo Fisher Scientific	87784
PiggyBac transposase expression construct	System Biosciences	PB210PA-1
QuadroMACS Separator	Miltenyi Biotec	130-090-976
Retroviral pFB construct	Addgene	69767
RNeasy Mini Kit	Qiagen	74104
Senescence β-Galactosidase Staining Kit	Cell Signaling Technology	9860
SilverQuest Silver Staining Kit	Thermo Fisher Scientific	LC6070
SuperFrost microscope slides	LI-COR Biosciences	12372098

2.1.3 Antibodies

Tab. 3: List of antibodies used in the experiments of this thesis.

Western blot			
Antibody (Host, antigen)	**Manufacture**	**Catalog no.**	**Dilution**
Rabbit anti-FLAG	Cell Signaling Technology	14793	1:1 000
Rabbit anti-CDKN2A/p16INK4a	Abcam	ab211542	1:1 000
Rat anti-CDKN2A/p19ARF	Abcam	ab26696	1:1 000
Rabbit anti-p53 (D2H9O)	Cell Signaling Technology	32532S	1:1 000
Rabbit anti-p21 Waf1/Cip1	Cell Signaling Technology	64016S	1:1 000
Mouse anti-actin	MP Biomedicals	SKU 0869100	1:5 000
Mouse anti-GAPDH	Abcam	ab8245	1:3 000
Goat anti-rabbit HRP-conjugated secondary antibodies	Promega	W4011	1:3 000
Goat anti-mouse HRP-conjugated secondary antibodies	Agilent Technologies	P044701-2	1:10 000
Goat anti-rat HRP-conjugated secondary antibodies	Cell Signaling Technology	7077S	1:2 000
Immunofluorescence			
Antibody (Host, antigen)	**Manufacture**	**Catalog no.**	**Dilution**
Rat anti-GFAP	Thermo Fisher Scientific	13-0300	1:200
Rat anti-mouse NKG2D/CD314	R&D Systems	MAB1547-100	1:500
Rabbit anti-CD3 zeta	BIOZOL	ABN-H00000919-D01P	1:250
Goat anti-rat IgG Alexa Fluor 488	Thermo Fisher Scientific	A-11006	1:500
Donkey anti-rat IgG Alexa Fluor 594	Thermo Fisher Scientific	A-21209	1:500
Goat anti-rabbit IgG Alexa Fluor 647	Thermo Fisher Scientific	A-21245	1:500
Flow cytometry			
APC-conjugated rat anti-mNKG2D antibody	eBioscience	17-5882-82	1:100
APC-conjugated-rat IgG1 isotype control	eBioscience	17-4301-82	1:100
FITC-conjugated human anti-mCD3	Miltenyi Biotec	130-119-798	1:50

APC-conjugated human anti-mCD4	Miltenyi Biotec	130-116-487	1:50
VioBlue-conjugated human anti-mCD8a	Miltenyi Biotec	130-102-431	1:50
PE-conjugated human anti-mH60	Miltenyi Biotec	130-108-820	1:50
PE-conjugated human anti-mRae-1 Pan	Miltenyi Biotec	130-111-283	1:50
PE-conjugated rat anti-mMult1	R&D systems	FAB2588P	1:1 00

CDKN2A, cyclin-dependent kinase inhibitor 2A; GAPDH, glyceraldehyde-3-phosphate dehydrogenase; HRP, Horseradish peroxidase; GFAP, glial fibrillary acidic protein; APC, Allophycocyanin; PE, Phycoerythrin; FITC, Fluorescein isothiocyanate.

2.1.4 Software

Tab. 4: List of software used in the analysis of this thesis.

Software	Specifications
Fiji (imageJ), v. 2.0.0.-RC-67/1.52c	Wayne Rasband (NIH)
ZEN 3.1 (blue edition)	Carl Zeiss
Proteome Discoverer™, v. 2.5.0.400	Thermo Fisher Scientific
GraphPad Prism, v. 9.3.1	GraphPad Software, Inc
Adobe Illustrator, v. 26.0	Adobe
R software, v. 4.3.1	R Foundation
FlowJo, v.10	Becton Dickinson
Microsoft ware (Office, Excel)	Microsoft
Zotero, v. 6.0.28	GMU and CHNM
Chiplot	https://www.chiplot.online/
Metascape Database	https://metascape.org/gp/index.html
Cytoscape	https://cytoscape.org/
InteractiVenn	http://www.interactivenn.net/
Biorender	https://www.biorender.com/
String protein-protein interaction	https://string-db.org
Biological DataBase network (bioDBnet)	https://biodbnet-abcc.ncifcrf.gov/db/db2db.php
Protter	https://wlab.ethz.ch/protter/start/
ChatGPT v.4	To improve language and readability

2.2. Methods

2.2.1 Mice

The study in this thesis employed C57BL/6J and APP/PS1 (B6.Cg-Tg (APPswe,PSEN1dE9)85Dbo/Mmjax) mice from the Jackson Laboratory (strains #000664 and #034832, respectively), maintained in pathogen-free conditions with a 12:12 h photoperiod at 22 °C and 55 % humidity. Mice had ad libitum access to food and water. Procedures complied with the German Animal Welfare Act and were approved by the “Landesamt für Natur, Umwelt und Verbraucherschutz Nordrhein-Westfalen” (Recklinghausen, Germany). Following CO2 suffocation, mice tissues were harvested, snap-frozen in liquid nitrogen, and stored at -80 °C.

2.2.2 Cell culture

Cells were incubated at 37 °C in a humidified environment containing 5 % CO2. Cell medium and supplements used are listed in **Tab. 5**. HUVECs (Lonza, #C2517A) were cultured in EBM-2 with EGM-2 SingleQuots supplements, and NHLFs (Lonza, #CC-2512) were cultivated in FBM with the addition of FGM-2 SingleQuot supplements and growth factors. As previously described (Schildge et al. 2013), astrocytes were extracted from the forebrains of P2-P4 C57BL/6J mice. After the removal of the meninges, brains were washed with HBSS, followed by a 10-min treatment with trypsin and DNase I at 37 °C. After seeding in DMEM with 10 % FBS and 1 % penicillin-streptomycin to confluency (7-10 days), microglia were removed by shaking at 180 rpm for 30 min at 37 °C, followed by the detachment of oligodendrocyte precursor cells at 240 rpm for 6 h at 37 °C and manual flask tapping for 1 min. Astrocytes were subsequently maintained in fresh medium. GFAP staining was used to validate the extracted astrocytes (**Fig. 1**). As previously described (Jain et al. 2014), MEFs were extracted from E13.5 wild-type C57BL/6J embryos. Following the removal of visceral organs, embryos were separated and finely chopped. The resultant cells underwent enzymatic dissociation using trypsin and were then grown in DMEM supplemented with 10 % FBS and 1 % penicillin-streptomycin. Human embryonic kidney 293T (HEK293T) cells and B16F10 murine melanoma cells (LGC Standards, Middlesex, UK, #ATCC-CRL-6475) were cultured in DMEM supplemented with 10 % FBS and 1 % penicillin-streptomycin.

Tab. 5: List of cell culture media and supplements.

Cell Culture Media and Supplements	Manufacturer	Catalog no.
Dulbecco's modified Eagle's medium (DMEM), high glucose, GlutaMAX Supplement	Thermo Fisher Scientific	31966047
Dulbecco's Phosphate Buffered Saline (DPBS)	Thermo Fisher Scientific	14190250
EBM-2 Basal Medium	Lonza	CC-3156
EGM-2 SingleQuots supplements	Lonza	CC-4176
FBM Fibroblast Growth Basal Medium	Lonza	CC-3131
Fetal bovine serum (FBS)	Thermo Fisher Scientific	10500064
Hanks' Balanced Salt Solution (HBSS)	Thermo Fisher Scientific	14175095
Penicillin-Streptomycin	Thermo Fisher Scientific	15140122
RPMI 1640 Medium, GlutaMAX Supplement	Thermo Fisher Scientific	61870044

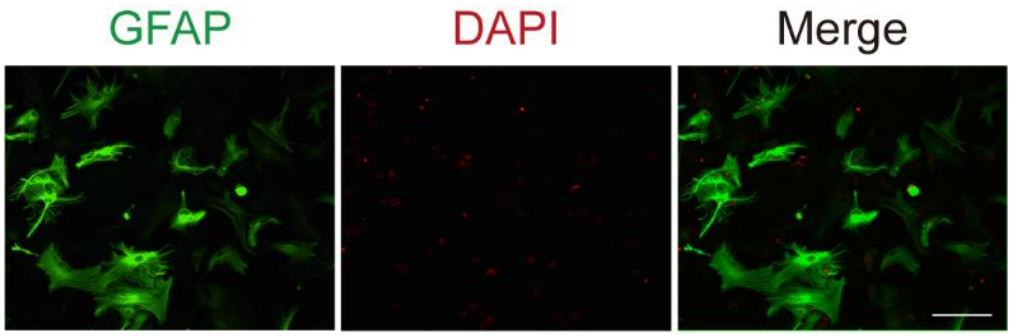

Fig. 1: Validation of extracted mouse astrocytes by GFAP immunostaining. Astrocytes isolated from the forebrain of mice at early passages (P1-P2) were subjected to immunostaining analysis. The cells were stained using an anti-GFAP antibody (green) and were co-stained for nuclear visualization with DAPI (red). Scale bar = 50 µm. GFAP, glial fibrillary acidic protein; DAPI, 4',6-diamidino-2-phenylindole.

2.2.3 Construction of NKG2D-CAR and PiggyBac NKG2DLs vectors

The construction of the murine NKG2D-CAR was performed by fusing the CD3ζ chain's cytoplasmic region's coding sequence (CD3ζ-CYP) with the full-length coding sequence of the murine NKG2D receptor (NKz-CAR), as previously described (Driouk et al. 2020, Zhang et al. 2005). The NKG2D-CAR cDNA was synthesized and cloned into the pUC57

vector by Genscript (www.genscript.com). NKz-CAR was amplified by polymerase chain reaction (PCR). Primers used are listed in **Tab. 6**. To create the retroviral vector for NKz-CAR, we utilized the pFB-internal ribosomal entry site (IRES)-Neo (neomycin resistance) vector backbone, integrating an mCherry/GFP sequence connected by a Thosea asigna virus 2A (T2A) peptide sequence. The amplified NKz-CAR was then subcloned into pFB-T2A-mCherry/GFP-IRES-Neo vector. For the lentiviral NKz-CAR construct, the pHage-elongation factor 1-alpha (EF1α)-MHC class I chain-related proteins A (MICA)-IRES-Zoanthus sp. green fluorescent protein (ZsGreen) vector backbone was modified by replacing MICA with NKz-CAR via restriction enzyme cloning, inducing the expression of NKz-CAR.

To construct PiggyBac vectors encoding mouse NKG2DLs, custom-designed PiggyBac backbone vectors, containing 5' and 3' inverted terminal repeats (ITRs), were obtained from VectorBuilder (vectorbuilder.com) and engineered to insert the EF1α promoter, a Neo sequence, and a simian virus 40 PolyA (SV40 PolyA) termination sequence through T2A linkage. The murine NKG2DLs' coding sequences were PCR-amplified using pCMV6-Ampicillin-IRES-GFP vectors encoding histocompatibility antigen 60a (H60a), retinoic acid early transcript 1β (Rae1β), or murine UL16-binding-protein-like transcript 1 (Mult1), obtained from Genscript. Details on the primers are provided in **Tab. 6**. These PCR fragments were cloned into the PiggyBac transposon expression vector PB-EF1α-T2A-Neo-PolyA, yielding the PiggyBac-based PB-EF1α-NKG2DL-T2A-Neo-PolyA constructs for expression of individual mouse NKG2DLs. Enzymatic digestion of the plasmids was performed at 37 °C for 1 h followed by ligation with T4 DNA Ligase. Plasmids were then transformed into E. coli DH5α cells for propagation, and DNA was purified using the GeneJET Plasmid Miniprep Kit. Sequence validation was carried out by Eurofins Genomics (eurofinsgenomics.eu).

Tab. 6: List of PCR primer sequences used for vector construction.

Primer Name	**Forward**	**Reverse**
mNKz-CAR	ATAGTCGACACCATGAG AGCAAAATTCAGCAGGA GTGCAG	ATAGCGGCCGCTCGAGTCCGG ACACCGCCCTTTTCATGCAGAT GTACGTGTTTAG
mNKz-CAR-FLAG	ATTTGCGGCCGCATGAG AGCAAAATTCAGCAGGA GTG	CTAGCTAGCTTACTTGTCATCAT CGTCCTTGTAGTCCACCGCCCT TTTCATGCAGATGTAC

PiggyBac_H60a	TGATAGCGGCCGCATGGCAAAGGGAGCCACCAGCAAGAG	TAAGACGCGTTAGCTGGTAATGAGGACTGCAGAAGAAG
PiggyBac_Rae1β	TAATAGCGGCCGCATGGCCAAGGCAGCAGTGACCAAG	CACGACGCGTCATCGCAAATGCAAATGCAAATAATAAAG
PiggyBac_Mult1	TGATAGCGGCCGCATGGAGCTGACTGCCAGTAACAAGGTC	TACGACGCGTTGGGATCCCATCAATATCGTCTGAAGTCAACAGC
PiggyBac_EF1α	TGTAAGAATTCAGTTTGGACTAGTCGTGAGGCTCCGG	GTAACTAAGCTTACCGGTTCTAGAGCGGCCGCTTCACGACACCTGAAATGGAAG
PiggyBac_T2A-Neo-SV40 PolyA	AATATCTAGAGACGTCACGCGTGAGGGCAGAGGAAGTCTTCTAACATGCGGTGACGTGGAGGAGAATCCCGGCCCTGCTAGCATGATTGAACAAGATGGATTGCACGCAGGTTCTCC	CAGCAAGCTTTAAGATACATTGATGAGTTTGGACAAAC

Restriction sites are underlined. mNK, murine Natural killer group 2D.

2.2.4 Cell transfection and establishment of stable cell lines

Using Lipofectamine 3000, HEK293T cells were transiently transfected with the lentiviral NKz-CAR plasmid following the protocol provided by the manufacturer. Expression of both NKG2D-CAR and FLAG-tag was assessed 48 h after transfection. To generate the stable B16F10 cell lines that express individual mouse NKG2DLs, B16F10 cells were first co-transfected with the PB-EF1α-NKG2DL-T2A-Neo-PolyA PiggyBac transposon plasmid and the PiggyBac transposase expression vector. Post-transfection, we selected the cells with 2 mg/ml of G418, and picked the single clones. These clones were then expanded and subsequently evaluated for their expression of the individual mouse NKG2DL.

2.2.5 Mouse T cell isolation and transduction

Spleens were extracted from 8-12-week-old wild-type C57BL/6J mice and dissected to isolate primary T cells. After lysis of red blood cells using 1X RBC Lysis Buffer, mouse Pan T cells were enriched using CD90.2 microbeads employing a MACS system according to the manufacturer's protocol. Purified T cells were then maintained in a culture medium consisting of RPMI-1640 supplemented with 10 % FBS, 1 % penicillin-streptomycin, 1X ITS, 55 μM β-mercaptoethanol, and 80 IU/mL of recombinant rhIL-2. For

activation, T cells were treated with 5 µg/ml of concanavalin A. For cell plating, a 12-well plate was precoated with 15 µg/ml of Retronectin at 4 °C overnight, followed by a 30-min room temperature coating with 2 % BSA. Within 24 h of activation, T cells were resuspended at a concentration of 1.5 × 10^6 cells/ml in RPMI-1640 with 10 % FBS and 80 IU/mL of rhIL-2 for subsequent transduction.

Retroviral supernatants, used for transduction, were collected from “Platinum-E” (Hölzel Diagnostika, #RV-101) packaging cells transfected with NKz-CAR retroviral plasmid and pCL-Eco helper plasmid using Lipofectamine 3000, 48 h post-transfection. Similarly, lentiviral particles were collected from “Platinum-A” (Hölzel Diagnostika, #RV-102) packaging cells transfected with NKz-CAR lentiviral plasmid and the helper plasmids pCMV-dR8.2 dvpr and pCMV-VSV-G. The lentiviral supernatants were concentrated using polyethylene glycol. All viral supernatants were filtered through 0.45 µm filters. For retrovirus-based transduction, a mixture of activated mouse T cells and retroviral supernatants containing 4 µg/ml polybrene was plated in the Retronectin-coated wells and centrifuged at 2 000 × g at 30 °C for 1 h. A second transduction followed 24 h later using freshly collected retroviral supernatants under the same conditions. For lentiviral transduction, concentrated virus was added at a multiplicity of infection of 50. Post-transduction, T cells were cultured in fresh medium supplemented with rhIL-2, with medium changes every other day. Cell counts were monitored daily to maintain a density of 1-2 × 10^6 cells/ml. The transduced T cells were then assessed for expression and functionality three to four days post-transduction.

2.2.6 Senescence induction

The drugs used to induce senescence in this thesis are listed in **Tab. 7**. To construct genotoxic stress-related senescence models, P1-P3 NHLFs and MEFs were treated with ETO at concentrations of 5 µM and 10 µM respectively for 48 h, followed by three washes with DPBS and harvest 5 days later. P1-P2 mouse astrocytes were incubated with 5 µM ETO for 24 h and harvested 2 days post-wash. To generate oxidative stress-induced senescence models, P1-P3 HUVECs and NHLFs were treated with 100 µM H2O2 for 5 days, then cultured 2 more days post-wash. P1-P2 mouse astrocytes and MEFs were incubated with 200 µM H2O2 for 2 h, followed by extended culturing in complete medium for 7 and 3 more days, respectively. To construct proteasome stress-associated

senescence models, P1-P2 mouse astrocytes was induced with 5 nM EPO for 6 days. P1-P3 proliferating cells treated with 0.1 % DMSO served as controls, all maintained at 60 % confluency before treatments.

Tab. 7: List of drugs treated to the cells.

Drugs	Manufacture	Catalog no.
Epoxomicin	Hölzel Diagnostika	HY-13821
Etoposide	Merck	E1383
Hydrogen peroxide (H2O2)	Merck	H1009

2.2.7 SA-β-gal staining

The activity of SA-β-gal was evaluated using a commercial Senescence β-Galactosidase Staining Kit. Briefly, 1×10^5 cells per cell condition were plated in 24-well plates for 24 h. Staining for SA-β-gal was then carried out following the manufacturer's protocol. Subsequently, cells were co-stained with DAPI and examined using an Epi-Scope1-Apotome fluorescence microscope with a 10x objective. The percentage of SA-β-gal positive cells, identified by their blue coloration, was quantified from the total cell count using Fiji software.

2.2.8 RNA extraction, reverse transcription and qPCR

Total RNA was extracted using the RNeasy Mini Kit, following the procedures outlined by the manufacturer. 1 000 ng RNA was then reverse-transcribed to cDNA using the High-Capacity cDNA Reverse Transcription Kit. qPCR analyses were conducted using PowerUP SYBR Green Master Mix on a QuantStudio6 Real-Time PCR System. For quantification, the cycle threshold (CT) values of the target genes were normalized against the CT values of β-actin. Primers used are listed in **Tab. 8**.

Tab. 8: List of primer sequences used for real-time quantitative PCR analyses.

Gene Name	Forward	Reverse
CDKN2A/P16INK4A (Homo sapiens)	GGGTCGGGTAGAGGAGGTG	GCTGCCCATCATCATGACCT
CDKN1A (Homo sapiens)	ACCTGTCACTGTCTTGTACCC	CGTTTGGAGTGGTAGAAATCTGTC
TP53 (Homo sapiens)	CCTGAGGTTGGCTCTGACTG	CTTCTTTGGCTGGGGAGAGG

ACTB (Homo sapiens)	AACCGCGAGAAGATGACCCA	GGATAGCACAGCCTGGATAGCA
cdkn2a/p16ink4a (Mus musculus)	CCCAACGCCCCGAACT	GCAGAAGAGCTGCTACGTGAA
cdkn2a/p19arf (Mus musculus)	CTCTGGCTTTCGTGAACATG	TCGAATCTGCACCGTAGTTG
cdkn1a (Mus musculus)	CAGATCCACAGCGATATCCAG	AGAGACAACGGCACACTTTG
trp53 (Mus musculus)	ATGTTCCGGGAGCTGAATG	CCCCACTTTCTTGACCATTG
h60a (Mus musculus)	AACCATTGCCTGATTCTGAGC	TGGGACAAATCAGCACACATC
h60b (Mus musculus)	TCAGAAGGGATGAGGAACCAG	GTTGATGGCCCAGAATCCAC
h60c (Mus musculus)	GCTGCCTCAACAAATCGTCG	ATCAACCCATCAAAGGGGCT
rae1α (Mus musculus)	GGGAGACAGCAAATGCCACT	AGGAATTTGGCCCTGGCTTT
rae1β (Mus musculus)	GCAAATGCCACTGAAGTGAAG	CCATTGGTCTTGTGAGTGTCC
rae1δ (Mus musculus)	TCCTACCCCAGCAGATGAAGT	TTCAGTGGCATTTGCTGTCTC
rae1ε (Mus musculus)	TCCTACCTCAGCAGACCTTCC	TCCTGGCACAAATCGTTCAGA
mult1 (Mus musculus)	TTGACAGTGCCTGAGACGTG	TCGTCTGAAGTCAACAGCACA
plxna1 (Mus musculus)	CTGGAAGGCCGAGTCAACAT	AAAAGGCACTCGTACCCTCG
plxna3 (Mus musculus)	TAACACATGCCAGGGCAAGAA	ACCCACCAGCACCATAACAG
ptk7 (Mus musculus)	ACTCTGCTCAGAGCCCTGCTTCT	CCTCCACTTCACAACGGAGCA
cyb5r1 (Mus musculus)	GGGATCCAGCCGGTTACTCT	GGAACCTCCTGGTGTTGTGG
actb (Mus musculus)	CCCTGAAGTACCCCATTGAAC	CCATGTCGTCCCAGTTGGTAA

CDKN1A, cyclin-dependent kinase inhibitor 1A; TP53, tumor protein p53; ACTB, actin beta; trp53, transformation-related protein 53. plxna1, plexin A1; plxna3, plexin A3; ptk7, protein tyrosine kinase 7; cyb5r1, cytochrome b5 reductase 1.

2.2.9 Western blot

Cell lysates were prepared in Tris-Buffered Saline (TBS, pH 7.6) with 2 % SDS and a cocktail of protease and phosphatase inhibitors. Protein samples ranging from 30 to 50 mg were electrophoresed on 10–15 % Sodium dodecyl-sulfate polyacrylamide gel electrophoresis (SDS-PAGE) gels and subsequently transferred to nitrocellulose

membranes. The membranes were then blocked using 10 % skim milk in PBS for 1 h at room temperature and incubated with primary antibodies at 4 °C overnight. Following a wash with PBS containing 0.1 % Tween20, membranes were incubated with HRP-conjugated secondary antibodies for 1.5 h at room temperature. Immunoblots were captured on a ChemiDoc Imaging System, and band intensities were analyzed using Fiji software.

2.2.10 Immunofluorescence

Cells were fixed in 4 % PFA for 10 min and subsequently rinsed three times with ice-cold PBS. Following permeabilization with PBS containing 0.1 % Triton X-100 (PBST) for 10 min, cells were washed and blocked for 30 min at room temperature using 3 % BSA in PBST. The primary antibodies were prepared in the blocking solution and applied to the cells for an overnight incubation at 4 °C. Cells were then washed three times in PBS and treated with Alexa Fluor-tagged secondary antibodies in 1 % BSA in PBS for 1 h at room temperature. After three washes in PBS, cells were mounted on microscope slides using VECTASHIELD Antifade Mounting Medium containing DAPI. Imaging was performed on an LSM800 confocal microscope using a 63× oil immersion lens or on an Epi-Scope1-Apotome fluorescence microscope with a 20× objective. Images were processed and analyzed using Fiji and Zeiss ZEN software.

2.2.11 Flow cytometry

Fluorescence-Activated Cell Sorting (FACS) was utilized to evaluate T cell viability, transduction efficiency, NKG2D surface expression on T cells, T cell subsets, and NKG2DLs surface expression on B16F10 cells and primary mouse cells. A total of 1×10^6 cells per sample were collected, washed with ice-cold PBS, and then resuspended in 100 µl of ice-cold PBS supplemented with 2 % BSA. For the T cell viability assay, cells were first stained with Viobility 405/452 Fixable Dye for viability. Subsequently, the cells were incubated with antibodies for 20-30 min at 4 °C in the dark, according to the manufacturer's instructions. Post-staining, cells were washed with ice-cold PBS and analyzed using a FACS instrument (Becton Dickinson, Celesta). Cell sorting was performed using a FACS sorter (Becton Dickinson, FACSAria III). FlowJo software was employed for data analysis.

2.2.12 Cytotoxicity assay

To assess the cytotoxic efficacy of NKG2D-CAR T cells against B16F10 cells expressing NKG2DLs and against mouse senescent cells, a real-time cytotoxicity assay was performed. Target cells were plated at densities of 3 000 to 5 000 cells per well in six replicates on 96-well black plates with clear bottoms. After 24 h, the medium was discarded, and cells were incubated with 5 µg/ml Calcein-AM in RPMI for 30 min at 37°C in a 5 % CO2 atmosphere. After labeling with Calcein-AM, target cells were washed and then incubated with 100 µl of effector cell suspension (either untransduced (UN) T cells or NKG2D-CAR T cells in RPMI complete medium) at different E: T ratios. The plate was then centrifuged at 200 x g for 2 min and placed in an IncuCyte S3 system at 37°C with 5 % CO2 for 4 h for B16F10 cells, and 8 h for mouse primary cells. Live imaging was performed every 2 h using a 4× objective, capturing the whole-well to capture changes in the green fluorescence indicative of Calcein-AM positive viable target cells. Viable cell counts were analyzed using Fiji software.

2.2.13 Mass spectrometry analysis of cell surface proteins

2.2.13.1 Cell surface protein extraction

Human and mouse primary cells grown on plates (~2×10^7 cells) were washed three times with ice-cold DPBS buffer supplemented with 1 mM $CaCl_2$ and 0.5 mM $MgCl_2$ (pH= 8) and then incubated with 0.5 mg/ml Sulfo-NHS-SS-Biotin for 30 min at 4 °C, with gentle shaking. Following biotinylation, the cells were rinsed three times with ice-cold DPBS (pH= 8). Residual, unreacted N-Hydroxysuccinimide ester, was quenched by incubation with 0.1 M glycine for 30 min at 4 °C. In subsequent steps, cells were first washed three times with DPBS (pH= 8), then lysed in a lysis buffer (50 mM HEPES (pH= 7.4), 150 mM NaCl, 1 mM EDTA, and 1.5 % SDS), prior to overnight incubation of lysates with streptavidin magnetic beads at 4 °C. Elution of streptavidin-bound proteins was aided by four washes with lysis buffer, followed by boiling in an elution buffer (2 % SDS, 100 mM Tris-HCl (pH= 7.5), and 0.1 M DTT) for 5 min.

2.2.13.2 Peptides preparation for Mass Spectrometry analysis

Extracted cell surface proteins were heated at 95 °C for 5 min, then quickly cooled on ice. 2.5 % total protein extracts and BSA standards were run on a 12 % SDS-PAGE, followed

by Silver staining to estimate total protein amounts. The SDS-PAGE gel was first run for 15 min at 100 V, to allow total proteins to migrate through the stacking gel and later for 75 min at 150 V, for separation on the separating gel. The SilverQuest Silver Staining kit was employed for estimation of total protein amounts, after image analysis, as suggested by the manufacturer.

Tryptic peptides for LC-MS/MS analysis were generated based on a previously described modified Filter-aided-Sample-preparation (FASP) protocol (Scifo et al. 2015). Approximately, 20 µg cell surface proteins were first reduced by incubation with 10 mM DTT and 2 mM TCEP in Tris (pH= 8) at 60 °C for 15 min, then alkylated with addition of 50 mM IAA and incubation for 30 min the dark. Filter columns (MWCO 10 kDa) were primed for the FASP protocol with two washes of HPLC water, two washes with 0.1 M NaOH, another three washes with HPLC water and one with 8 M urea buffer (UB), prior to sample loading. Samples were mixed with 300 µl UB, transferred to filter columns and subjected to buffer exchange by centrifugation at room temperature, for 40 min. Detergents in the samples were depleted by repeating the washes 6 times with 300 µl UB, followed by centrifugation at 17,000 x g for 20 min. Samples were then digested with trypsin (1:20; in 50 mM ammonium bicarbonate) directly on the filter columns for 1 h at 37 °C, followed by overnight incubation at 30 °C with shaking. Residual detergents were removed from the peptides by precipitation with an equal volume of 2 M KCl, incubation for 30 min at room temperature and centrifugation at 17,000 x g for 20 min to collect the supernatant. Subsequently, the peptides were cleaned and desalted using C18 Stage tips, then resuspended in 20 µl 1 % FA for MS analysis or stored at 4 °C till use.

2.2.13.3 LC-MS/MS analysis

Peptide separation and quantification on a Dionex Ultimate 3000 RSLC nanosystem coupled to an Orbitrap Exploris 480 MS instrument, as well as database searching, were performed by Dr. Enzo Scifo (Translational Biogerontology Lab, AG Ehninger, DZNE e.V. Bonn). MS analyses were performed with three biological replicates, for each cell condition. Peptides were separated using a binary solvent system comprising of 95 % eluent A (0.1 % FA in water) and 5 % eluent B (0.1 % FA in 80 % ACN), at a flow rate of 300 nL/min. A trap column cartridge (Acclaim PepMap C18) was used for peptide concentration, prior to separation by reversed-phase chromatography on an Acclaim

PepMap C18, 100 Å, 75 µm X 25 cm column. The following gradients were employed: 5 % to 31 % eluent B in 75 min followed by 31 % to 50 % eluent B in 20 min. Peptides eluting from the LC column were transferred to a stainless steel emitter (Thermo Scientific) for electrospray ionisation using a Nanospray Flex ion source, applying a spray voltage of 1.9 kV and an ion transfer tube temperature of 300 °C. Mass spectrometric data were acquired in data-dependent positive ion mode. Measurement parameters were set as follows: mass range of m/z 375−1550; resolution of 120,000 at m/z 400; target value of 300 % (3×10^6) ions; maximum injection time of 25 ms, charge state of 2-7, dynamic exclusion of 60 sec with exclusion after 1 time and a mass tolerance of 10 ppm, for MS survey scans. A top speed method with a 2 sec cycle time was used for selection of precursor ions for fragmentation. Acquisition of MS2 spectra was based on a decision tree with priority one assigned to those precursor signal intensity thresholds of 3×10^5 or greater and priority two comprising of spectra with an intensity range of 1×10^4 - 3×10^5. Data-dependent MS2 scans were based on the following settings: an isolation window of 2 m/z, normalized collision energy of 30 % High-energy Collision Dissociation, 7.5 K and 15 K resolution, AGC target value of 100 % (1×10^5), maximum ion injection times of 20 and 50 ms, for scan priority one and two, respectively. MS survey scans and MS2 data were acquired in profile and centroid modes, respectively.

Raw MS data was analyzed using Proteome Discoverer™ (PD. Version 2.5) software (Thermo Fisher Scientific). MS2 spectra were searched using the SEQUEST® HT search engine against the Swiss-Prot® *Mus musculus* (v2021-06-20) and *Homo sapiens* (v2021-06-20) databases. Peptide identifications were based on specifying trypsin as the proteolytic enzyme, allowing for 2 missed cleavages as well as setting the minima and maxima peptide length to 7 and 30 amino acids, respectively. Precursor and fragment mass tolerances were set to 10 ppm and 0.02 Da MS2. Carbamidomethylation of cysteine was specified as a fixed modification, while methionine and N-terminal loss of methionine, were set as variable modifications, for all searches. The false discovery rate (FDR) for proteins, peptides, and peptide spectral matches (PSMs) was set to 1 % in the Consensus workflow. In the Spectrum Selector node, the Lowest Charge State = 2 and Highest Charge State = 6 were used. The INFERYS rescoring node incorporated into the Processing workflow was employed to boost peptide identifications. Automatic settings were used and identified peptides were filtered for maximum 1 % FDR using the Percolator

algorithm. A second stage search was applied to identify semi-tryptic peptides. Protein quantification is based on unique and razor peptides. Proteins affected by site, reverse or potential contaminants were filtered out prior to analysis. Unless otherwise specified, default settings of individual nodes were used during the analysis.

2.2.14 Statistics and data analysis

Statistical analysis was conducted using GraphPad Prism software. The results were presented as mean ± SD or mean ± SEM. To assess the differences between two independent groups, an unpaired two-tailed Student's t-test was employed. For comparisons involving three or more groups, differences were determined using either one-way or two-way analysis of variance (ANOVA) followed by Tukey's post-hoc tests to adjust for multiple comparisons. Statistical significance was set as follows: *$P < 0.05$; **$P < 0.01$; ***$P < 0.001$; ****$P < 0.0001$; ns, not significant. For visual representation, figures were created using Adobe Illustrator and Biorender.com.

PSMs of all identified surface proteins across various cellular conditions were subjected to principal component analysis (PCA). For Pearson's correlation analysis, normalized z-scores, adjusted in comparison to the non-senescent control group for the PSMs, were utilized. Cluster analyses were performed on scaled z-scores of PSMs, where scaling involved conversion using the logarithm base 10 (log10). To address zero values in the log10 transformation, each z-score was modified by adding a constant value of 1 before transformation. For negative z-scores representing downregulated proteins, the log10 transformation was applied to the absolute values, and the results were subsequently multiplied by -1.

PCA was conducted using the "tidyverse" package in base R and the results were visualized using the "ggplot2" package. Pearson's correlation analysis was carried out with the "corrplot" R package and the results displayed using the online application "Chiplot," accessible at https://www.chiplot.online/. For clustering analysis, data were processed using the Mfuzz clustering method via the "mfuzz" package in R, with visualizations created through "ggplot2". Volcano plots were generated with the "ggrepal" package in R and visualized via "ggplot2". Cellular Component enrichment analyses were performed using Ingenuity Pathway Analysis (Ingenuity Systems) and displayed on "Chiplot" web. Molecular Function (MF) and Biological Process (BP) enrichment analyses

were conducted using Gene Ontology (GO) from the Metascape Database (https://metascape.org/gp/index.html) and visualized with Chord diagrams using the "circlize" package in R or with Cytoscape. The statistical cut-off value for pathway enrichment was set at $p < 0.05$ or with Benjamini-Hochberg adjusted $p < 0.05$, and a minimal enrichment factor of 1.5. Heat maps were generated and viewed on "Chiplot" web. Venn diagrams were produced using the "eulerr" package in R or the "InteractiVenn" online tool, available at http://www.interactivenn.net/.

3. Results

3.1 Efficacy of NKG2D-CAR T cells in targeting and eliminating stress-induced senescent cells *in vitro*

3.1.1 Construction of NKG2D-CAR T cells

NKG2D-CAR constructs were engineered by fusing the full-length murine NKG2D receptor sequence to the CD3ζ CYP domain (NKz-CAR), as described in previous studies (Driouk et al. 2020, Zhang et al. 2005). In the retroviral vector (RV) pFB-based construct, the reporter protein GFP or mCherry sequence were included, cleaved using the T2A peptide. In the lentiviral (LV) pHAGE vector, NKz-CAR was linked with a FLAG tag and ZsGreen, connected via an IRES element (**Fig. 2A**). The expression validation of NKG2D-CAR constructs was first performed in HEK293T cells. Western blot analyses confirmed the expression of FLAG-tagged protein in LV-transduced HEK293T cells (**Fig. 2B**). Immunofluorescence assays revealed the specific stanning of NKG2D and CD3ζ in ZsGreen-positive HEK293T cells bearing NKz-CAR, further verifying its expression (**Fig. 2C**).

Activated pan T cells, extracted from mouse spleens, were transduced with either the RV or LV NKG2D-CAR constructs. Viability assay showed no difference between RV and LV transduced T cells, averaging 49.3 % for RV (NKG2D-CAR) T cells and 46.8 % for LV (NKG2D-CAR) T cells (**Fig. 2D**). The expression of mCherry was evident in Plat-E packaging cells 48 h post-transfection and in primary T cells 24 h following the second transduction (**Fig. 2E**). The transduction efficiency was higher in RV (NKG2D-CAR) T cells at 56.7 % compared to 37.1 % in LV (NKG2D-CAR) T cells (**Fig. 2F**). Surface expression of the NKG2D receptor on transduced T cells was assessed via FACS three to four days post-transduction, revealing a notable increase in the percentage of NKG2D-positive cells and a significant rise in mean fluorescence intensity (MFI) compared to endogenous NKG2D expression in native T cells (**Fig. 2G**).

FACS was utilized to analyze the composition of CD4+ and CD8+ T cell subpopulations within both UN-T cells and NKG2D-CAR T cells. UN-T cells were collected post-activation, and NKG2D-CAR T cells were sorted by the viable GFP+ or mCherry+ cells. Similar with the UN-T cell population, a significant proportion of NKG2D-CAR T cells, 62.0 % ± 2.5 %,

were identified as CD8+ cells. There was no significant difference in the subpopulation of CD3+ T cell subsets between the UN-T cells and NKG2D-CAR T cells (**Fig. 2H**).

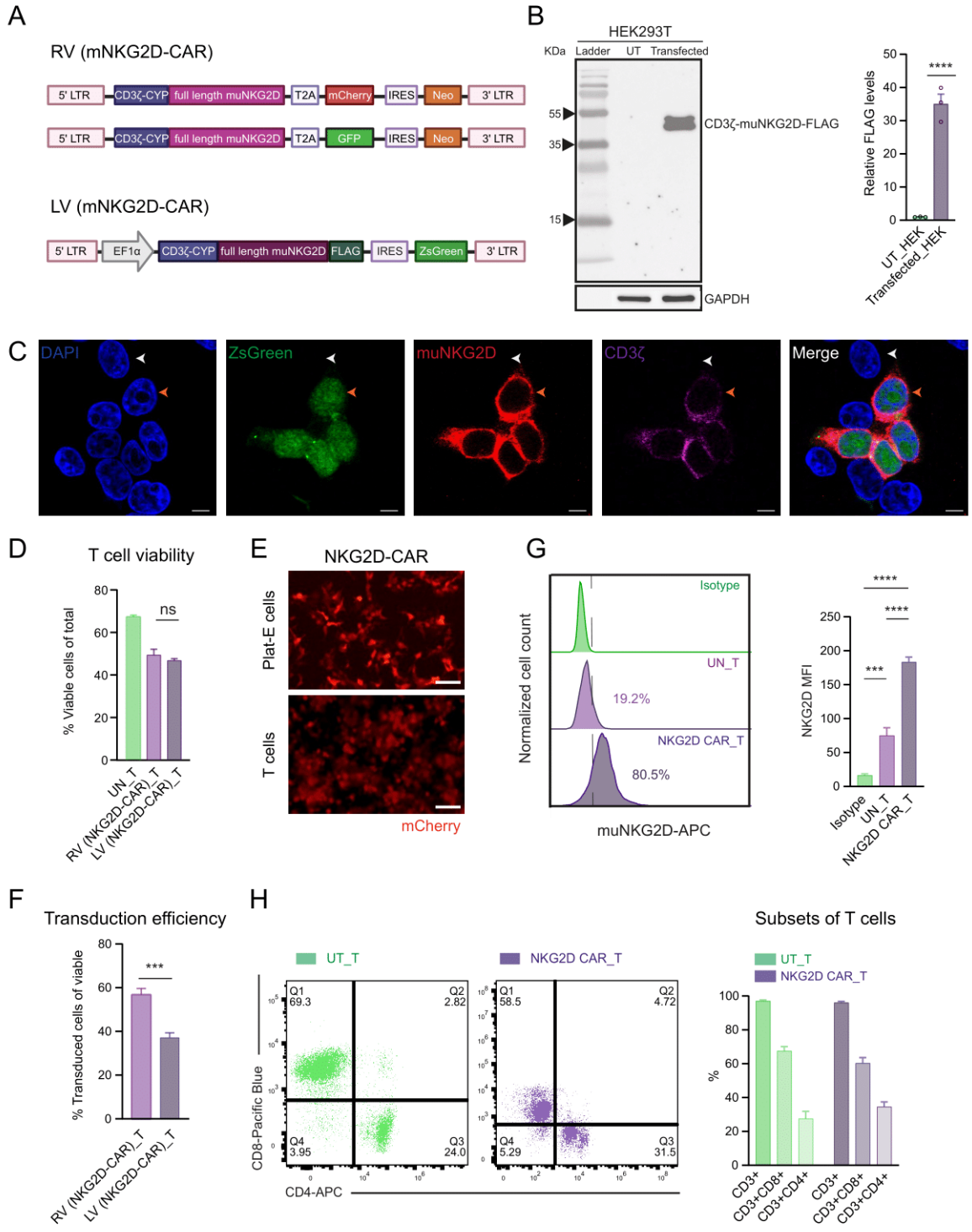

Fig. 2: Construction of NKG2D-CAR T cells. (A) Schematic representation of retroviral (RV) and lentiviral (LV) NKG2D-CAR constructs. (B) Western blot analysis of protein expression of FLAG-tagged NKG2D-CAR in LV NKG2D-CAR construct-transfected and untransfected (UT) HEK293T cells. Data are presented as the mean ± SEM of three

biological replicates and are normalized to GAPDH levels. ****P < 0.0001, determined by unpaired two-tailed Student's t-test analysis. (C) Immunofluorescence staining of LV NKG2D-CAR construct-transfected HEK293T cells. Cells were co-stained with antibodies targeting mouse NKG2D (red) and CD3ζ (purple), respectively. Cell nuclei were stained with DAPI (blue). Indicative NKG2D-CAR+ cells are marked with orange arrows, and NKG2D-CAR- cells with white arrows. Scale bar = 10 μm. (D, F) Analysis of cell viability (D) and transduction efficiency (F) in RV and LV NKG2D-CAR-transduced T cells, evaluated by FACS. Transduction efficiency was calculated as % mCherry/GFP/ZsGreen+ cells among viable cells. Data are presented as the mean ± SEM of six biological replicates. ns, not significant, determined by one-way ANOVA followed by Tukey's post-hoc tests. (E) Fluorescent microscopy images showing Plat-E packaging cells (upper row) and T cells transduced with RV NKG2D-CAR, captured 24 h after the second round of transduction (lower row). Scale bar = 200 μm. (G) Surface expression of NKG2D analyzed by FACS. Histograms show the percentage of positive cells stained with APC-conjugated anti-mouse NKG2D antibody (purple) or isotype antibody (green). MFI data are presented as the mean ± SEM of six biological replicates. ***P < 0.001; ****P < 0.0001, determined by one-way ANOVA followed by Tukey's post-hoc tests. (H) Proportions of CD8 and CD4 subtypes within CD3+ UN-T cells and NKG2D-CAR T cells determined by FACS. NKG2D-CAR T cells were positively sorted for viable GFP+ or mCherry+ cells prior to analysis. Data are presented as the mean ± SEM of two biological replicates, with statistical analyses by two-way ANOVA followed by Tukey's post-hoc tests.

3.1.2 Efficacy of NKG2D-CAR T cells against NKG2DL-expressing cells

To evaluate the targeting ability of NKG2D-CAR T cells, B16F10 melanoma cells were engineered to overexpress individual mouse NKG2DLs: H60a, Rae1β, or Mult1, using the PiggyBac transposon system (**Fig. 3A**). Following neomycin selection, stably transfected cell lines were established from individual colonies and confirmed for NKG2DL surface expression via FACS. As a baseline, unmodified B16F10 cells, which is known to lack NKG2DLs (Kim et al. 2020, Shin et al. 2013), were used as control cells. Each transfected cell line exhibited a significant rightward shift in MFI compared to the control (**Fig. 3B**). Subsequently, cytotoxicity assays were conducted to compare the effectiveness of NKG2D-CAR T cells and UN-T cells against these NKG2DL-expressing B16F10 cells at different E: T ratios. The viability of target cells was dynamically monitored using fluorescent Calcein-AM labeling and automated longitudinal microscopy. UN-B16F10 cells served as the negative control (**Fig. 3C**). After 4 h of co-culture, cytotoxicity percentages were calculated using the formula (1-live fluorescent cell count at 4 h/live fluorescent cell count at 0 h) x 100. The results showed that NKG2D-CAR T cells displayed dose-dependent cytotoxicity against all three NKG2DL-overexpressing cells, achieving maximum cell killing efficacies of 29.9 %, 32.9 %, and 37.2 % at a 20:1 E: T ratio. In

contrast, NKG2D-CAR T cells exhibited minimal cytotoxic efficacy (up to 8.0 %) against NKG2DL-negative control cells (**Fig. 3D**, **E**). Additionally, even at the highest E: T ratio, UN-T cells with inherent NKG2D receptor expression demonstrated only limited cytotoxic activity against NKG2DL-expressing targets (up to 12.5 % lysis), compared to baseline (5.9 % lysis against control cells) (**Fig. 3D**, **E**).

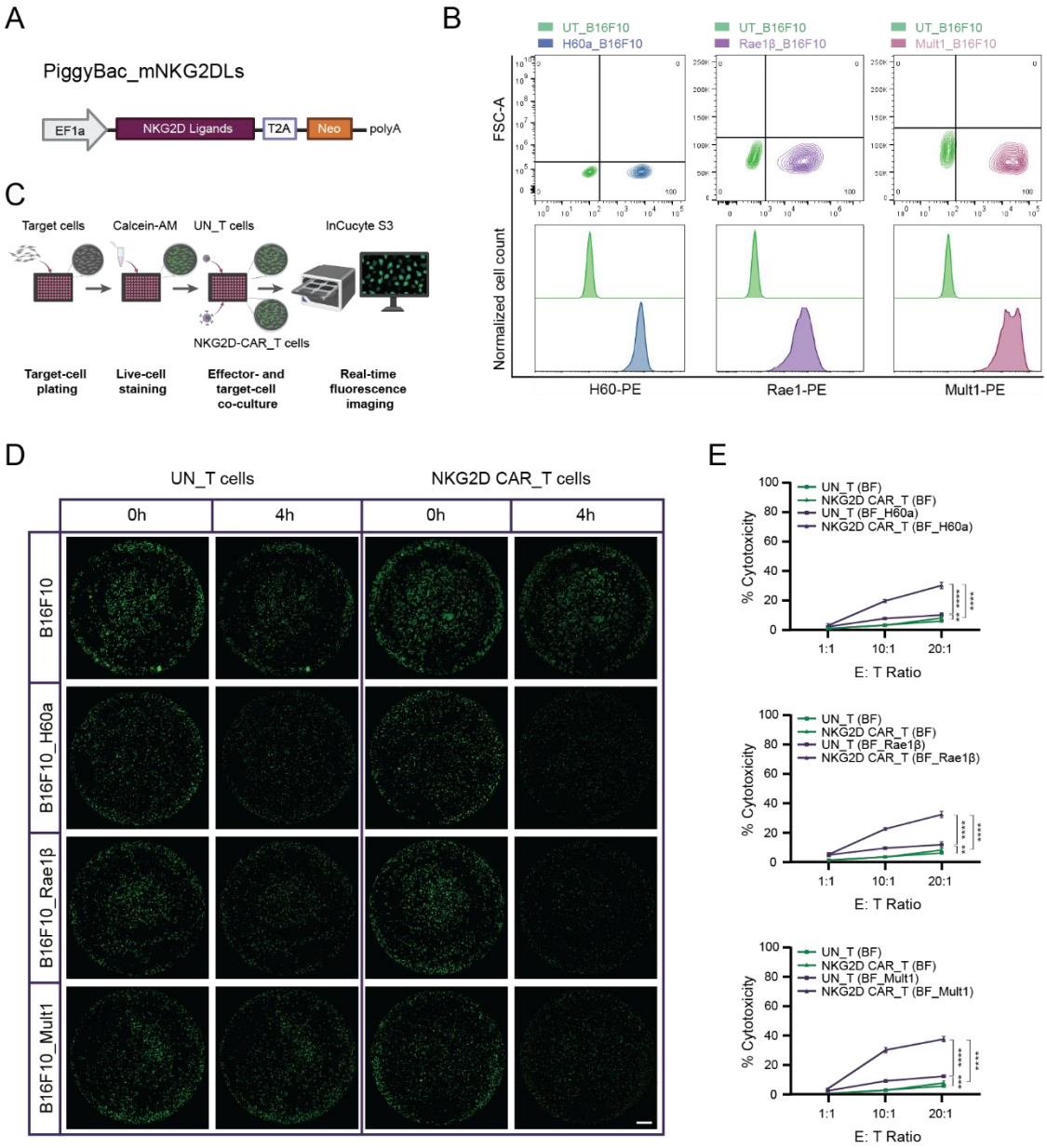

Fig. 3: Efficacy of NKG2D-CAR T cells against NKG2DL-expressing cells. (A) Schematic representation of PiggyBac vector encoding individual mouse NKG2DLs. (B) Assessment of surface expression for each mouse NKG2DL using FACS. Flow plots (upper panel) and histograms (lower panel) illustrate the percentages of positive cells and the MFI of PE-labeled NKG2DL in NKG2DLs-stably transfected B16F10 cells *vs.* UT-

B16F10 cells (control). Analysis is based on results from four independent technical replicates for each transfected cell colony. FSC-A, Forward-scatter area. (C) Schematic representation of Calcein-AM-based cytotoxicity assay. (D) Whole-well imaging of NKG2DL-transfected and UT-B16F10 control cells before (0 h) and after (4 h) co-culture with NKG2D-CAR T cells or UN-T cells at a 20:1 E: T ratio. Live cells are visible with Calcein-AM staining, shown in green. Scale bar = 800 μm. (E) Quantification of cytotoxicity of NKG2D-CAR T cells and UN-T cells towards NKG2DLs over-expressing B16F10 cells and UN-B16F10 cells at different E: T ratios (1:1, 10:1, 20:1) after 4 h of co-culture. Data are presented as the mean ± SD of three biological replicates. **P < 0.01; ***P < 0.001; ****P < 0.0001, determined by two-way ANOVA followed by Tukey's post-hoc tests. BF, B16F10.

3.1.3 Expression of NKG2D ligands in senescent cells triggered by DNA damage and oxidative stress

NKG2DLs are generally not expressed in healthy cells but are upregulated in response to cellular stressors (González et al. 2008). To investigate whether NKG2DLs expression is triggered during stress-induced senescence, MEFs and mouse forebrain AST were treated with the DNA damage agent ETO and the reactive oxygen species (ROS) inducer H2O2. Senescence induction was confirmed by several common used biomarkers. Both MEFs and AST treated with ETO or H2O2 exhibited flattened and enlarged morphological changes, along with increased SA-β-gal activity compared to proliferative control cells (**Fig. 4A**). Elevated levels of negative cell cycle regulators p16ink4a and p19arf were observed in senescent MEFs, while in senescent AST, there was an upregulation of p19arf, p21, and p53 (**Fig. 4B**). qPCR and FACS were employed to assess mRNA and surface protein levels of NKG2DLs in these senescence models, respectively (**Fig. 4C**, **D**). An increase in the protein levels of H60 and Mult1 was observed across all senescent cells, irrespective of the cell type or inducing agent (**Fig. 4D**). Furthermore, Rae1 expression was elevated at the mRNA level in H2O2-treated MEFs and at both mRNA and protein levels in H2O2-treated AST (**Fig. 4C**, **D**). These findings highlight the potential of NKG2DLs as targets for CAR-T cell-mediated clearance of stress-associated senescent cells.

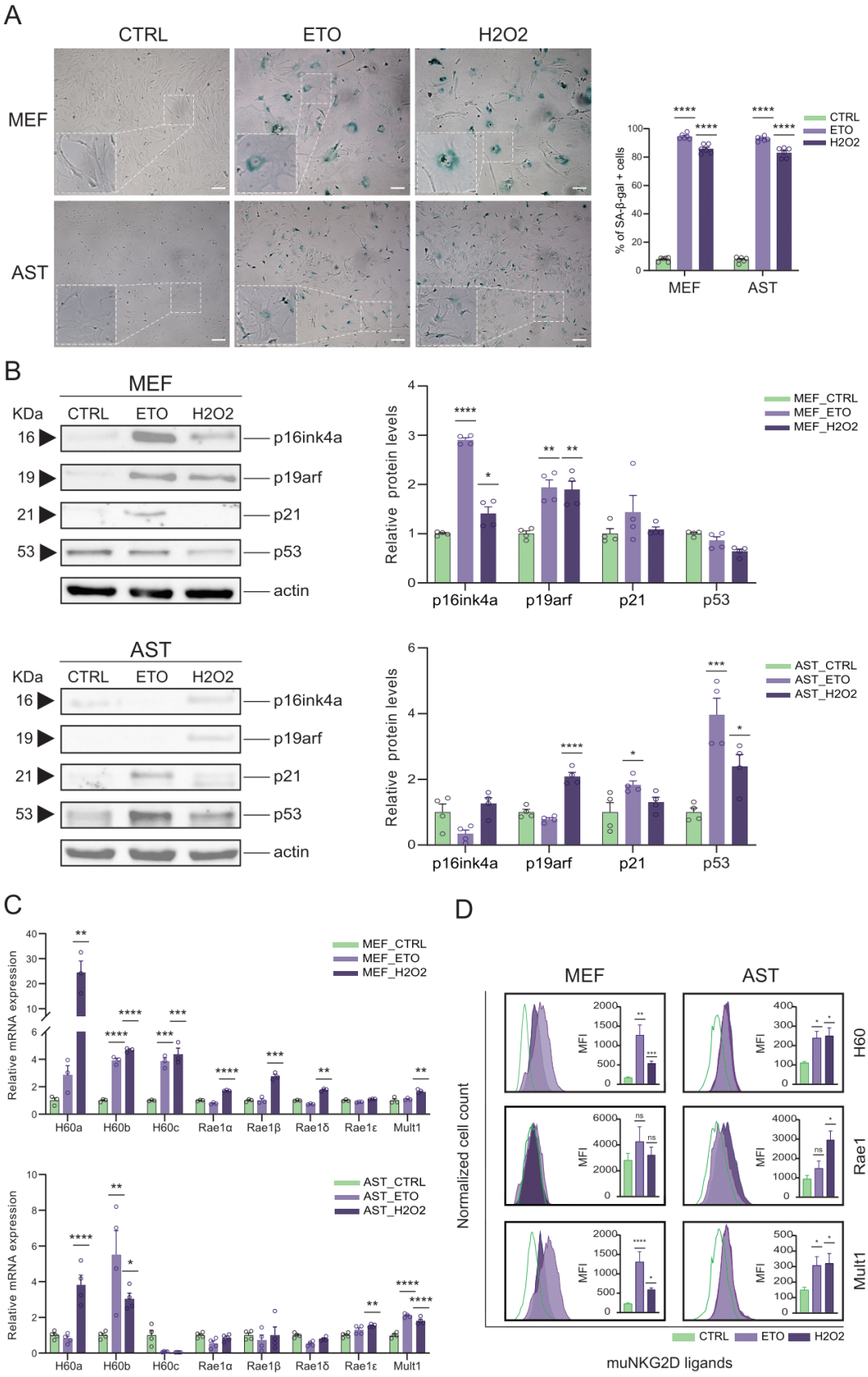
A
CTRL
ETO
H2O2
MEF
AST
% of SA-β-gal + cells
CTRL
ETO
H2O2
B
MEF
KDa
p16ink4a
p19arf
p21
p53
actin
Relative protein levels
MEF_CTRL
MEF_ETO
MEF_H2O2
AST
AST_CTRL
AST_ETO
AST_H2O2
C
Relative mRNA expression
H60a
H60b
H60c
Rae1α
Rae1β
Rae1δ
Rae1ε
Mult1
D
MEF
AST
Normalized cell count
MFI
H60
Rae1
Mult1
muNKG2D ligands

Fig. 4: Expression of NKG2D ligands in senescent cells triggered by DNA damage and oxidative stress. (A) Bright-field microscopy images of SA-β-gal staining in MEFs (upper panel) and AST (lower panel), with or without ETO or H2O2 treatment. Blue staining indicates SA-β-gal positive cells. Scale bar = 100 μm. Percentage of SA-β-gal positive cells was quantified in randomly chosen fields. Results are shown as the mean ± SEM from six biological replicates. (B) Western blot showing protein levels of senescence markers in MEFs and AST, with or without ETO or treatment. Results are shown as the mean ± SEM of four biological replicates normalized against actin levels. (C) qPCR analysis of mRNA levels of mouse NKG2DLs in senescent MEFs and AST triggered by ETO or H2O2. Results, normalized to β-actin mRNA levels, are shown as mean ± SEM from three or four biological replicates. (D) FACS analysis comparing cell surface expression of each mouse NKG2DL in senescent MEFs and AST (filled purple histograms) to that in proliferative control cells (green line histograms). MFI of PE-labeled mouse NKG2DLs is shown as mean ± SEM of three biological replicates. Statistical significance was determined by one-way ANOVA with Tukey's post-hoc tests, where *P < 0.05; **P < 0.01; ***P < 0.001; ****P < 0.0001 for all panels (A-D).

3.1.4 Cytotoxicity of NKG2D-CAR T cells against senescent MEFs and AST expressing NKG2DLs

To evaluate the cytotoxic ability of NKG2D-CAR T cells against senescent cells that express endogenous NKG2DLs, we conducted co-culture assays involving either NKG2D-CAR T cells or UN-T cells and proliferative or senescent MEFs or AST at E: T ratios of 1:1, 5:1, and 10:1 for 8 h. A Calcein-AM-based cytotoxicity assay was utilized to measure the lytic activity of the effector T cells (**Fig. 5A**, **6A**). We observed a dose-dependent increase in cytotoxicity by NKG2D-CAR T cells over UN-T cells against senescent MEFs triggered by both ETO and H2O2. The peak specific killing efficacies reached 53.9 % *vs.* 21.9 % and 67.3 % *vs.* 26.0 % at a 10:1 E: T ratio, respectively (**Fig. 5B**). In contrast, NKG2D-CAR T cells showed minimal lysis of proliferative cells, with the maximum cytotoxicity observed being only 6.3 % across all tested E: T ratios (**Fig. 5B**), which indicates a low off-target activity. A similar pattern of cytotoxic capacity was evident in the NKG2D-CAR T cells against senescent AST, where the highest cytolysis was 78.7 % at a 10:1 E: T ratio in AST induced by H2O2 (**Fig. 6**). UN-T cells exhibited limited cytotoxic efficacy, with up to 18.4 % killing observed towards senescent AST irrespective of the inducing stimuli, a level comparable to the efficacy of NKG2D-CAR T cells against proliferative AST, which was under 15 % (**Fig. 6**). Overall, our findings demonstrate that NKG2D-CAR T cells selectively target and eliminate NKG2DL-expressing senescent cells induced by either DNA damage or oxidative stress.

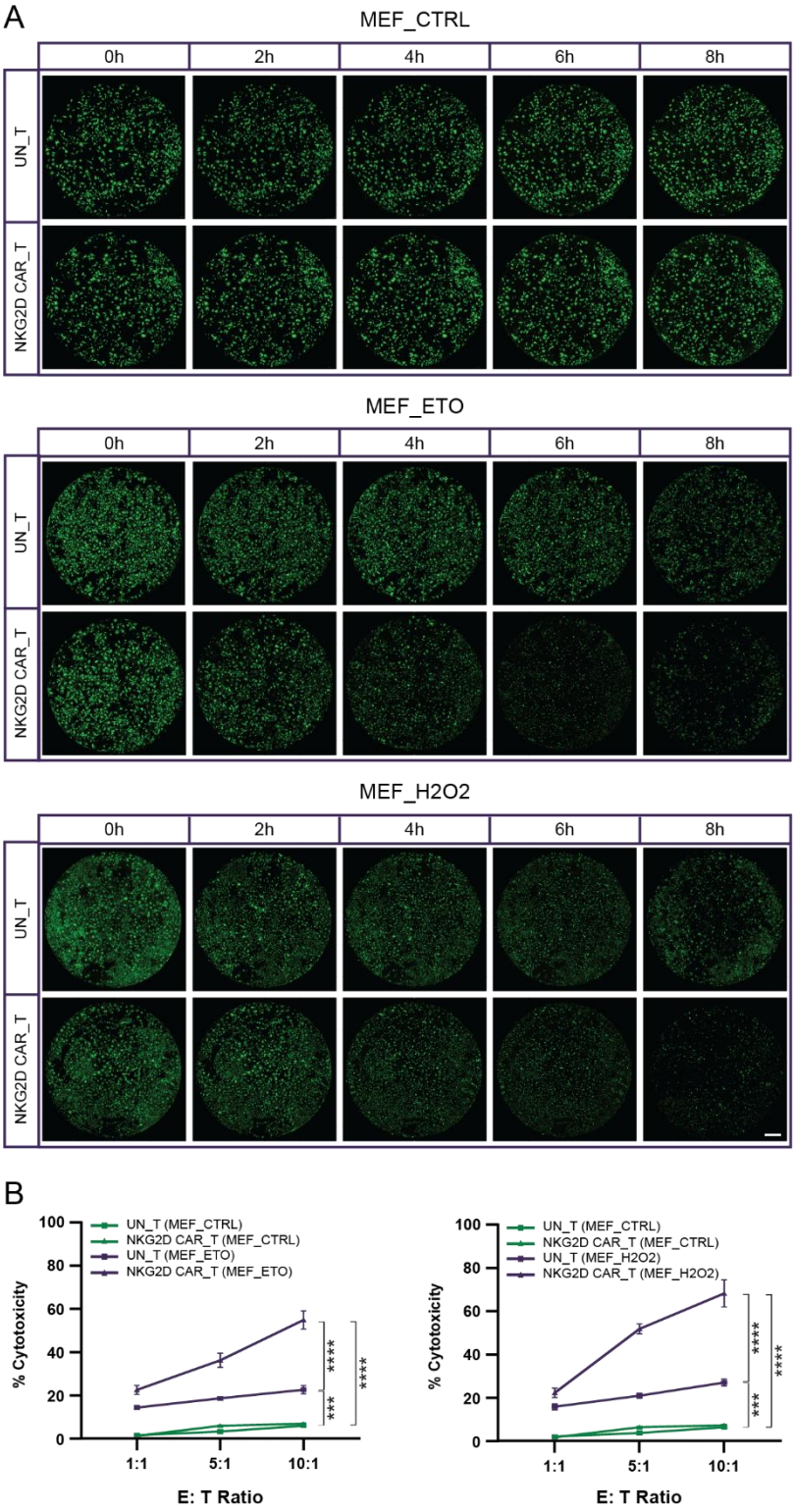

Fig. 5: Cytotoxicity of NKG2D-CAR T cells against senescent MEFs expressing NKG2DLs. (A) Whole-well images showing senescent MEFs induced by either ETO or H2O2, and untreated proliferative MEFs, stained with Calcein-AM and imaged every 2 h during an 8-h co-culture with either NKG2D-CAR T cells or UN-T cells at a 10:1 E: T ratio. Living cells are in green by Calcein-AM staining. Scale bar = 800 μm. (B) Cytotoxicity analysis comparing the efficacy of NKG2D-CAR T cells and UN-T cells against senescent

and proliferative MEFs, calculated after 8 h of co-culture at E: T ratios of 1:1, 5:1, and 10:1. The results are shown as the mean ± SD from four biological replicates. Significance levels are indicated by ***P < 0.001 and ****P < 0.0001, as determined by two-way ANOVA with Tukey's post-hoc tests.

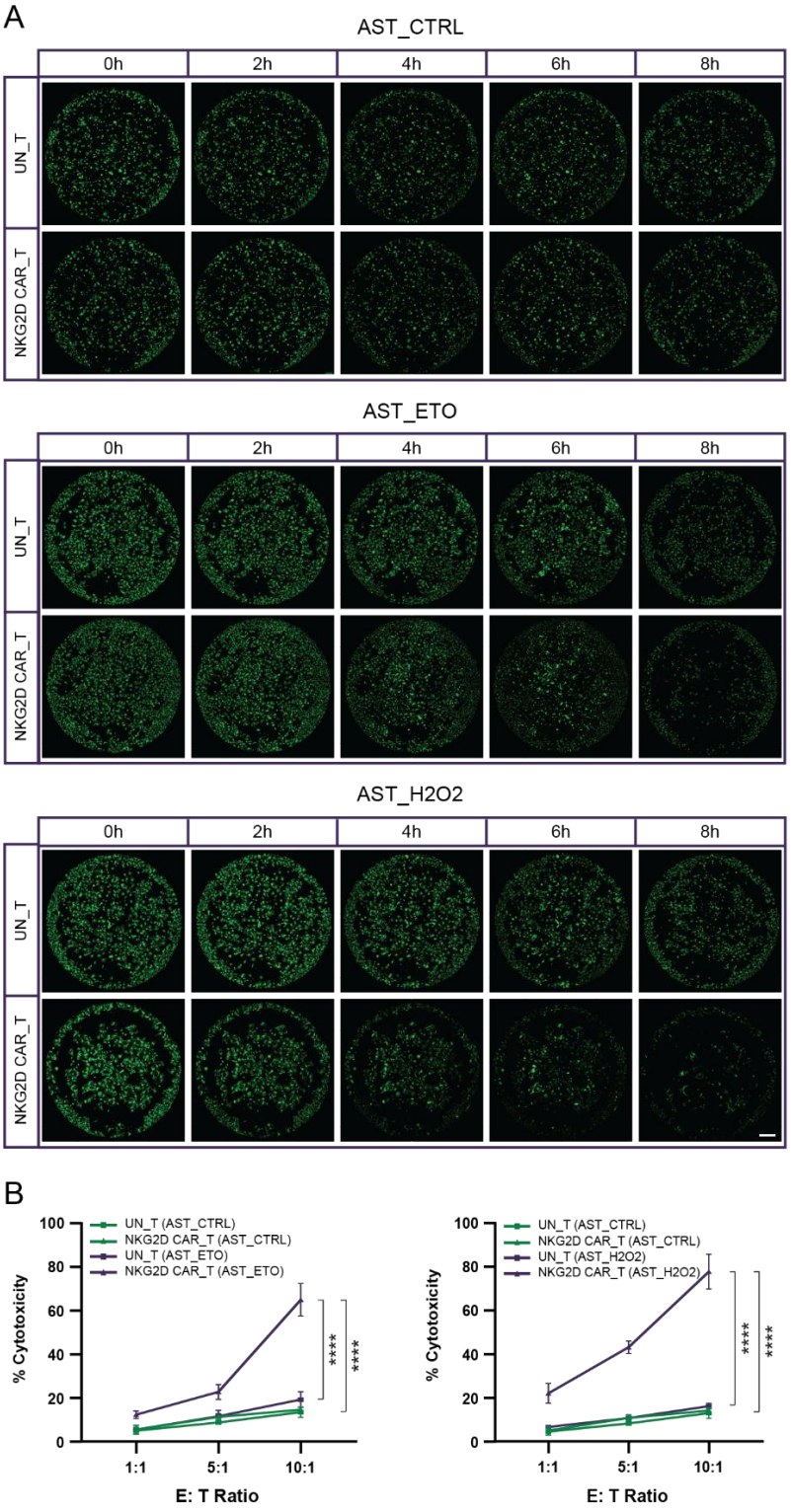

Fig. 6: Cytotoxicity of NKG2D-CAR T cells against senescent AST expressing NKG2DLs. (A) Whole-well images showing senescent AST induced by either ETO or

H2O2, and untreated proliferative AST, stained with Calcein-AM and imaged every 2 h during an 8-h co-culture with either NKG2D-CAR T cells or UN-T cells at a 10:1 E: T ratio. Scale bar = 800 μm. (B) Cytotoxicity analysis comparing the efficacy of NKG2D-CAR T cells and UN-T cells against senescent and proliferative AST, calculated after 8 h of co-culture at E: T ratios of 1:1, 5:1, and 10:1. The results are shown as the mean ± SD from four biological replicates. Significance levels are indicated by ***P < 0.001 and ****P < 0.0001, as determined by two-way ANOVA with Tukey's post-hoc tests.

3.2 MS analysis of the senescence-associated cell surfaceome

3.2.1 Cellular senescence alters the cell surface proteome

To investigate the cell surface proteome changes associated with senescence, we established various senescence models: 1) Genotoxic stress-induced senescence in NHLFs, MEFs, and mouse AST; 2) Oxidative stress-induced senescence in HUVECs, NHLFs, MEFs, and mouse AST; and 3) Proteasome stress-induced senescence in mouse AST. These senescence models were confirmed using established senescence markers, with all models showing significantly increased SA-β-gal staining (**Fig. 7**). Additionally, qPCR analysis consistently demonstrated elevated mRNA levels of p16, p21, and/or p53 across these senescence models (**Fig. 8**).

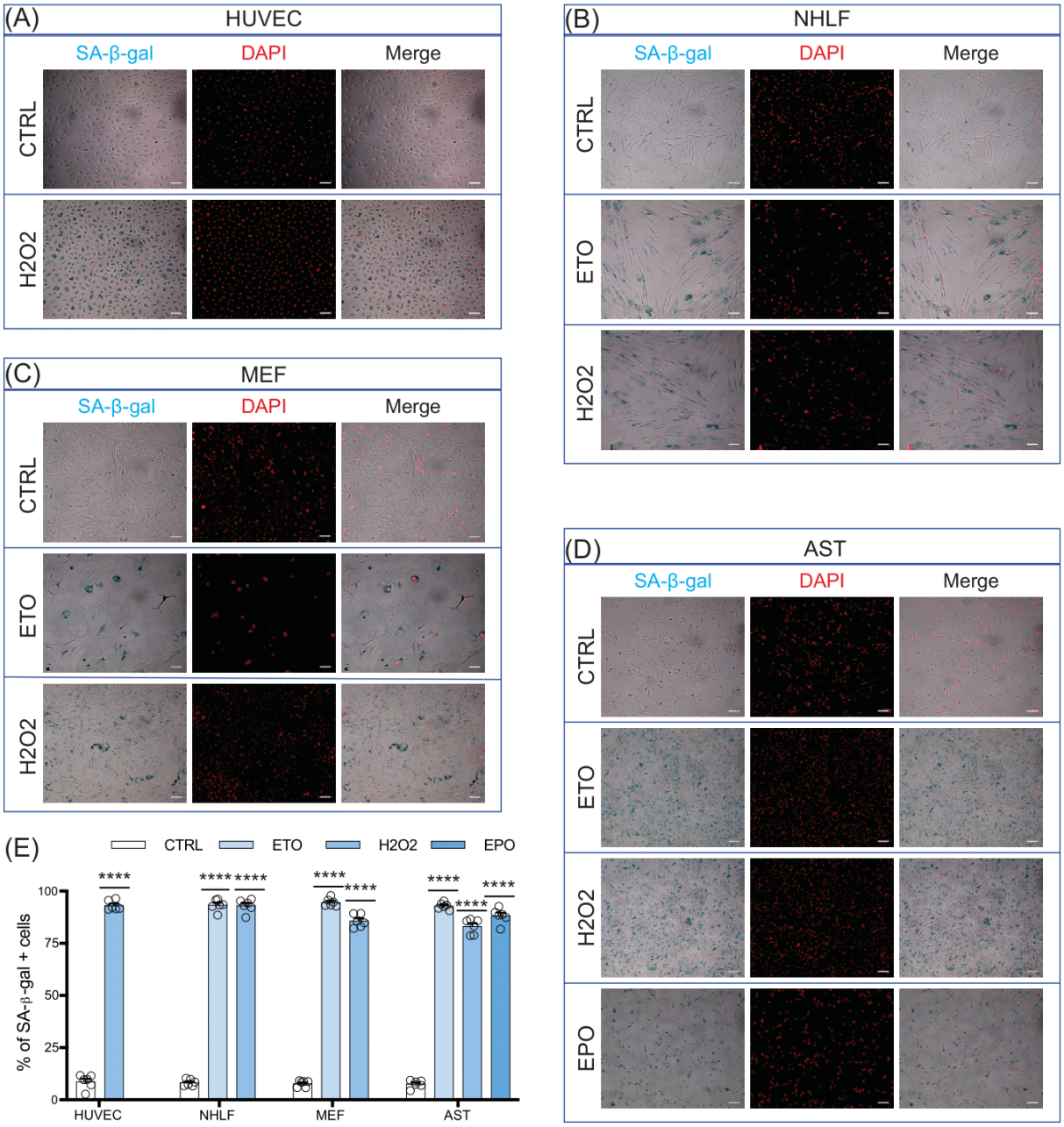

Fig. 7: SA-β-gal staining of cultured cells. (A-D) Images of SA-β-gal staining in cultured cells treated with either DMSO (control) or senescence inducers, with co-staining for SA-β-gal activity and DAPI. Positive SA-β-gal staining is visible under bright-field microscopy, indicated by blue cells. Scale bar = 100 µm. (E) Quantitative analysis of SA-β-gal-positive cells, calculated as the ratio of blue cells to DAPI-positive cells. Results are presented as the mean ± SEM from six biological replicates. Statistical significance was determined using an unpaired two-tailed Student's t-test for comparisons between two groups, and one-way ANOVA followed by Tukey's post-hoc test for analyses involving more than two groups, with ****P < 0.0001.

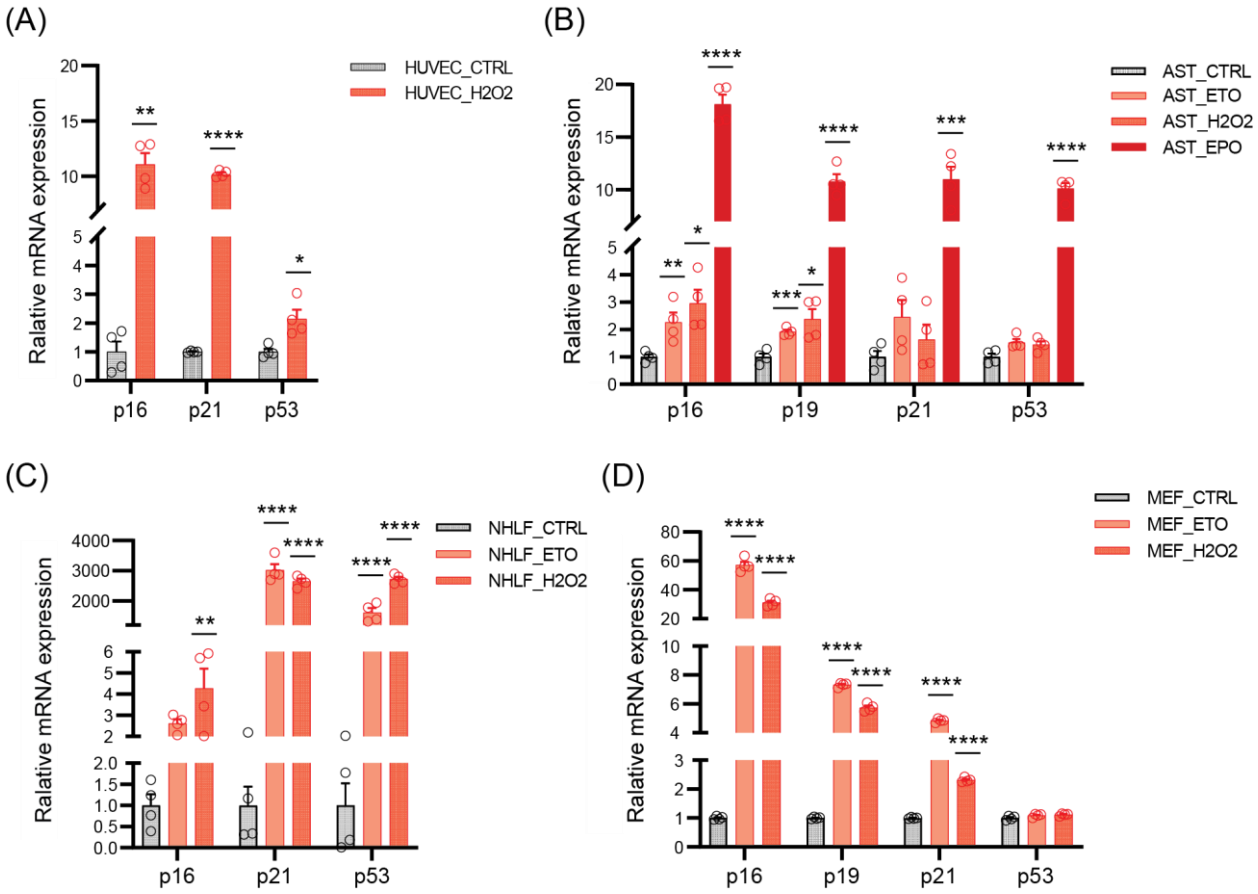

Fig. 8: RT-qPCR analysis of senescence markers. Results are normalized to β-actin mRNA levels and presented as mean ± SEM, with individual data points shown for four biological replicates. Statistical significance is indicated with *P < 0.05; **P < 0.01; ***P < 0.001; ****P < 0.0001. Statistical analysis was conducted using an unpaired two-tailed Student's t-test for comparisons between two groups and one-way ANOVA followed by Tukey's post-hoc test for multiple group comparisons.

We employed biotinylation method to enrich proteins associated with the cell surface, followed by label-free quantitative MS analysis to assess changes in their expression levels. The classification of proteins as cell surface-associated was based on their GO annotations for plasma membrane and/or extracellular regions, as indicated by the Protein Center platform integrated within the Proteome Discoverer software. In this study, approximately 32 % of all identified proteins, with a range from 29.1 % to 34.9 % across different cellular conditions, were identified as cell surface proteins (**Fig. 9**).

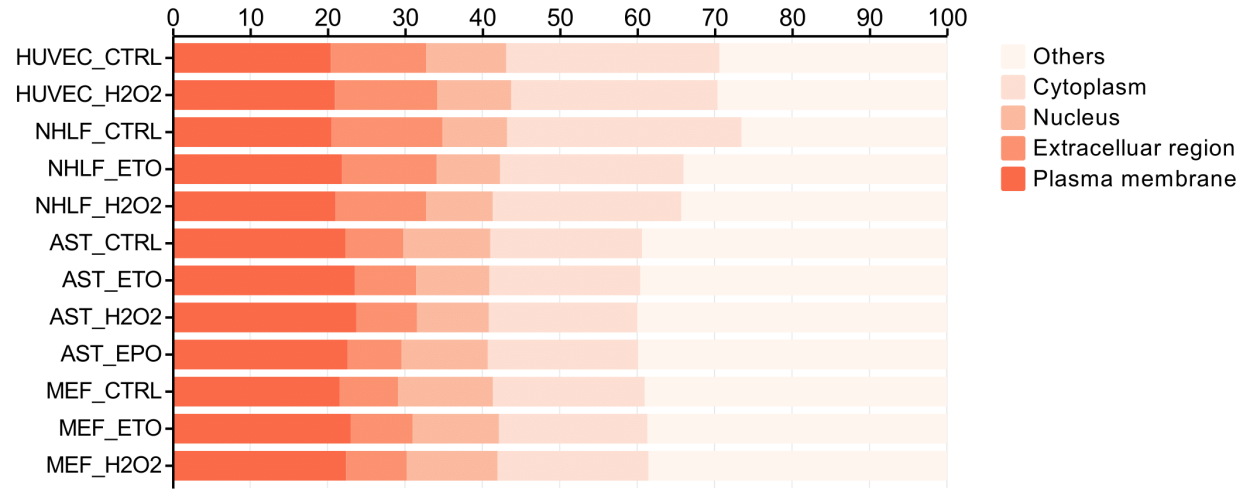

Fig. 9: Distribution of cellular components of identified proteins. The horizontal axis shows the percentage of identified proteins.

In this thesis, a comprehensive identification of cell surface proteins was performed, revealing a total of 2091 surface-associated proteins across all cell conditions. PCA was utilized to examine the clustering of these cellular conditions based on the PSM values of the identified proteins (**Fig. 10A**). The analysis showed clear separations between senescent and non-senescent cells in both PC1 and PC2, suggesting that CS profoundly modifies the cell surface proteome. Additionally, senescence conditions derived from different cell types or induced by different stressors within the same cell type displayed largely distinct clustering patterns. This highlights the influence of both the cell type and the nature of the CS inducer on the proteomic profile of the cell surface during senescence. Moreover, Pearson correlation analyses indicated strong correlations within conditions of the same cell type experiencing senescence (**Fig. 10B**). An unsupervised clustering analysis was also conducted to visualize the trajectories of surface protein expression during senescence, which underscored that the expression profiles of surface proteins varied significantly across different cell types (**Fig. 10C**).

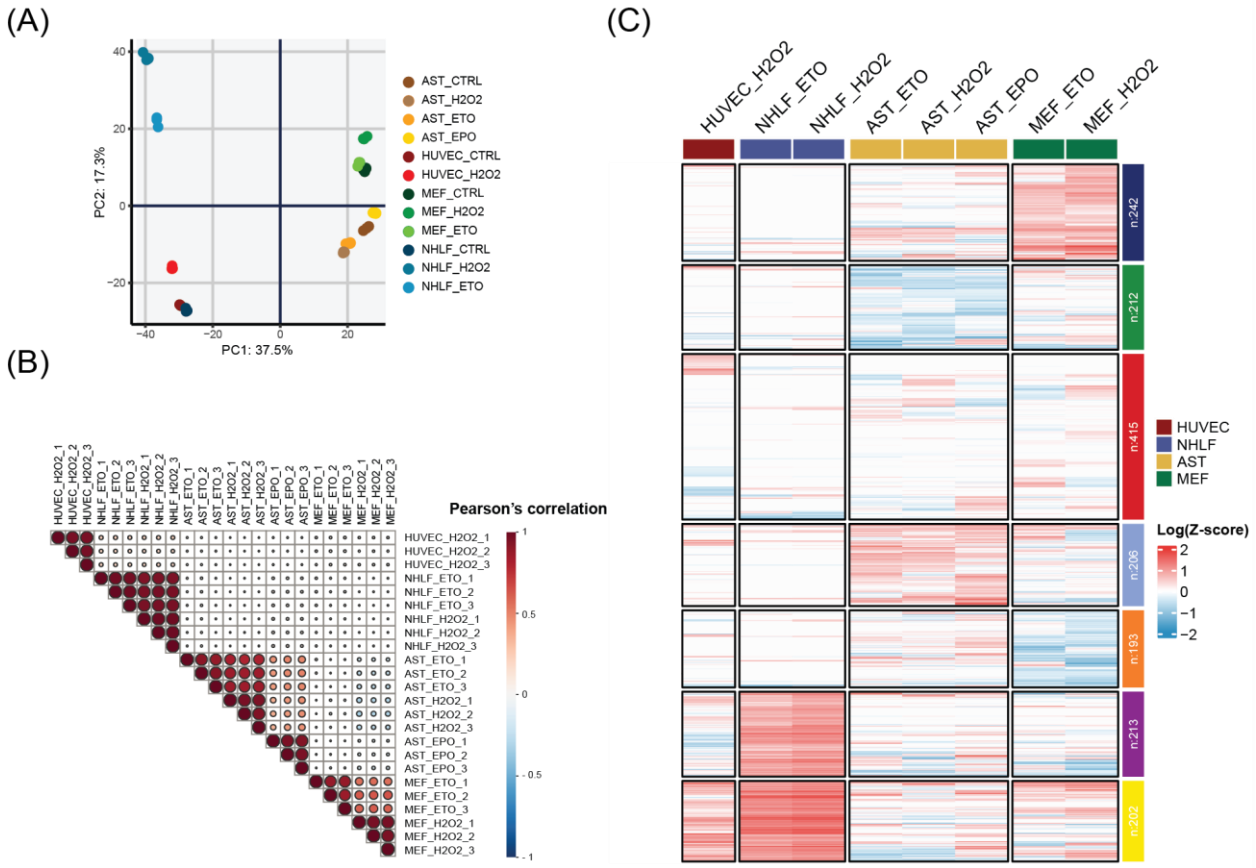

Fig. 10: Proteomic profiling of cell surface proteins across various cellular conditions. (A) PCA of proteomic profiles PSMs for all identified surface proteins (2091 proteins) across twelve different cell conditions. (B) Heat map displaying Pearson correlation coefficients that assess correlations across various cell types and senescence inducers. This analysis utilizes normalized z-scores of PSMs for all 2091 detected surface proteins, with normalization relative to their corresponding non-senescent control groups. (C) Clustering analysis of expression profiles for the 2091 surface proteins under diverse senescence conditions. The analysis scale employs a logarithmic base 10 (Log10) transformation of PSM z-scores.

3.2.2 Quantitative analysis of differential surface proteomic profiling in senescent cells

Utilizing label-free MS analysis, we conducted a quantitative comparison of cell surface proteomic profiles between senescent cells and their non-induced counterparts. We focused on proteins exhibiting significant changes, with a p-value of < 0.05 and a fold change (FC) of ≥ 1.5 (senescence/control, SEN/CTRL) (**Fig. 11A**). This comparative analysis identified between 369 and 1251 differentially expressed proteins (DEPs), with 31.1 % to 43.2 % classified as cell-surface-associated (**Fig. 11A**). Most differentially expressed cell surface proteins were significantly upregulated, though an interesting

exception was shown in senescent MEFs induced by H2O2, where 58 % of the cell surface DEPs were downregulated. Furthermore, the magnitude of protein level changes in senescent human cells was more pronounced compared to senescent mouse cells, across various cell types and inducers, as evidenced by overall log2 (FC) metrics (**Fig. 11A**).

Next, we conducted MF enrichment analysis for the DEPs within each senescence model. The analysis revealed a mix of shared and unique molecular functions within the CS surfaceome of human and mouse models, with 179 shared items and 115 and 58 items uniquely identified in *Homo sapiens* and *Mus musculus*, respectively (**Fig. 11B**). **Fig. 11C** illustrates the top 10 commonly enriched clusters across eight different senescence conditions alongside the top 10 specifically enriched clusters unique to each condition, ranked by their summed p-values. The cell adhesion molecule binding pathway emerged as the most universally shared molecular function pathway across all senescence conditions. However, distinct pathway enrichments were also observed. In particular, H2O2-induced senescent NHLFs displayed a unique profile with 34 specifically enriched clusters, predominantly featuring transporters involved in ATPase-coupled ion transmembrane transporter activity.

To investigate the interactome dynamics associated with the CS surfaceome, we performed a ligand-receptor (L-R) interaction analysis. This utilized literature-supported interactions derived from single-cell RNA sequencing datasets, available at Cellinker (Zhang et al. 2021b). The distribution of five different interaction types for each senescence scenario is visually detailed in **Fig. 11D**. We detected consistent patterns in L-R interaction distributions across the various senescent cell models in both human and mouse species, with cell-adhesion interactions being the most prevalent, accounting for 40 % to 52 % of the interactions. Besides cell-adhesion interactions, receptor-related interactions, including cytokine-cytokine receptor and extracellular matrix (ECM)-receptor interactions, were also frequently observed, ranging from 28.3 % to 44.4 %. Secreted protein-associated interactions followed, representing 14.8 % to 25 % of the total. A notable exception was found in senescent AST induced by EPO, where secreted protein to receptor interactions dominated, accounting for 60.7 % of all interactions (**Fig. 11D**).

Moreover, to explore the biological implications of CS surfaceome, we performed a BP enrichment analysis on surface DEPs in each senescence condition. Remarkably, the

number of uniquely enriched BPs in each species paralleled the number of commonly enriched ones between the two (1226 *vs.* 1284). Specifically, 796 BPs were uniquely enriched in human cells, and 488 were exclusively enriched in mouse cells (**Fig. 11E**). The Chord diagram depicted in **Fig. 11F** shown the top 10 enriched clusters, both shared and unique to each senescence condition, ranked by their summed p-values. The pathways, including cell-cell adhesion, regulation of cell migration, and vasculature development, have been involved in CS due to their mechanistic significance (Kuilman et al. 2010, Levi et al. 2020). Additionally, pathways like vesicle-mediated transportation and endocytosis, have been recognized features of the SASP in the previous study (Coppé et al. 2010). Particularly, senescent NHLFs induced by H2O2 displayed the most distinct profile, with 217 uniquely enriched clusters, especially those related to the “cellular response to increased oxygen levels” pathway.

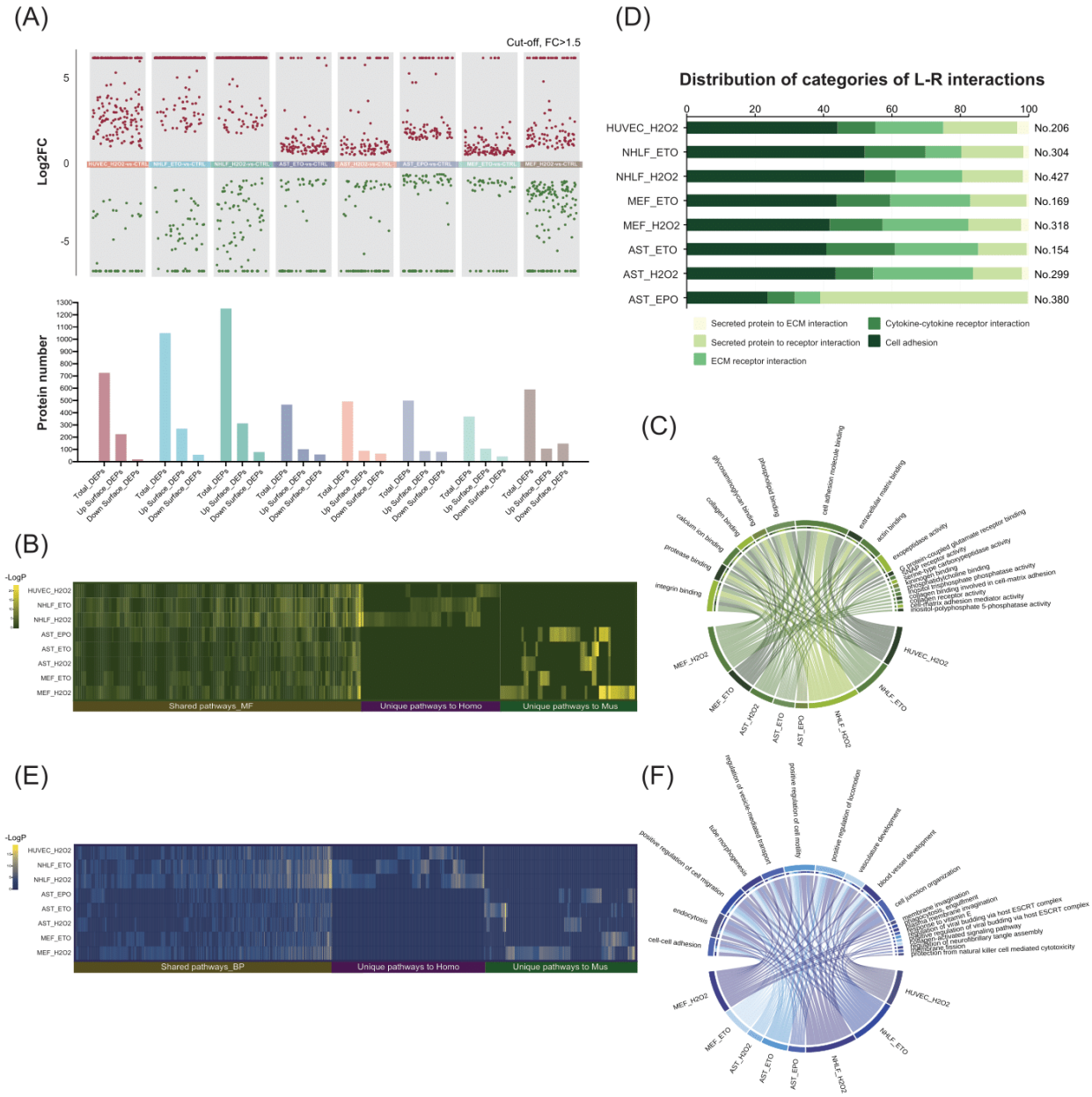

Fig. 11: Quantitative analysis of differential surface proteomic profiling in senescent cells. (A) The top panel presents multiple volcano plots representing DEPs from eight comparative analyses across various cell types under different senescence-inducing conditions. DEPs are visualized as red dots (upregulated proteins) and green dots (downregulated proteins), with a significant difference ($p < 0.05$) and a FC of at least 1.5 compared to control conditions. The y-axis represents the log2 (FC) of SEN/CTRL. The bar chart details the total number of DEPs and cell surface DEPs identified. (B, E) Heat maps show the -log(p-values) from GO-based MF and BP enrichment analyses of surface DEPs, mapped against their respective MF or BP processes. (C, F) Chord diagrams show the top 10 most commonly and uniquely enriched terms among surface DEPs in all senescent conditions. (D) This panel displays the distribution and total number of L-R interaction categories derived from surface DEPs across eight studied senescence

scenarios. The horizontal axis indicates the proportions of L-R interaction categories within surface DEPs under different senescence conditions.

3.2.3 Shared surfaceome and its contribution to senescence signature

Senescent cells universally exhibit morphological alterations, cell-cycle arrest, and SASP characteristics (Hernandez-Segura et al. 2018). In the current thesis, we aimed to identify senescence-associated cell surface molecules that are commonly shared across various senescent cell models. We identified a set of 27 proteins that were consistently differentially expressed across three human senescence paradigms (**Fig. 12A**). Notably, 16 of these proteins (59.2 %) showed an increase in expression levels, whereas a minor fraction (11.1%) displayed significant reductions in abundance across all examined human cell models (**Fig. 12B**). To explore the potential functional relationships among these commonly upregulated proteins in human senescence models, we conducted a BP enrichment analysis. This analysis highlighted several pathways, including neutrophil degranulation, sterol metabolic processes, negative regulation of proteolysis, and monoatomic cation transport (**Fig. 12C**). Furthermore, we analyzed the overlap in surface DEPs across different mouse senescence models. Only one protein, N(4)-(beta-N-acetylglucosaminyl)-L-asparaginase (AGA), was consistently upregulated across all five mouse senescence models (**Fig. 12D**).

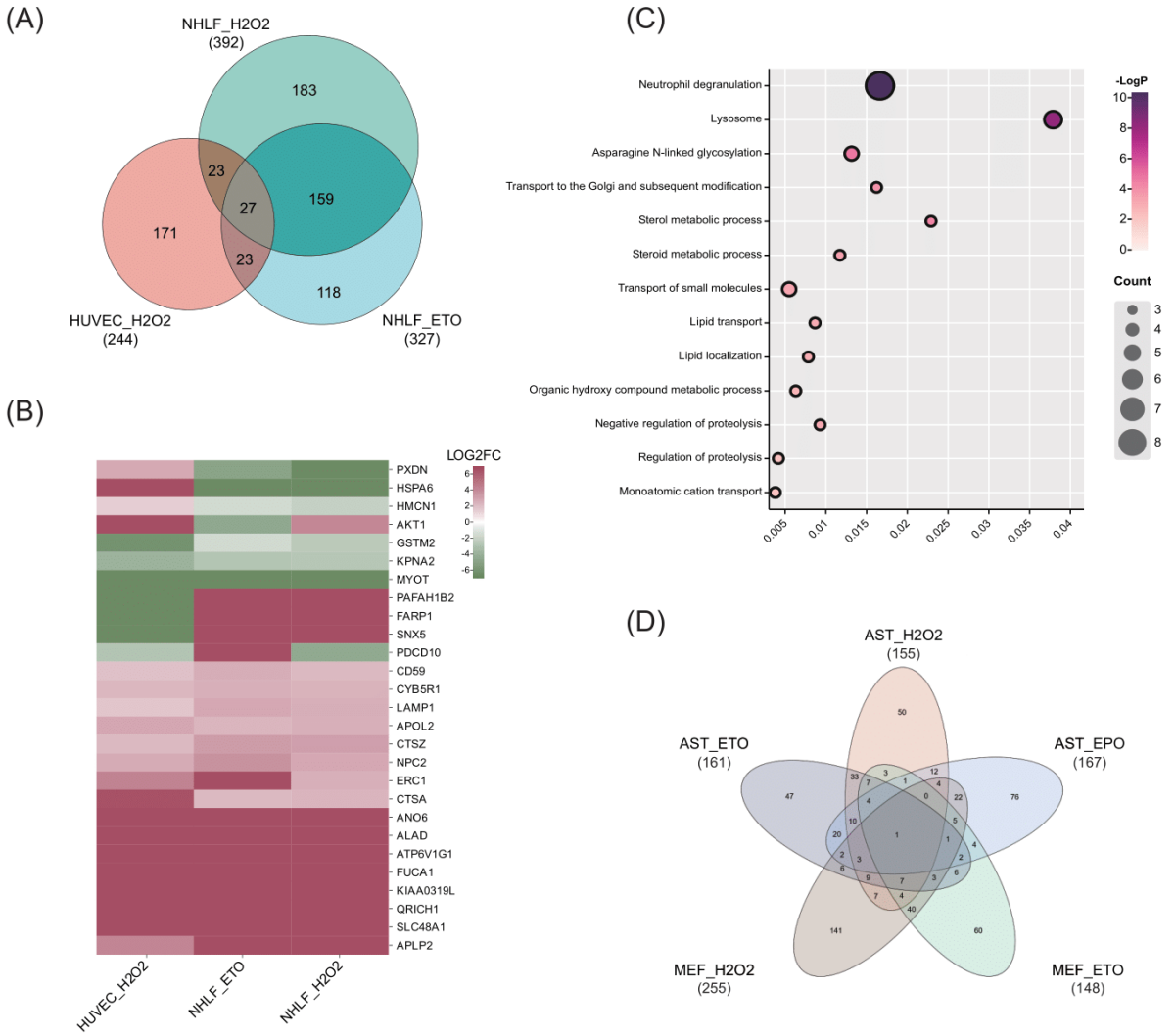

Fig. 12: Shared surfaceome and its contribution to senescence signature. (A) The Venn diagram displays the number of cell surface DEPs and their overlaps across three human senescence comparisons. (B) The heat map shows the senescence-associated changes in expression across 27 shared human surface DEPs, visualized by the log2 (FC) of the respective SEN/CTRL comparison. (C) This panel shows the biological pathways enriched among the shared upregulated human surface DEPs. The horizontal axis represents the gene ratio, which indicates the ratio of DEPs-coded genes within a given pathway to the total number of genes in this pathway. The size of each bubble indicates the number of protein-coding genes enriched in the pathway, while the color scale reflects the -log10(p-value) of enrichment. (D) The Venn diagram displays the overlap of surface differential expression profiles among the five mouse senescence comparisons.

3.2.4 Heterogeneity of senescence surfaceome across cell types

To assess how different cell types influence the CS surfaceome, we performed comparative analyses of surface DEPs in three scenarios: 1) senescent human endothelial cells *vs.* lung fibroblasts induced by oxidative stress (**Fig. 13A**); 2) senescent

mouse astrocytes *vs.* fibroblasts induced by oxidative stress; and 3) senescent mouse astrocytes *vs.* fibroblasts induced by DNA damage (**Fig. 13D**, **G**). Our findings revealed that only 12.8 % to 22.6 % of DEPs were common to each comparison, with 37.1 % to 61.2 % of proteins being upregulated, 8 % to 20 % downregulated, and notably, 19.4 % to 42.9 % showing opposing changes in response to the same CS inducers (**Fig. 13B**, **E**, **H**). Further analysis was conducted to explore whether the functional attributes of the CS surfaceome vary between different cell types. The top 10 GO-enriched clusters for each comparison of both upregulated and downregulated surface proteins are visualized in **Fig. 13C**, **F**, **I**, highlighting distinct highly enriched biological pathways within each comparative scenario.

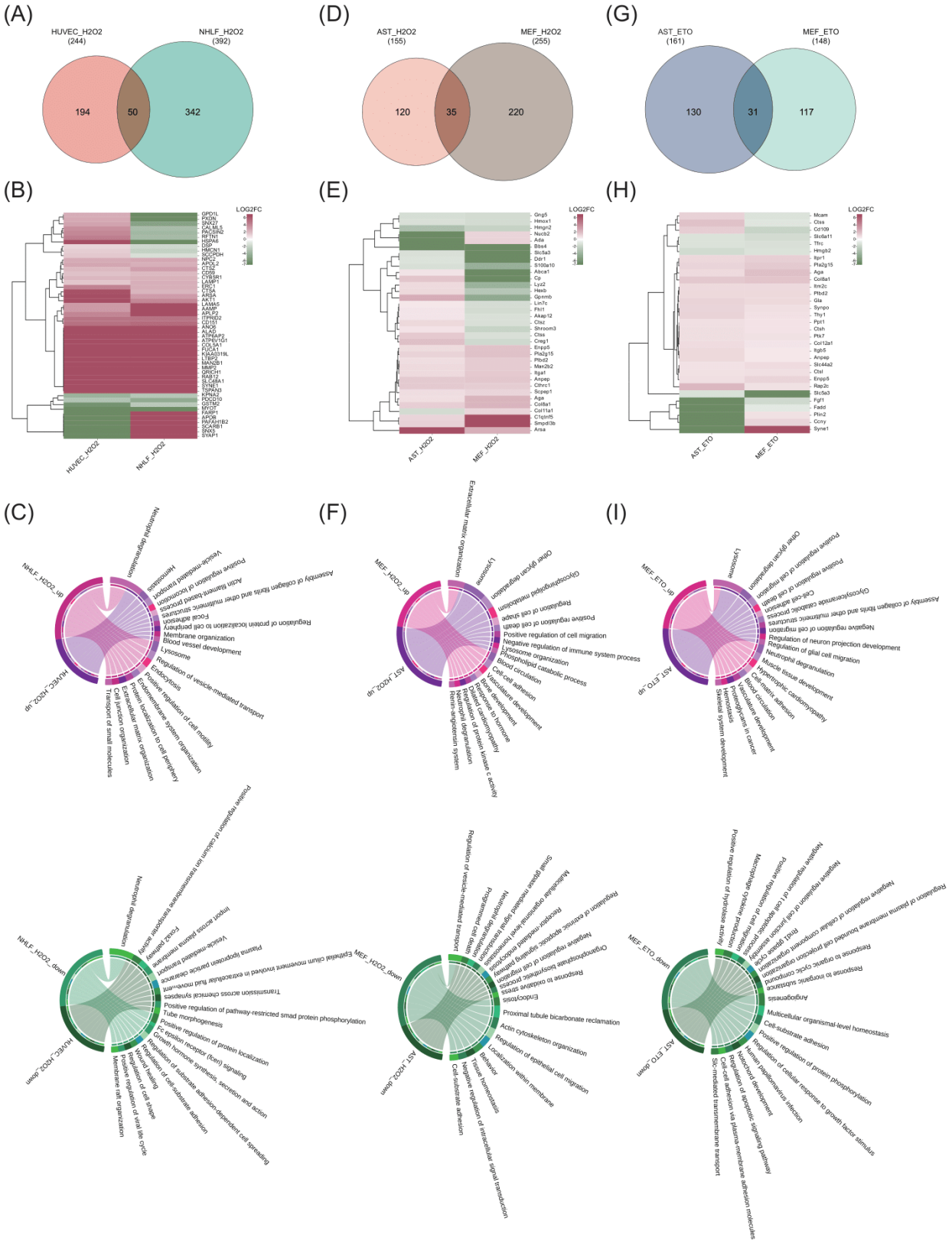

Fig. 13: Heterogeneity of senescence surfaceome across cell types. (A, D, G) Venn diagrams show the number of surface DEPs and their overlap when induced by the same senescence inducers (either oxidative stress or genotoxic stress) across different cell types. (B, E, H) The heat maps display the senescence-associated expression changes

for overlapping surface DEPs, identified from each comparison in (A, D, G), based on the log2 (FC) of SEN/CTRL. (C, F, I) The chord diagrams illustrate the top 10 enriched biological pathways for both upregulated (displayed in red) and downregulated (shown in green) cell surface proteins within each senescence comparison.

3.2.5 Senescence inducer-dependent surfaceome changes

To assess the effects of different senescence inducers on surface DEPs within the same cell type, we conducted comparative analyses using senescent human lung fibroblasts, mouse fibroblasts, and mouse astrocytes treated with either the DNA-damaging agent ETO or the ROS inducer H2O2. Notably, nearly half of the surface DEPs (41.1 % to 55.9 %) were consistently activated by both inducers across the same cell types (**Fig. 14A**). Furthermore, BP enrichment analysis of the shared surface DEPs highlighted pathways such as neutrophil degranulation, cell-cell adhesion, and positive regulation of cation transmembrane transport as robustly activated by both inducers (**Fig. 14B**).

We also investigated the potential for identifying the origin of CS based on inducer-specific surface markers. This was achieved by characterizing the proteomic signatures unique to different CS inducers (ETO, H2O2, and EPO) across various cell types (**Fig. 14A**, **C**). Pathways distinctly linked to specific stressors were identified and are shown in **Fig. 14D**. At the molecular level, our focus was on inducer-specific CS surface markers that were exclusively associated with distinct CS drivers and consistently upregulated in at least two different cell types. Considering the lack of a RS model in this thesis, we integrated data from two previously published studies involving RS models: a whole transcriptome study in MEFs (Chen et al. 2018) and a surface proteome study in human primary fibroblasts BJ (Mrazkova et al. 2018). After excluding molecules overlapping with markers activated under RS conditions, we identified unique proteins linked to specific inducers. For ETO, six proteins including inositol 1,4,5-trisphosphate receptor type 1 (ITPR1) and palmitoyl-protein thioesterase 1 (PPT1) emerged as ETO-specific CS surface signatures. In the context of H2O2-induced senescence, seven proteins such as sphingomyelin phosphodiesterase acid like 3B (SMPDL3B) and collagen triple helix repeat containing 1 (CTHRC1) were identified as unique markers. Additionally, eleven proteins demonstrated strong and exclusive upregulation after EPO treatment (**Fig. 14E**, **Tab. 9**).

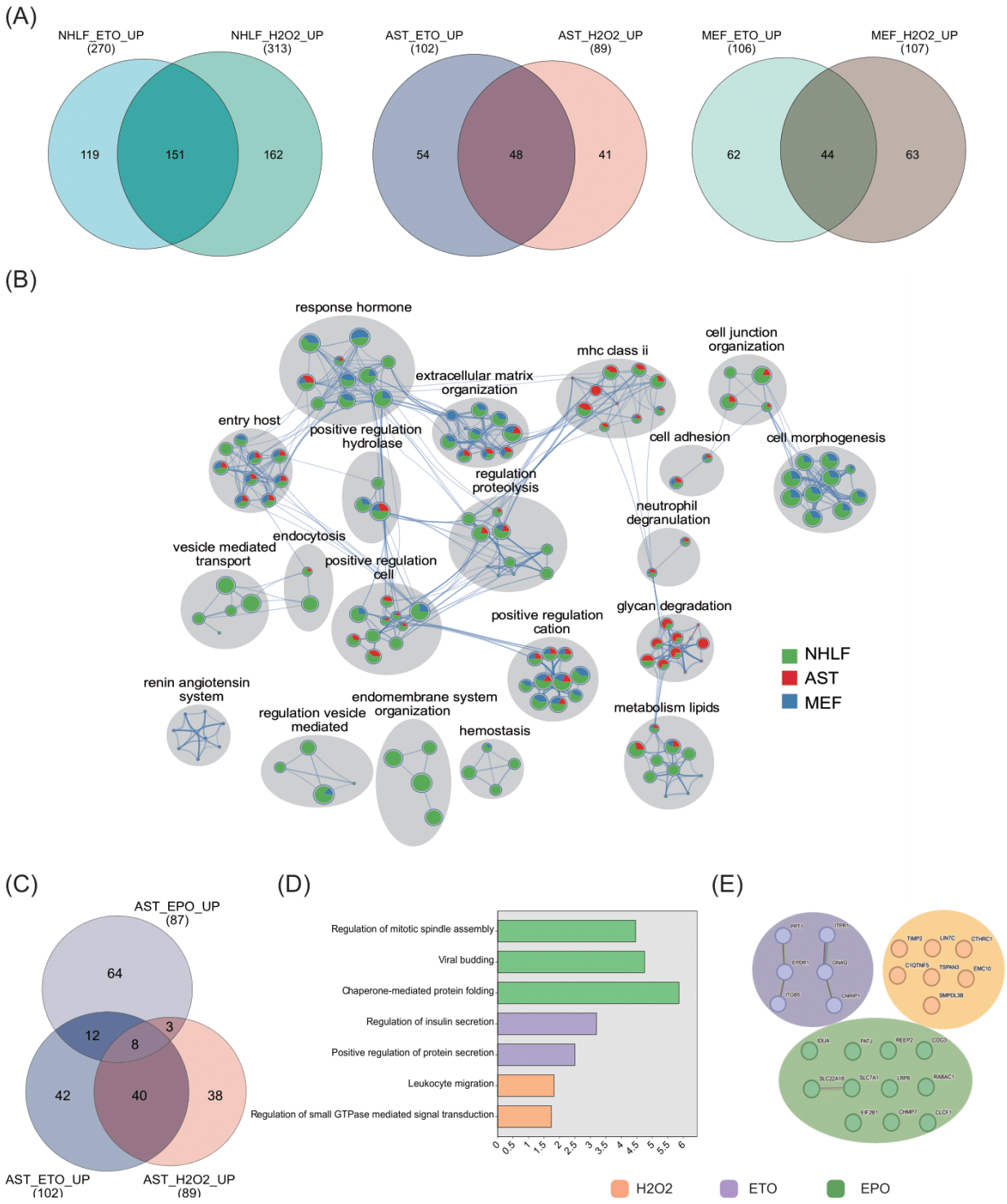

Fig. 14: Senescence inducer-dependent surfaceome changes. (A, C) Venn diagrams illustrate the overlap of upregulated surface proteins across senescence comparisons within the same cell type, but induced by different senescence-inducing stimuli. (B) Network plot shows enriched biological pathways for surface proteins upregulated in both oxidative and genotoxic stress-induced senescence. Nodes represent enriched terms as pie charts, color-coded by cell type (NHLFs in green, mouse astrocytes in red, MEFs in blue), with sizes indicating the number of hits and slices showing the distribution of protein-

coding genes. (D) This chart displays biological pathways enriched among surface proteins uniquely activated by specific inducers but shared across cell types, plotted by -log10(p-value). (E) String protein-protein interaction analysis shows interactions among inducer-specific senescence surface markers shared by different cell types. Nodes represent markers, color-coded by inducer, with edges indicating the type and confidence of interactions (interactions derived from curated databases in blue, co-expression interactions in black, text-mining interactions in green, and experimentally determined interactions in pink; the thicker the edge, the higher the confidence).

Tab. 9: Inducer-specific senescence surface markers.

ETO		
Gene Symbol	**UniProt Accession**	**UniProt Protein Name**
GNAQ	P50148	Guanine nucleotide-binding protein G(q) subunit alpha
EPDR1	Q9UM22	Mammalian ependymin-related protein 1
CNRIP1	Q96F85	CB1 cannabinoid receptor-interacting protein 1
PPT1	P50897	Palmitoyl-protein thioesterase 1
ITGB5	P18084	Integrin beta 5
ITPR1	Q14643	Inositol 1,4,5-trisphosphate receptor type 1
H2O2		
Gene Symbol	**UniProt Accession**	**UniProt Protein Name**
TSPAN3	O60637	Tetraspanin-3
TIMP2	P16035	Metalloproteinase inhibitor 2
EMC10	Q5UCC4	ER membrane protein complex subunit 10
LIN7C	Q9NUP9	Protein lin-7 homolog C
SMPDL3B	Q92485	Acid sphingomyelinase-like phosphodiesterase 3b
C1QTNF5	Q9BXJ0	Complement C1q tumor necrosis factor-related protein 5
CTHRC1	Q96CG8	Collagen triple helix repeat-containing protein 1
EPO		
Gene Symbol	**UniProt Accession**	**UniProt Protein Name**
Q14232	EIF2B1	Translation initiation factor eIF-2B subunit alpha

Q9BRK0	REEP2	Receptor expression-enhancing protein 2; Receptor expression-enhancing protein
Q8WUX9	CHMP7	Charged multivesicular body protein 7
Q96JB2	COG3	Conserved oligomeric Golgi complex subunit 3
P30825	SLC7A1	High affinity cationic amino acid transporter 1
Q9UI14	RABAC1	Prenylated Rab acceptor protein 1
Q8NI35	PATJ	InaD-like protein
O75581	LRP6	Low-density lipoprotein receptor-related protein 6
Q96BI1	SLC22A18	Solute carrier family 22-member 18
Q9UBD9	CLCF1	Cardiotrophin-like cytokine factor 1
P35475	IDUA	Alpha-L-iduronidase

3.2.6 Identification of potential senotherapeutic targets

To identify potential senotherapeutic targets that are prominently and selectively expressed in senescent cells but minimally in normal tissues, we analyzed the expression profiles of shared upregulated CS surface markers identified in this thesis, 16 in human cells and 1 in mouse cells, across various human tissues using data from the Human Proteome Map (HPM) (Kim et al. 2014) (**Fig. 15A**). Among these, cytochrome b5 reductase 1 (CYB5R1) demonstrated relatively low expression levels across diverse human tissues, which is in line with low CYB5R1 mRNA levels observed in adult mouse tissues according to RNA-seq data from the “European Molecular Biology Laboratory (EMBL-EBI) Expression Atlas” (Geiger et al. 2013, Merkin et al. 2012) (**Fig. 16E**, **Tab. 10**). Further extending our analysis to identify potential surface targets relevant to both *Homo sapiens* and *Mus musculus*, we selected all surface DEPs identified in at least one senescence condition within each species and determined their homologues in the other species using the biological database network bioDBnet (tool db2db). 704 cell surface DEPs in human senescent cells, with 658 proteins having murine counterparts were identified. Similarly, among the 589 cell surface DEPs from mouse senescent cells, 574 proteins have human homologues. A comparison revealed 153 cell surface proteins with senescence-associated differential expression in both species, including 69 proteins upregulated in at least two senescence conditions (**Fig. 16A**, **B**). Among these

upregulated cell surface proteins, glutathione peroxidase 7 (GPX7), fragile X messenger ribonucleoprotein 1 (FMR1), plexin A1 (PLXNA1), and protein tyrosine kinase 7 (PTK7) showed either absent or low expression levels across both species (**Fig. 16E**, **F**, **Fig. 15B** and **Tab. 10**). To further broaden the identification of potential targetable CS surface markers, we compared our findings from human senescent-cell-derived cell surface DEPs with established CS signatures from previous transcriptomic (Casella et al. 2019, Hernandez-Segura et al. 2017) and proteomic datasets (Kim et al. 2017, Mrazkova et al. 2018). This analysis revealed 32 cell surface molecules that overlapped with reported upregulated CS signatures, among which plexin A3 (PLXNA3) presented at very low levels across various tissues in both humans and mice (**Fig. 16C**-**F**, **Fig. 15C** and **Tab. 10**). This identification extends to PTK7, previously identified as a CS surface marker in a RS model of human fibroblasts BJ (Mrazkova et al. 2018).

Tab. 10: Expression levels of six potential senotherapeutic targets in normal adult mouse tissues.

Expression Atlas # E-MTAB-2801 **Expression level cut-off: 0 Transcripts Per Million**								
TPM (Transcripts Per Million) in vital tissues								
Targets	**brain**	**colon**	**kidney**	**liver**	**lung**	**spleen**	**skeletal muscle**	**testis**
PLXNA1	54	4	13	5	66	27	11	27
PLXNA3	33	1	2	0.3	4	9	0.8	0.7
CYB5R1	15	9	20	6	28	40	50	24
PTK7	8	3	6	0.4	39	18	0.6	5
FMR1	40	4	13	5	19	29	4	8
GPX7	8	3	3	4	30	5	11	0.9
Expression Atlas # E-PROT-11 **Expression level cut-off: 0 Parts Per Billion**								
PPB (Parts Per Billion) in vital tissues								
Targets	**cerebellum**	**ovary**	**kidney**	**liver**	**lung**	**spleen**	**heart**	**white adipose**
GPX7	/	117.859	/	/	/	/	3.441	/
PTK7	/	8.445	/	/	2.793	2.155	0.742	/
PLXNA1	0.568	/	0.029	0.011	/	0.053	/	0.089

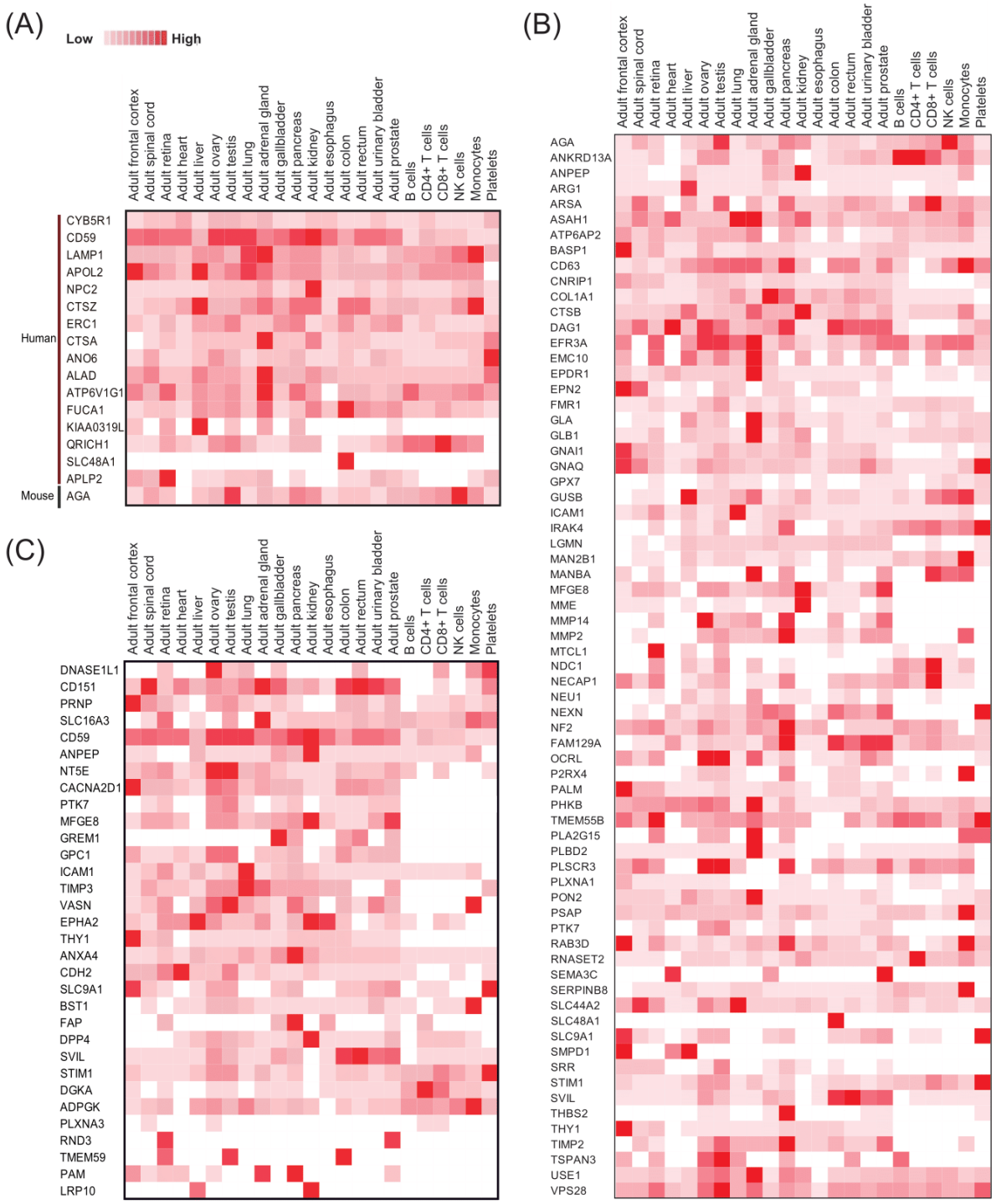

Fig. 15: Expression profiles of identified upregulated senescence surface markers in human normal tissues. (A) Heat maps show the expression profiles in human normal tissues for upregulated surface markers shared across human (16 proteins) or mouse (1 protein) senescence models, (B) 69 upregulated cell surface proteins identified from at least one senescence condition and shared between *Homo sapiens* and *Mus musculus*, and (C) 32 surface molecules common to DEPs in senescent human cells with murine homologues in this thesis, also identified as upregulated markers in published

transcriptome and proteome data. The y-axis lists the protein names. The heat maps in this figure are generated via the Human Proteome Map (HPM).

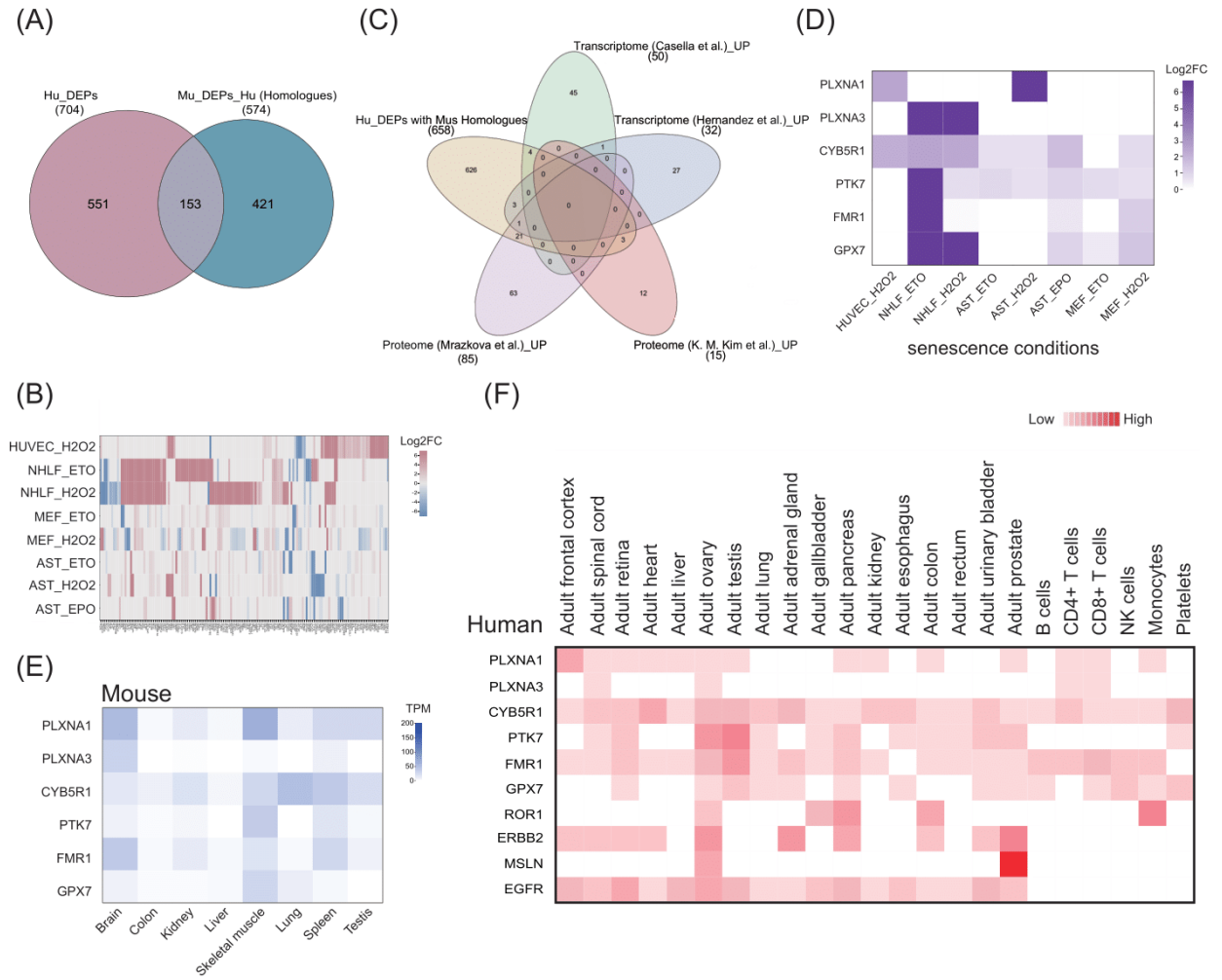

Fig. 16: Identification of potential senotherapeutic targets. (A) Venn diagram displays the number of surface DEPs identified in at least one senescence condition, showing overlaps between *Homo sapiens* and *Mus musculus*. (B) Heat map Illustrates the expression profiles of 153 overlapping surface DEPs between the two species, analyzed based on the log2 (FC) of SEN/CTRL. (C) Venn diagram comparing surface DEPs derived from human (Hu) senescent cell conditions with murine (Mu) homologues and upregulated senescence signatures from published transcriptome and proteome studies. (D, E, F) Heat maps show the expression profiles of six identified potential senotherapeutic targets across eight senescence conditions, analyzed based on log2 (FC) of SEN/CTRL (D), mRNA levels in adult mouse tissues as determined by published RNA-sequence datasets (E), and protein levels in adult human tissues as determined by the HPM combined with the expression profiles of known CAR-T cell therapeutic targets in clinical trials (F). ROR1, inactive tyrosine-protein kinase transmembrane receptor ROR1; ERBB2, receptor tyrosine-protein kinase erbB-2; MSLN, mesothelin; EGRR, epidermal growth factor receptor.

3.2.7 Validation of potential senotherapeutic targets in aging and age-related disease *in vivo*

CS contributes to natural aging and various age-related pathologies (He and Sharpless 2017). To explore if the CS surface signature identified in the current thesis overlaps with known aging biomarkers, we integrated data from two aging studies into our analysis: GenAge (de Magalhães et al. 2009) and SOMAscan (Tanaka et al. 2018). GenAge compiles age-related genes from studies spanning mice, rats, and humans, while SOMAscan identifies aging-related protein markers in healthy human plasma. After comparison, 32 and 18 proteins overlapped with GenAge (accounting for 8.6 % of all GenAge markers and 9 % after excluding rat genes) and SOMAscan (8.3 % of all SOMAscan), respectively (**Fig. 17A**).

To further determine the potential of our candidate CS cell surface markers as senotherapeutic targets in aging tissues *in vivo*, we assessed the mRNA levels of four candidates, PLXNA1, PLXNA3, PTK7, and CYB5R1, in young and old wild type mice, as well as in brains of APP/PS1 mutant mice. These candidates are characterized by cell membrane localization with extracellular epitopes, as depicted in schematic visualizations available through Protter (https://wlab.ethz.ch/protter/start/) and shown in **Fig. 18**. Our qPCR analysis showed significantly elevated mRNA levels of PLXNA1 in the brain and testis of old mice (20-month-old) compared to young counterparts (3-month-old) (**Fig. 17B**). Moreover, in AD mouse model, elevated expression levels of PLXNA1 and PLXNA3 were observed in the brain at 4 months of age, while PTK7 expression increased at 11 months (**Fig. 17C**).

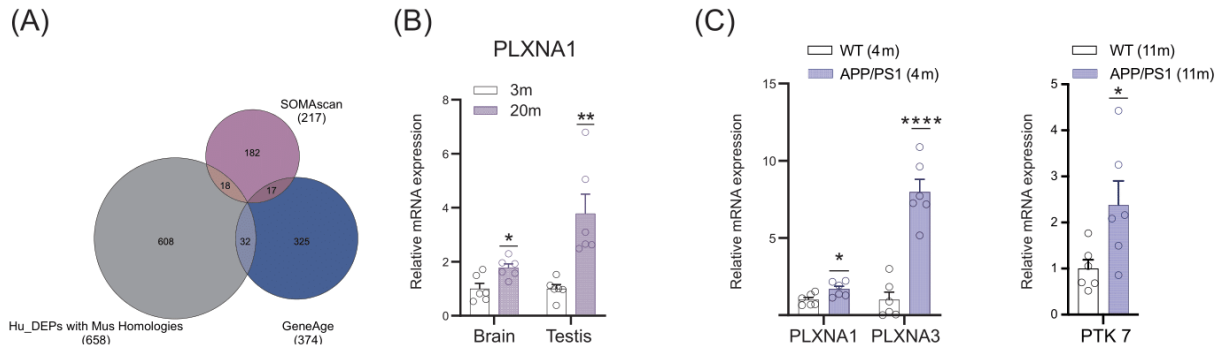

Fig. 17: Validation of potential senotherapeutic targets in aging and age-related disease *in vivo*. (A) Venn diagram shows comparison between the human senescence-condition derived surface DEPs with murine homologues and aging biomarkers identified

in GenAge and SOMAscan studies. (B, C) mRNA levels of four potential senotherapeutic targets in tissues of young (3-month-old) and old (20-month-old) WT male mice (B) and in brain of APP/PS1 mice (C), determined by RT–qPCR. Data are shown as the mean ± SEM of six biological replicates; normalized to β-actin mRNA level. *P < 0.05; **P < 0.01, analyzed using Student's t-test).

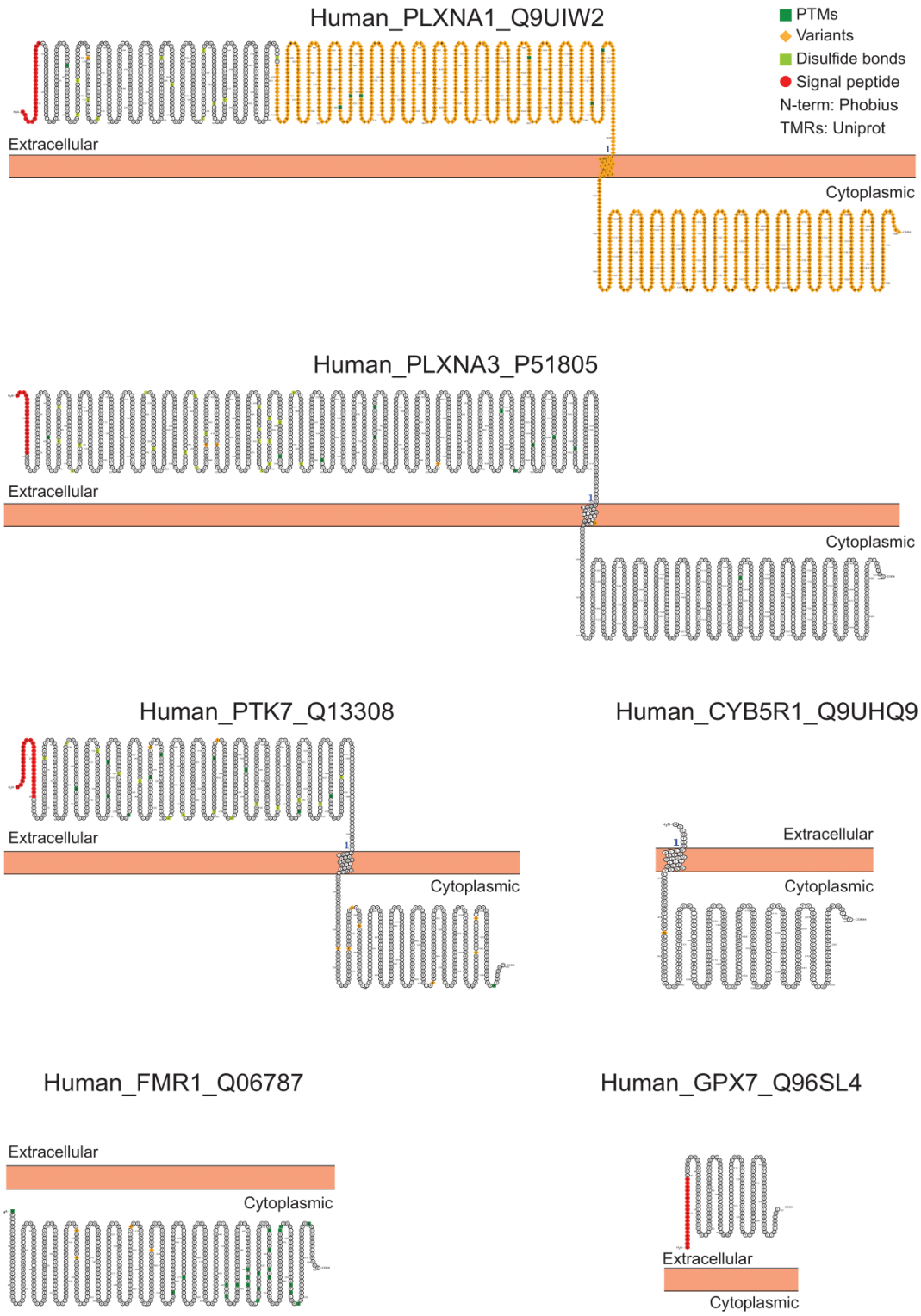

Fig. 18: The schematic representation of the protein sequences for six identified potential senotherapeutic targets. Each target protein is annotated with its respective UniProt accession number. The visualization was generated using the Protter protein-visualization platform.

4. Discussion

4.1 T cells engineered with NKG2D-CAR target and eliminate stress-induced senescent cells

4.1.1 Summary of this study

The accumulation of senescent cells is increasingly recognized as a contributor to a variety of age-related changes and pathologies, sparking significant interest in developing therapeutics aimed at elimination of senescent cells from tissues (Chaib et al. 2022, Childs et al. 2015, Gasek et al. 2021, Tchkonia et al. 2013, Wiley and Campisi 2021). Despite some agents that induce apoptosis in senescent cells or block the SASP have shown therapeutic promise, their application is often hindered by low specificity and off-target effects (Zhang et al. 2023). Immunotherapeutic strategies, particularly CAR-T cells, traditionally used for targeting specific cancer antigens, are now being explored for their potential against senescent cells (Song et al. 2020).

Unlike cancer cells, senescent cells generally do not produce an immunosuppressive microenvironment that could inhibit T cell activity (Anderson et al. 2017, Pellegatta et al. 2018), which may facilitate the effectiveness of CAR-T cell therapies. Additionally, the SASP of senescent cells could play a supportive role by enhancing the trafficking and infiltration of these adoptive CAR-T cells into tissues (Feucht and Abou-El-Enein 2020). Supporting this notion, there is emerging evidence from mouse models demonstrating the efficacy of CAR-T cells targeting uPAR-expressing senescent cells in conditions like lung adenocarcinoma and liver fibrosis (Amor et al. 2020). These findings suggest that targeting specific senoantigens with CAR-T cells could be a promising strategy to remove senescent cells with high specificity.

While CAR-T cells offer enhanced precision in targeting senescent cells, the effectiveness of this senolytic therapy hinges significantly on the accurate identification of senoantigens. Given the heterogeneous and dynamic nature of senescent cells (Casella et al. 2019, Hernandez-Segura et al. 2018), identifying broadly expressed senoantigens is still a challenge. NKG2D, an innate cell-surface receptor found on NK cells and some T-cell subsets, plays a crucial role in the immunological surveillance of cancer cells (Prajapati et al. 2018). Its ligands are typically lowly expressed in healthy cells but are induced under various stress conditions including DNA damage, oxidative stress, viral infections, and

cellular transformation (González et al. 2008). There is consistent evidence showing the upregulation of NKG2DLs in various senescent cells both *in vitro* (Kim et al. 2008, Krizhanovsky et al. 2008, Sagiv et al. 2016, Soriani et al. 2009, Yang et al. 2023) and in senescent skin fibroblasts from elderly individuals *in vivo* (Hasegawa et al. 2023). Recent studies have demonstrated that eliminating senescent cells using NKG2D-CAR T cells can ameliorate several age-related physiological changes and pathologies in both naturally aged and irradiated mice (Yang et al. 2023).

Based on the stress-sensing capabilities of NKG2DLs, we engineered NKG2D-based CARs by fusing the full length of murine NKG2D receptor coding sequence, serving as both the extracellular recognition and transmembrane domain, to the CD3ζ signaling domain (NKz-CARs) as previously described (Driouk et al. 2020, Zhang et al. 2005). We constructed models of genotoxic stress- and oxidative stress-induced senescence using mouse MEFs and AST. Our findings confirmed the broad elevation of mouse NKG2DLs on the surface of these stress-induced senescent cells. Notably, T cells engineered to express NKG2D-CAR demonstrated selective and cytotoxicity against NKG2DLs-expressing senescent AST and MEFs, thereby supporting the potential of NKG2D-CAR T cells as effective senolytics in aging and age-related diseases.

4.1.2 Design considerations for balancing the efficacy and safety of NKz-CAR T cells

The efficacy and safety of CAR-T therapies are influenced significantly by the specifics of CAR design (Gacerez et al. 2016). Unlike the designs of traditional second-generation CAR that incorporate costimulatory domains like CD28 or CD137 to enhance T cell activation and persistence (Gacerez et al. 2016), NKz-CAR leverages the natural signaling capabilities of the NKG2D receptor. This receptor inherently associates with costimulatory molecules DNAX-activating protein 10 (DAP10) in humans and/or DAP12 in mice, thus engaging the PI3K pathway to provide costimulation alongside CD3ζ signaling (Barber and Sentman 2011, Raulet 2003). Such a configuration suggests that NKz-CARs function as the second-generation CARs, effectively utilizing dual signaling pathways to activate T cells. In this thesis, NKz-CAR T cells demonstrated effective targeting of NKG2DL-expressing B16F10 cells, in line with previous findings of NKG2DL-positive tumor cell elimination by similarly modified T cells (Driouk et al. 2020, Weiss et al. 2018, Zhang et al.

2005). This confirms the binding affinity of NKz-CARs. However, the expression of human NKG2DLs such as MICA and MICB on normal intestinal epithelial cells (Groh et al. 1996) and the presence of the mouse ligand Mult1 in various normal tissues (Carayannopoulos et al. 2002) raise concerns about potential off-target effects of NKG2D-CAR T cell therapy. Optimal binding affinity is therefore crucial, enabling effective target engagement and execution of T cell effector functions while minimizing on-target but off-tumor effects, particularly when targeting antigens expressed at low levels on healthy cells. Notably, severe toxicity was observed in BALB/c and C57BL/6 mice with DAP10 or CD28 fused-NKz-CAR T cells, but not with NKz-CAR T cells alone (VanSeggelen et al. 2015), suggesting that the short-term persistence of NKz-CAR T cells might reduce off-target risks. Moreover, owing to the natural extracellular recognition domain of the NKG2D receptor used in our NKz-CARs, these CARs are likely less immunogenic compared to those employing single-chain fragment variable domains. Encouragingly, clinical trials involving NKz-CAR T cells in cancer therapy have shown favorable safety profiles (Curio et al. 2021). Further evidence from study on nonhuman primates using T cells engineered with an NKG2D extracellular domain, CD8 transmembrane domain, and an additional CD137 co-stimulatory domain, instead of CD28, revealed no adverse effects (Yang et al. 2023). Further research is needed to optimize the efficacy and safety profiles of senolytic NKz-CAR T cells.

4.1.3 Astrocytes: a promising model for studying cellular senescence in brain aging and neurodegeneration

Astrocytes are the most predominant glial cells in the brain, which are central to the physiology of the nervous system, providing structural support and participating in various metabolic activities (García-Cáceres et al. 2019). Senescent astrocytes, characterized by elevated p16 expression and loss of lamin-B1, have been reported to accumulate in both aged human brains (Matias et al. 2022) and in those of AD patients (Gaikwad et al. 2021). Studies in p16-deficient mice have demonstrated attenuation of age-related decline in the self-renewal capacity of multipotent brain progenitors (Molofsky et al. 2006). Moreover, the genetic removal of p16-expressing senescent glial cells has been shown to mitigate cognitive decline, diminish tau hyperphosphorylation, and prevent gliosis in a tauopathy

mouse model (Bussian et al. 2018). These findings indicate glial senescence as a crucial pathomechanism potentially contributing to brain aging and neurodegenerative diseases. In addition, the proliferative capacity of astrocytes *in vivo* has been evidenced by studies analyzing human central nervous system biopsies and postmortem tissues (Colodner et al. 2005). In this thesis, mouse astrocytes subjected to DNA damage, oxidative stress, or proteasome inhibition exhibited classical signatures of CS, including morphological changes, decreased proliferation ability, elevated expression of negative cell cycle regulators, and enhanced SA-β-gal activity. Notably, astrocytes showed higher sensitivity to DNA damage and oxidative stress compared to MEFs, requiring lower doses and shorter exposure times to induce senescence. This heightened their responsiveness to external stimuli, which is consistent with previous research on human and rodent astrocyte cultures (Bitto et al. 2010, Souza et al. 2013), positioning astrocytes as an invaluable model for investigating CS within the broader context of brain research.

4.1.4 Expression of NKG2DLs and its contribution to immunogenicity in senescent cells

While p16 and p21 are recognized as hallmarks of senescence, their distinct functions in inhibiting cell proliferation have been evidenced in previous cell culture studies (Beauséjour et al. 2003, Kuilman et al. 2010). The p53/p21 pathway is generally activated early during senescence, primarily responding to dysfunctional telomeres as damaged DNA, whereas the p16/RB pathway appears more critical in sustaining the senescent state, independent of telomere status (Beauséjour et al. 2003). Recent *in vivo* single-cell transcriptomic analyses in mice have further demonstrated that cells with high p21 expression and those with high p16 expression form two distinct populations in various aged tissues (Wang et al. 2021). In the current thesis, exposure to DNA damage and oxidative stress in mouse astrocytes predominantly resulted in elevated p21/p53 expression without an increase in p16. In previous study on human astrocytes, where H2O2 treatment triggered extensive activation of p16, p53, and p21 (Bitto et al. 2010), and diverges from results in rat astrocytes under similar stress conditions (Bang et al. 2019), suggesting that the signatures of cell cycle regulators in astrocyte senescence vary across species and experimental conditions.

Compared to these varied expressions of classical senescence-associated cell cycle regulators, the upregulation of NKG2DLs may serve as a universal senescence marker. Elevated expression of NKG2DLs has been identified in numerous senescence models across human and mouse cells, driven by diverse stressors (Kim et al. 2008, Krizhanovsky et al. 2008, Sagiv et al. 2016, Soriani et al. 2009, Yang et al. 2023). Notably, elevated NKG2DLs expression was also observed *in vivo* in senescent dermal fibroblasts from elderly individuals (Hasegawa et al. 2023). In this thesis, a consistent increase in the protein levels of mouse NKG2DLs, including H60 and Mult1, was detected across different cell types and senescence-inducing stimuli, highlighting the potential role of NKG2DLs as a common feature of senescence, enhancing the immunogenicity of senescent cells in various contexts.

4.1.5 NKz-CAR T cells in senescence targeting: efficacy, antigen density and T cell subset dynamics

NKG2D-CAR T cells, which target NKG2DLs, have displayed anticancer effects in various tumor contexts, such as T-cell lymphoma (Driouk et al. 2020), glioblastoma (Weiss et al. 2018), osteosarcoma (Fernández et al. 2017), and colorectal cancer (Zarei et al. 2023). To evaluate the effectiveness of NKz-CAR in targeting senescent cells expressing NKG2DLs, we utilized a Calcein-AM-based cytotoxicity assay on the IncuCyte platform, allowing for real-time monitoring of cytotoxic responses throughout co-culture periods. This method provides a more dynamic and precise assessment of cytotoxic potency compared to previous endpoint assays (Hanson and Finkelstein 2019). Our results demonstrated that NKz-CAR T cells effectively eliminated senescent AST and MEFs triggered by either DNA damage or oxidative stress. Interestingly, CD137-fused NKG2D-CAR T cells targeting ETO-induced senescent MEFs achieved comparable cytotoxic effects at significantly lower E: T ratios (up to 2:1) in previous study (Yang et al. 2023), which may be due to the enhanced activation of NKG2D-CAR T cells with an additional co-stimulation.

Antigen density is another critical factor determining the cytotoxic activity of CAR-T cells (Gacerez et al. 2016). Nonetheless, our results did not show a correlation between NKG2DLs expression levels on the surface of target cells and the cytotoxicity of effector cells, which was revealed by the similar cytolytic capacities of NKz-CAR T cells against

senescent MEFs and AST with varying patterns of NKG2DLs expression. This finding aligns with observations in various tumor studies (Fernández et al. 2017, Ibáñez-Navarro et al. 2023, Zhang et al. 2005), indicating that diverse expression profiles of NKG2DLs in different cellular contexts do not necessarily influence the responsiveness of NKG2D-CAR T cells. The variability in binding affinities of NKG2D-CAR T cells to its ligands, as well as the different capacities of NKG2DLs to trigger downstream activating signals, may contribute to this observed lack of correlation (Zingoni et al. 2018).

Additionally, the dynamics within CAR-T cell subsets, particularly the proportions of CD8+ and CD4+ T cells, also impact their cytolytic activities (Zhang et al. 2020a). Although requiring longer conjunction periods and exhibiting delayed kinetics, CD4+ CAR-T cells display comparable cytotoxic efficiency compared to their CD8+ counterparts in targeting cancer cells (Agarwal et al. 2020, Liadi et al. 2015, Wang et al. 2018). They also show reduced susceptibility to exhaustion or activation-induced cell death (Liadi et al. 2019). Notably, experiments involving T cells expressing CD19-CAR from a defined 1:1 ratio of CD8:CD4 CAR-T cells have demonstrated superior antitumor activities *in vivo* (Sommermeyer et al. 2016, Turtle et al. 2016). In the current study, NKz-CAR T cells comprised approximately 62 % CD8+ T cells and a substantial proportion of CD4+ T cells (33.3 %). Given that most clinical and preclinical experiments employ randomly composed CD8+ and CD4+ CAR-T cell subsets (Zhang et al. 2020a), further investigation is needed to explore the optimal composition of CD8+ and CD4+ NKG2D-CAR T cells for targeting senescent cells, both *in vitro* and in aged individuals *in vivo*.

4.2 Analysis of the senescence-associated cell surfaceome reveals potential senotherapeutic targets

4.2.1 Summary of this study

Cell surface proteins serve as essential molecular mediators, facilitating vital functions like cell-cell communication and metabolite transport. Strikingly, 66 % of the drugs in the DrugBank database target cell surface proteins (Bausch-Fluck et al. 2018). The surfaceome is notably context-dependent, reflecting its diverse roles across different pathological states (Bausch-Fluck et al. 2018). Senescent cells, in contrast to the proliferative cells, exhibit unique metabolic profiles and protein expression patterns that contribute to their distinct phenotypes (Hernandez-Segura et al. 2018). Despite decades

of research, the molecular mechanisms driving CS are not fully understood. A pivotal aspect in understanding these mechanisms involves the CS surfaceome, which mediates interactions with the extracellular environment. Recent advancements in immunotherapeutic strategies, particularly those targeting the senescence-associated surfaceome, exemplified by the targeted senolytic strategy based on CAR-T cells described in our first study, demonstrate the potential of using senescent cell surface markers for targeted elimination of senescent cells from tissues (Amor et al. 2020, Qu et al. 2020, Yang et al. 2023). However, a comprehensive identification of surface proteins on the senescent cells is still lacking.

In our study, we utilized label-free quantitative MS analysis to characterize the senescence-associated cell surfaceome across various senescence models in both murine and human cells derived from fetal or adult tissues. Our findings revealed significant changes in the cell surface proteome during senescence, which varied markedly among cell types. Moreover, we identified four cell membrane proteins, including PLXNA1, PLXNA3, PTK7, and CYB5R1, as potential targets for senotherapy. These proteins were notably overrepresented in senescent cells, but minimally present or absent in normal tissues of both humans and mice. Additionally, these proteins, particularly PLXNA1, showed increased levels in various tissues of aged mice, as well as in the brains of an AD mouse model. These markers may hold substantial potential for advancing translational research into targeted senotherapy.

4.2.2 Biotinylation-based approach for the enrichment of cell surface associated proteins

The cell surfaceome, crucial for the immune system's antigen recognition, has been extensively explored for its potential to define disease biomarkers and therapeutic targets (Bausch-Fluck et al. 2018, Kuhlmann et al. 2018). However, challenges in cell surfaceome analysis arise from the difficulty of efficiently extracting cell surface proteins from their hydrophobic membrane into aqueous solutions, and their typically lower abundance compared to intracellular proteins consequently results in their underrepresentation in bottom-up proteomic studies (Pauwels et al. 2022). In this thesis, we utilized a biotinylation-based labeling method to enrich for extracellular and plasma membrane proteins. This method substantially enhances the quantification of cell surface proteins via

MS and has been employed to assess expression level variations under various experimental conditions (Nagano et al. 2011). We found that approximately 32 % of the proteins identified were classified as cell surface proteins across all cell conditions, which is consistent with prior studies and confirming the effectiveness of our methodology (Garcia et al. 2009, Jia et al. 2020). It is essential to acknowledge the possibility of detecting low-abundance intracellular proteins within our biotinylation samples, which may be due to nonspecific associations or direct interactions with cell surface proteins.

4.2.3 Extensive alterations in expression profiles and modifications in cell mechanics of the surfaceome during cellular senescence

In this thesis, we highlight significant alterations in the cell surfaceome under CS, demonstrated by marked differences in expression between senescent and non-senescent states. The observed changes in the surfaceome correspond with various cellular functional modifications.

Senescent cells exhibit altered adhesion properties, reflecting underlying changes in cytoskeletal organization, morphological transformation, and altered cell migration rates (Brauer et al. 2023, Levi et al. 2020). Our comprehensive analysis across varied senescence conditions revealed a substantial enrichment of cell adhesion molecules. This finding suggests that cell adhesion and migration are critical features of the CS surfaceome, playing essential roles in the structural remodeling of the extracellular matrix. Previous studies have reported a decrease in the expression of several cell adhesion molecules, such as melanoma cell adhesion molecule (MCAM) (Jin et al. 2016) and vascular cell adhesion protein 1 (VCAM1) (Jung et al. 2011), suggesting the impaired mechanical integrity of senescent cells compared to proliferative cells. We identified 93 cell surface proteins related to CS-driven cell adhesion changes through biological function GO annotation in this thesis. Intriguingly, a majority of these cell-adhesion molecules, including ICAM1, serpin family B member 8 (SERPINB8), Nexilin (NEXN), and Thy-1 membrane glycoprotein (THY1), exhibited upregulation across various senescence conditions in both species. ICAM1, notably associated with immune response modulation, has been demonstrated to be overexpressed in senescent human cells within atherosclerotic lesions (Gorgoulis et al. 2005) and in oxidative stress-induced senescent human omentum-derived mesothelial cells (Ksiazek et al. 2010). Its enhanced expression

in aged tissues (Miguel-Hidalgo et al. 2007) and tumors (Reina and Espel 2017) further underscores its potential as a biomarker for various aging-related alterations.

Additionally, our findings revealed a significant enrichment of the biological pathway “vesicle-mediated transport”, with 107 proteins identified, highlighting changes associated with the SASP. In this list, inflammatory factors such as pentraxin 3 (PTX3) and high mobility group box 1 (HMGB1), were also reported to be upregulated in recent senescence associated proteomic study (Basisty et al. 2020). Notably, these proteins are associated with the progression of age-related disorders, including cardiac conditions. bone diseases, and cancer, suggesting their potential as targets for senomorphic interventions (Lee et al. 2021, Palumbo et al. 2023, Peri et al. 2000, Tarantino et al. 2020).

4.2.4 Shared surfaceome contributes to a general senescence signature

Within the shared cell surface signature associated with CS identified in this thesis, proteins such as V-type proton ATPase subunit G 1 (ATP6V1G1) and lysosomal protein Lysosome-associated membrane glycoprotein 1 (LAMP1) were previously recognized in relation to senescence (Kang et al. 2017, Rovira et al. 2022). Furthermore, our analysis revealed novel markers that were upregulated during CS, including CYB5R1, amyloid beta precursor like protein 2 (APLP2), anoctamin-6 (ANO6), NPC intracellular cholesterol transporter 2 (NPC2), and transcriptional regulator QRICH1 (QRICH1). Notably, AGA, an enzyme plays a role in protein metabolism exhibiting peptidase and hydrolase activities (Harkke et al. 2003), was significantly and universally upregulated across various mouse senescence models, suggesting an increase in lysosomal activity during CS. For the downregulated proteins, glutathione S-transferase Mu 2 (GSTM2), an enzyme vital for the detoxification of ROS metabolites and xenobiotics, has demonstrated a decline during senescence in human primary fibroblasts, which could be mitigated by the transfection of small extracellular vesicles containing recombinant GSTM2 from healthy young donors (Fafián-Labora et al. 2020). The downregulation of GSTM2 across diverse senescence conditions in this thesis suggests a decreased capacity for oxidative stress resistance in senescent cells.

4.2.5 Cell type and senescence inducer substantively shape the heterogeneity of the senescence-associated surfaceome

The heterogeneity of CS is significantly influenced by the cell type and the specific inducers of senescence, as first evidenced by variable senolytic susceptibilities among senescent cells (Zhang et al. 2023, Zhu et al. 2015). This diversity is further reflected in distinct transcriptomic profiles (Casella et al. 2019, Hernandez-Segura et al. 2017) and SASPs (Basisty et al. 2020), which vary depending on the inducers, types of cells involved, and stages of senescence. In this thesis, our analysis of the CS surfaceome across various cell types under a unified stimulus has shown the significant role of cell type in defining the CS surfaceome at molecular and functional levels. PCA, Pearson correlation, and clustering analyses have consistently demonstrated that the heterogeneity of the CS surfaceome is predominantly shaped by the cell type. For example, senescent astrocytes were found to be enriched with glial cell migration pathway, marked by brain-specific proteins such as tyrosine phosphatase receptor type z1 (PTPRZ1). In contrast, proteins linked to muscle and skeletal system development, such as matrix metalloproteinase 2 (MMP2) and matrix gla protein (MGP), were prevalent in senescent fetal-derived fibroblasts. Senescent human endothelial cells subjected to oxidative stress displayed elevated proteins associated with blood vessel development, like bone morphogenetic protein 6 (BMP6) and angiopoietin 2 (ANGPT2). Interestingly, there was noticeable regulation of SASP-associated pathways, such as neutrophil degranulation and vesicle-mediated transport, across diverse senescence conditions. This heterogeneity in senescence surfaceome among different cell types may stem from intrinsic cellular responses to senescence-inducing stimuli and is further influenced by the interactions within their microenvironment, including neighboring cells and the extracellular matrix. *In vivo*, these contextual interactions potentially enhance the heterogeneity of the senescence surfaceome response to different stimuli.

Furthermore, senescent cells exhibit inducer-specific alterations in autophagy, proteasome activity, and metabolism (Capasso et al. 2015). In this thesis, CS surface profiles induced by DNA damage (ETO) showed abnormalities in glucose metabolism, while oxidative stress (H2O2) resulted in significant changes in cell signaling pathways. These distinct effects may be attributed to the specific cellular stress responses and DNA damage repair mechanisms activated during senescence, related to nuclear and

mitochondrial DNA damage. Moreover, the unique L-R interactome pattern observed in the EPO-specific CS surfaceome in mouse astrocytes, associated with chromosome missegregation, indicates the link between proteasome activity and genomic instability. Characterizing inducer-specific CS surface signatures may aid in distinguishing different forms of CS, as well as monitoring chemotherapy-induced CS *in vivo*. For example, ETO and EPO have been extensively used in cancer therapy (Adams 2004, Zhang et al. 2021a). The biomarkers identified in these inducer-specific senescence contexts could be poetically used to enhance therapeutic efficacy and minimize adverse effects while optimizing treatment regimens.

4.2.6 The potential applications of identified senescence surface markers as senotherapeutic targets

Ideal senotherapy targets should be distinctly and predominantly expressed on senescent cells while sparing normal tissues. In this thesis, some senescence surface markers, which are absent in the certain tissues, may be potentially used for the targeted elimination of senescent cells in specific organs. For instance, KIAA0319L (KIAA0319 Like) could be targeted for senescence clearance in the heart, lung, colon, and kidney, while THY1 could be specifically targeted in the heart.

Among the candidates we identified, four cell membrane proteins with low or undetectable expression in various normal tissues were noted. PLXNA3 is a member of the plexin family, which acts as an important receptor for semaphorin signaling and has shown elevated transcript levels in human senescent cell cultures (Brauer et al. 2023, Hernandez-Segura et al. 2017, Schwartz et al. 2021). Previous *in vivo* study demonstrated its role in neuronal development and axon guidance, with research indicating its association with neuronal apoptosis in PLXNA3 knockout mouse models (Ben-Zvi et al. 2008). Another potential senotherapeutic target identified from our research is PTK7, a member of the receptor tyrosine kinase family, which plays roles in cell migration and planar cell polarity. Enhanced levels of PTK7 have been documented in RS-associated human fibroblasts (Mrazkova et al. 2018), and it has been recognized as a SASP factor in senescent intestinal fibroblasts and aging intestines (Yun et al. 2023). All these four surface proteins are notably implicated in cancers. Particularly, PLXNA1, PLXNA3, and PTK7 have been reported to be associated with aggressive tumor phenotypes and poor prognosis in

several types of cancers (Jin et al. 2014, Woischke et al. 2016, Zhang et al. 2020b). Notably, therapeutic strategies utilizing PTK7, including CAR-T cells and ADCs, have revealed promising results in preclinical trials targeting solid tumors (Jie et al. 2021, Lee et al. 2023, Xu et al. 2023).

Moreover, the overlap between CS surface markers identified in the current thesis and known aging biomarkers suggests the implication of CS surfaceome in aging and various age-related diseases. The marked upregulation of these cell surface proteins, particularly PLXNA1, in tissues from aged mice and in the brains of AD model mice, highlights their potential as senotherapeutic targets aimed at addressing aging-related changes and disorders.

4.3 Conclusion

In the first study of this thesis, we evaluated the cytotoxic capabilities of NKG2D-CAR T cells targeting senescent MEFs and mouse astrocytes, induced by DNA damage and oxidative stress. Our research provides preliminary preclinical insights into the effectiveness of NKG2D-CAR T cells in targeting and eliminating stress-induced senescent cells *in vitro* (**Fig. 19**). Given that senescence is associated with various pathologies in aging and age-related diseases, our results indicate the extensive clinical potential of senolytic CAR-T cell therapies. Here, we provide the first evidence of the cytolytic activities of NKG2D-CAR T cells against senescent astrocytes, suggesting the feasibility of targeting senescent cells in the brain with this strategy. Further research is needed to fully explore the therapeutic potential of NKG2D-CAR T cells in the context of natural aging and *in vivo* models of age-related diseases.

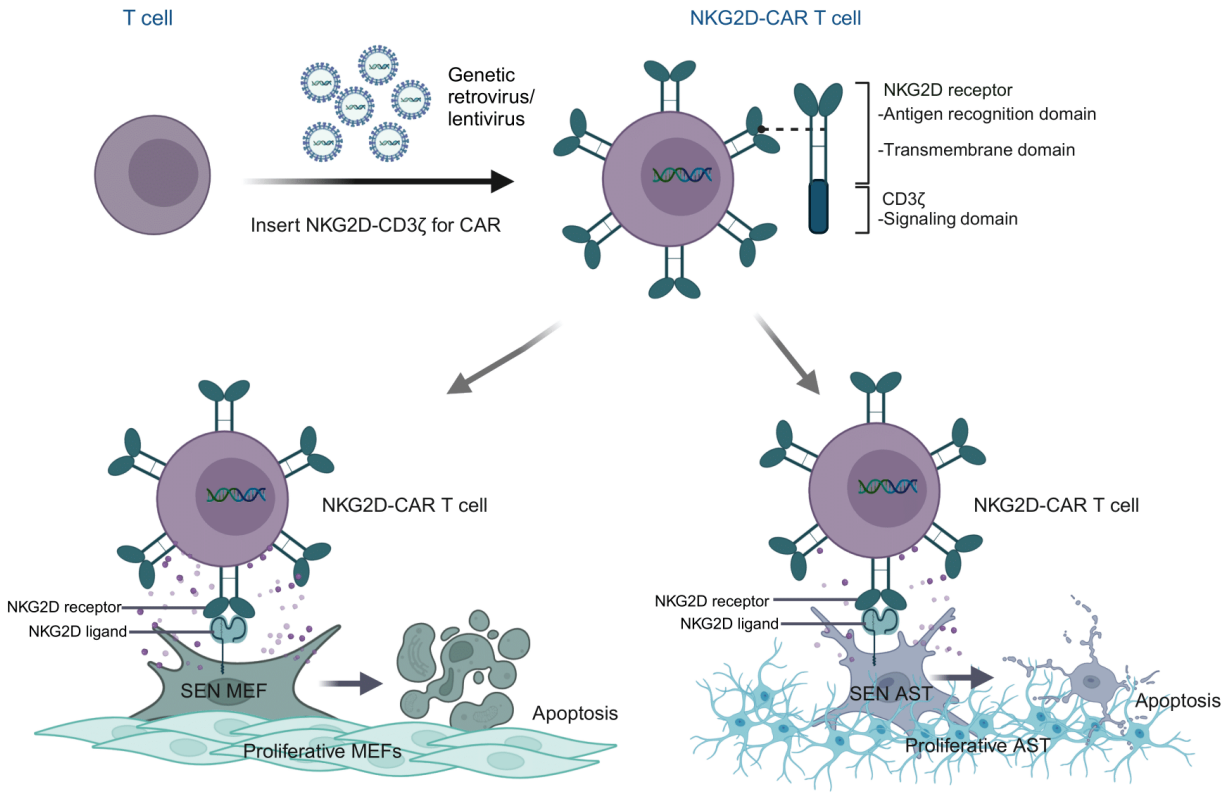

Fig. 19: Targeting senescent cells with NKG2D-CAR T cells. The NKG2D-CAR construct consists of an NKG2D receptor as the antigen recognition domain linked to a CD3ζ cytoplasmic signaling domain. T cells engineered to express NKG2D-CAR specifically identify and engage with NKG2DLs that are upregulated on the surface of senescent MEFs and AST induced by genotoxic and oxidative stress, exerting cytotoxic activity against the target cells. SEN, senescence. This figure was created with Biorender (biorender.com)

In the second study of this thesis, we comprehensively characterized the senescent cell-associated surfaceome using multiple senescence models triggered by various stimuli, spanning both murine and human cell types from fetal and adult origins (**Fig. 20**). Our analysis revealed significant alterations in cell surface protein expression and extensive changes in cell mechanics and ECM composition during senescence. The profound heterogeneity in the CS surfaceome, determined by cell type and the CS inducer, provides a critical basis for development of targeted immune-based therapies for senescent cell elimination. The potential utility of the senescence-associated cell surface markers identified in this thesis will be the focus of future research aimed at targeting and removing senescent cells in the context of aging and age-associated diseases.

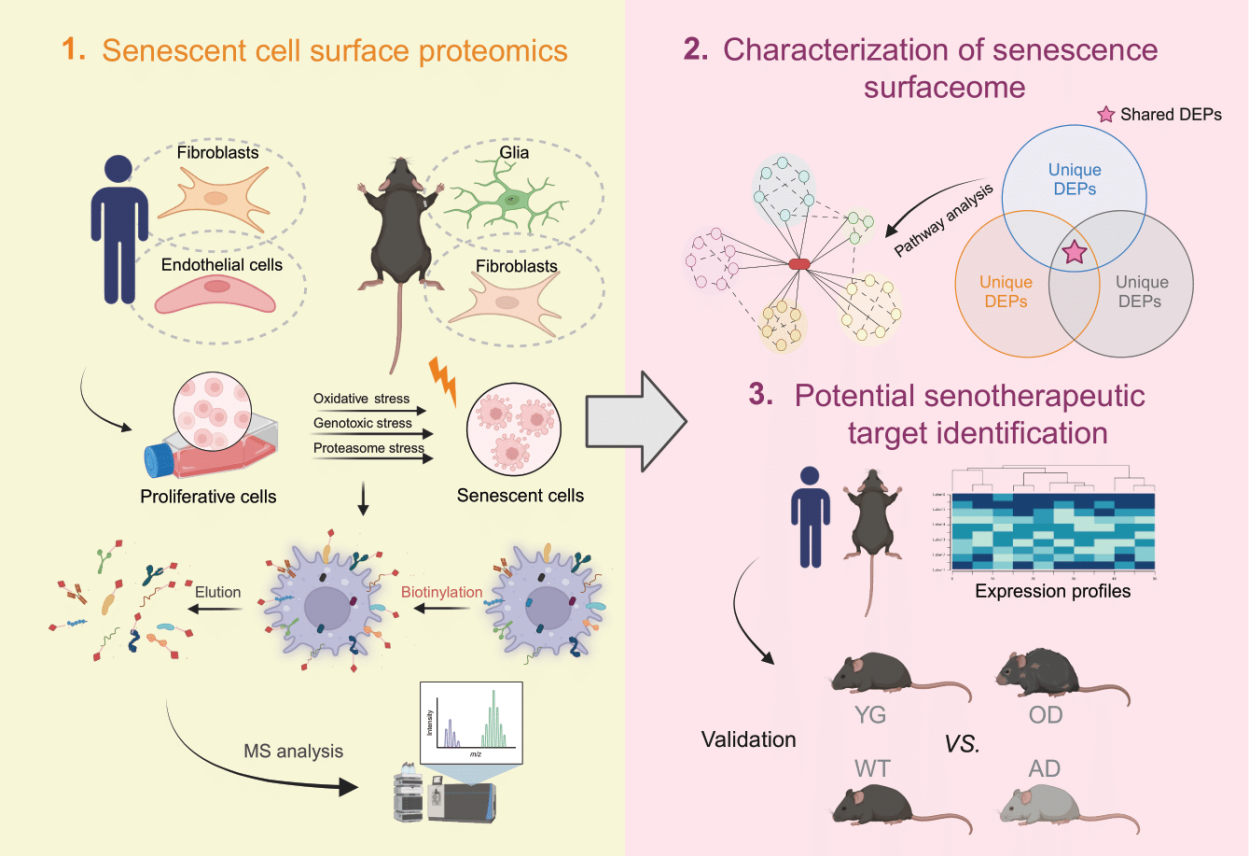

Fig. 20: Characterization of senescence-associated cell surfaceome. Senescence was induced in primary human endothelial cells, lung fibroblasts, mouse forebrain astrocytes, and mouse embryonic fibroblasts through genotoxic stress, oxidative stress, or proteasome stress. Following induction, cell surface proteins from all cell conditions were enriched using a biotinylation labeling technique, then subjected to mass spectrometric analysis. DEPs were identified and comprehensive bioinformatics and pathway analyses were conducted to characterize senescence-associated cell surfaceome. The identified potential senotherapeutic targets are highly expressed on the surface of senescent cells across various cell types and stress inducers, while present with low expression in normal tissues. The enrichments of these potential targets were further validated in various organs of aged WT mice and in the brains of an AD mouse model. This figure was created with Biorender (biorender.com).

5. Abstract

Cellular senescence is a state of permanent cell cycle arrest, characterized by substantial macromolecular alterations and senescence-associated secretory phenotype (SASP) in response to various stressors. The accumulation of senescent cells is thought to play a crucial role in aging-associated physiological decline and the pathogenesis of various age-related diseases. Clearance of senescent cells by transgenic or pharmaceutical strategies has been reported to attenuate various age-related pathologies and extend lifespan in mice. However, current senolytics still have limitations in terms of potency and specificity. Immunotherapy, particularly chimeric antigen receptor (CAR)-T cell therapy, emerges as a promising avenue to selectively eliminate senescent cells. Despite its potential, the effectiveness of this therapy hinges on the precise identification of senescence-associated surface antigens (senoantigens). Even though some surface markers for cellular senescence have been first identified in human fibroblasts, the translational potential of these findings is constrained by the limited senescent cell models previously established. The comprehensive identification of senescence-associated surface proteins remains to be achieved.

First, to investigate the efficacy of CAR-T cells in targeting and eliminating senescent cells *in vitro*, we focused on the Natural killer group 2D (NKG2D) receptor, which binds to NKG2D ligands (NKG2DLs) expressed on the surface of senescent cells, providing a target for CAR-T cells. Employing mouse embryonic fibroblasts (MEFs) and astrocytes (AST) as senescence models, we demonstrate the elevated expression of NKG2DLs in response to genotoxic and oxidative stress. NKG2D-CAR T cells displayed potent cytotoxicity against these senescent cells, with minimal effects on non-senescent cells, suggesting their potential as targeted senolytics. Our research presents the first evidence of NKG2D-CAR T cells' ability to target senescent brain cells, offering a novel approach to manage senescence-associated diseases. The findings pave the way for future investigations into the therapeutic applicability of NKG2D-targeting CAR-T cells in naturally aged organisms and models of aging-associated brain diseases *in vivo*.

Furthermore, to identify novel cell surface markers for potential senotherapeutic targeting, we conducted an extensive analysis of the cell surface proteome, or "surfaceome", in senescent cells, spanning various senescence induction regimes and encompassing both

murine and human cell types. Utilizing quantitative mass spectrometry, we investigated enriched cell surface proteins across eight distinct models of senescence. Our results uncover significant changes in surfaceome expression profiles during senescence, highlighting extensive modifications in cell mechanics and extracellular matrix remodeling. Our research also reveals substantive heterogeneity of senescence, predominantly influenced by cell type and senescence inducer. We identified four cell surface proteins with extracellular epitopes, namely PLXNA1, PLXNA3, PTK7, and CYB5R1. These proteins are expressed in senescent cells, absent or present at low levels in their proliferating counterparts, and notably upregulated in tissues from aged mice and an Alzheimer's disease mouse model. These proteins emerge as promising candidates for senotherapeutic targeting, offering potential pathways for identifying and selectively targeting senescent cell populations in aging and age-related diseases.

6. List of figures

7. List of tables

8. References

Adams J. The proteasome: a suitable antineoplastic target. Nat Rev Cancer 2004; 4: 349–360

Admasu TD, Rae M, Stolzing A. Dissecting primary and secondary senescence to enable new senotherapeutic strategies. Ageing Res Rev 2021; 70: 101412

Agarwal S, Hanauer JDS, Frank AM, Riechert V, Thalheimer FB, Buchholz CJ. In Vivo Generation of CAR T Cells Selectively in Human CD4+ Lymphocytes. Mol Ther 2020; 28: 1783–1794

Althubiti M, Lezina L, Carrera S, Jukes-Jones R, Giblett SM, Antonov A, Barlev N, Saldanha GS, Pritchard CA, Cain K, Macip S. Characterization of novel markers of senescence and their prognostic potential in cancer. Cell Death Dis 2014; 5: e1528

Amor C, Feucht J, Leibold J, Ho Y-J, Zhu C, Alonso-Curbelo D, Mansilla-Soto J, Boyer JA, Li X, Giavridis T, Kulick A, Houlihan S, Peerschke E, Friedman SL, Ponomarev V, Piersigilli A, Sadelain M, Lowe SW. Senolytic CAR T cells reverse senescence-associated pathologies. Nature 2020; 583: 127–132

Anderson KG, Stromnes IM, Greenberg PD. Obstacles Posed by the Tumor Microenvironment to T cell Activity: A Case for Synergistic Therapies. Cancer Cell 2017; 31: 311–325

Anderson R, Lagnado A, Maggiorani D, Walaszczyk A, Dookun E, Chapman J, Birch J, Salmonowicz H, Ogrodnik M, Jurk D, Proctor C, Correia-Melo C, Victorelli S, Fielder E, Berlinguer-Palmini R, Owens A, Greaves LC, Kolsky KL, Parini A, Douin-Echinard V, LeBrasseur NK, Arthur HM, Tual-Chalot S, Schafer MJ, Roos CM, Miller JD, Robertson N, Mann J, Adams PD, Tchkonia T, Kirkland JL, Mialet-Perez J, Richardson GD, Passos JF. Length-independent telomere damage drives post-mitotic cardiomyocyte senescence. EMBO J 2019; 38: e100492

Baker DJ, Wijshake T, Tchkonia T, LeBrasseur NK, Childs BG, van de Sluis B, Kirkland JL, van Deursen JM. Clearance of p16Ink4a-positive senescent cells delays ageing-associated disorders. Nature 2011; 479: 232–236

Baker DJ, Childs BG, Durik M, Wijers ME, Sieben CJ, Zhong J, Saltness RA, Jeganathan KB, Verzosa GC, Pezeshki A, Khazaie K, Miller JD, van Deursen JM. Naturally occurring p16(Ink4a)-positive cells shorten healthy lifespan. Nature 2016; 530: 184–189

Baker DJ, Arany Z, Baur JA, Epstein JA, June CH. CAR T therapy beyond cancer: the evolution of a living drug. Nature 2023; 619: 707–715

Bang M, Kim DG, Gonzales EL, Kwon KJ, Shin CY. Etoposide Induces Mitochondrial Dysfunction and Cellular Senescence in Primary Cultured Rat Astrocytes. Biomol Ther (Seoul) 2019; 27: 530–539

Barber A, Sentman CL. NKG2D receptor regulates human effector T-cell cytokine production. Blood 2011; 117: 6571–6581

Basisty N, Kale A, Jeon OH, Kuehnemann C, Payne T, Rao C, Holtz A, Shah S, Sharma V, Ferrucci L, Campisi J, Schilling B. A proteomic atlas of senescence-associated secretomes for aging biomarker development. PLoS Biol 2020; 18: e3000599

Bausch-Fluck D, Goldmann U, Müller S, van Oostrum M, Müller M, Schubert OT, Wollscheid B. The in silico human surfaceome. Proc Natl Acad Sci U S A 2018; 115: E10988–E10997

Beauséjour CM, Krtolica A, Galimi F, Narita M, Lowe SW, Yaswen P, Campisi J. Reversal of human cellular senescence: roles of the p53 and p16 pathways. EMBO J 2003; 22: 4212–4222

Ben-Zvi A, Manor O, Schachner M, Yaron A, Tessier-Lavigne M, Behar O. The Semaphorin receptor PlexinA3 mediates neuronal apoptosis during dorsal root ganglia development. J Neurosci 2008; 28: 12427–12432

Bitto A, Sell C, Crowe E, Lorenzini A, Malaguti M, Hrelia S, Torres C. Stress-induced senescence in human and rodent astrocytes. Exp Cell Res 2010; 316: 2961–2968

Brauer E, Lange T, Keller D, Görlitz S, Cho S, Keye J, Gossen M, Petersen A, Kornak U. Dissecting the influence of cellular senescence on cell mechanics and extracellular matrix formation in vitro. Aging Cell 2023; 22: e13744

Bussian TJ, Aziz A, Meyer CF, Swenson BL, van Deursen JM, Baker DJ. Clearance of senescent glial cells prevents tau-dependent pathology and cognitive decline. Nature 2018; 562: 578–582

Capasso S, Alessio N, Squillaro T, Di Bernardo G, Melone MA, Cipollaro M, Peluso G, Galderisi U. Changes in autophagy, proteasome activity and metabolism to determine a specific signature for acute and chronic senescent mesenchymal stromal cells. Oncotarget 2015; 6: 39457–39468

Carayannopoulos LN, Naidenko OV, Fremont DH, Yokoyama WM. Cutting edge: murine UL16-binding protein-like transcript 1: a newly described transcript encoding a high-affinity ligand for murine NKG2D. J Immunol 2002; 169: 4079–4083

Casella G, Munk R, Kim KM, Piao Y, De S, Abdelmohsen K, Gorospe M. Transcriptome signature of cellular senescence. Nucleic Acids Res 2019; 47: 7294–7305

Chaib S, Tchkonia T, Kirkland JL. Cellular senescence and senolytics: the path to the clinic. Nat Med 2022; 28: 1556–1568

Chen M, Lyu G, Han M, Nie H, Shen T, Chen W, Niu Y, Song Y, Li X, Li H, Chen X, Wang Z, Xia Z, Li W, Tian X-L, Ding C, Gu J, Zheng Y, Liu X, Hu J, Wei G, Tao W, Ni T. 3’ UTR

lengthening as a novel mechanism in regulating cellular senescence. Genome Res 2018; 28: 285–294

Chen W, Wang X, Wei G, Huang Y, Shi Y, Li D, Qiu S, Zhou B, Cao J, Chen M, Qin P, Jin W, Ni T. Single-Cell Transcriptome Analysis Reveals Six Subpopulations Reflecting Distinct Cellular Fates in Senescent Mouse Embryonic Fibroblasts. Front Genet 2020; 11: 867

Childs BG, Durik M, Baker DJ, van Deursen JM. Cellular senescence in aging and age-related disease: from mechanisms to therapy. Nat Med 2015; 21: 1424–1435

Cho SJ, Stout-Delgado HW. Aging and Lung Disease. Annu Rev Physiol 2020; 82: 433–459

Colodner KJ, Montana RA, Anthony DC, Folkerth RD, De Girolami U, Feany MB. Proliferative potential of human astrocytes. J Neuropathol Exp Neurol 2005; 64: 163–169
Coppé J-P, Desprez P-Y, Krtolica A, Campisi J. The senescence-associated secretory phenotype: the dark side of tumor suppression. Annu Rev Pathol 2010; 5: 99–118

Curio S, Jonsson G, Marinović S. A summary of current NKG2D-based CAR clinical trials. Immunother Adv 2021; 1: ltab018

Demaria M, Ohtani N, Youssef SA, Rodier F, Toussaint W, Mitchell JR, Laberge R-M, Vijg J, Van Steeg H, Dollé MET, Hoeijmakers JHJ, de Bruin A, Hara E, Campisi J. An essential role for senescent cells in optimal wound healing through secretion of PDGF-AA. Dev Cell 2014; 31: 722–733

Dimri GP, Lee X, Basile G, Acosta M, Scott G, Roskelley C, Medrano EE, Linskens M, Rubelj I, Pereira-Smith O. A biomarker that identifies senescent human cells in culture and in aging skin in vivo. Proc Natl Acad Sci U S A 1995; 92: 9363–9367

Doherty TJ. Invited review: Aging and sarcopenia. J Appl Physiol (1985) 2003; 95: 1717–1727

Driouk L, Gicobi JK, Kamihara Y, Rutherford K, Dranoff G, Ritz J, Baumeister SHC. Chimeric Antigen Receptor T Cells Targeting NKG2D-Ligands Show Robust Efficacy Against Acute Myeloid Leukemia and T-Cell Acute Lymphoblastic Leukemia. Front Immunol 2020; 11: 580328

Druelle C, Drullion C, Deslé J, Martin N, Saas L, Cormenier J, Malaquin N, Huot L, Slomianny C, Bouali F, Vercamer C, Hot D, Pourtier A, Chevet E, Abbadie C, Pluquet O. ATF6α regulates morphological changes associated with senescence in human fibroblasts. Oncotarget 2016; 7: 67699–67715

Fafián-Labora JA, Rodríguez-Navarro JA, O'Loghlen A. Small Extracellular Vesicles Have GST Activity and Ameliorate Senescence-Related Tissue Damage. Cell Metab 2020; 32: 71-86.e5

Falandry C, Bonnefoy M, Freyer G, Gilson E. Biology of cancer and aging: a complex association with cellular senescence. J Clin Oncol 2014; 32: 2604–2610

Fernández L, Metais J-Y, Escudero A, Vela M, Valentín J, Vallcorba I, Leivas A, Torres J, Valeri A, Patiño-García A, Martínez J, Leung W, Pérez-Martínez A. Memory T Cells Expressing an NKG2D-CAR Efficiently Target Osteosarcoma Cells. Clin Cancer Res 2017; 23: 5824–5835

Feucht J, Abou-El-Enein M. Senolytic CAR T Cells in Solid Tumors and Age-Related Pathologies. Mol Ther 2020; 28: 2108–2110

Gabai Y, Assouline B, Ben-Porath I. Senescent stromal cells: roles in the tumor microenvironment. Trends Cancer 2023; 9: 28–41

Gacerez AT, Arellano B, Sentman CL. How Chimeric Antigen Receptor Design Affects Adoptive T Cell Therapy. J Cell Physiol 2016; 231: 2590–2598

Gaikwad S, Puangmalai N, Bittar A, Montalbano M, Garcia S, McAllen S, Bhatt N, Sonawane M, Sengupta U, Kayed R. Tau oligomer induced HMGB1 release contributes to cellular senescence and neuropathology linked to Alzheimer's disease and frontotemporal dementia. Cell Rep 2021; 36: 109419

Garcia J, Faca V, Jarzembowski J, Zhang Q, Park J, Hanash S. Comprehensive profiling of the cell surface proteome of Sy5Y neuroblastoma cells yields a subset of proteins associated with tumor differentiation. J Proteome Res 2009; 8: 3791–3796

García-Cáceres C, Balland E, Prevot V, Luquet S, Woods SC, Koch M, Horvath TL, Yi C-X, Chowen JA, Verkhratsky A, Araque A, Bechmann I, Tschöp MH. Role of astrocytes, microglia, and tanycytes in brain control of systemic metabolism. Nat Neurosci 2019; 22: 7–14

Gasek NS, Kuchel GA, Kirkland JL, Xu M. Strategies for Targeting Senescent Cells in Human Disease. Nat Aging 2021; 1: 870–879

Geiger T, Velic A, Macek B, Lundberg E, Kampf C, Nagaraj N, Uhlen M, Cox J, Mann M. Initial quantitative proteomic map of 28 mouse tissues using the SILAC mouse. Mol Cell Proteomics 2013; 12: 1709–1722

Georgakopoulou EA, Tsimaratou K, Evangelou K, Fernandez Marcos PJ, Zoumpourlis V, Trougakos IP, Kletsas D, Bartek J, Serrano M, Gorgoulis VG. Specific lipofuscin staining as a novel biomarker to detect replicative and stress-induced senescence. A method applicable in cryo-preserved and archival tissues. Aging (Albany NY) 2013; 5: 37–50

González S, López-Soto A, Suarez-Alvarez B, López-Vázquez A, López-Larrea C. NKG2D ligands: key targets of the immune response. Trends Immunol 2008; 29: 397–403

González-Gualda E, Baker AG, Fruk L, Muñoz-Espín D. A guide to assessing cellular senescence in vitro and in vivo. FEBS J 2021; 288: 56–80

Gorgoulis VG, Pratsinis H, Zacharatos P, Demoliou C, Sigala F, Asimacopoulos PJ, Papavassiliou AG, Kletsas D. p53-dependent ICAM-1 overexpression in senescent human cells identified in atherosclerotic lesions. Lab Invest 2005; 85: 502–511

Groh V, Bahram S, Bauer S, Herman A, Beauchamp M, Spies T. Cell stress-regulated human major histocompatibility complex class I gene expressed in gastrointestinal epithelium. Proc Natl Acad Sci U S A 1996; 93: 12445–12450

Guo J, Huang X, Dou L, Yan M, Shen T, Tang W, Li J. Aging and aging-related diseases: from molecular mechanisms to interventions and treatments. Signal Transduct Target Ther 2022; 7: 391

Hanson KM, Finkelstein JN. An accessible and high-throughput strategy of continuously monitoring apoptosis by fluorescent detection of caspase activation. Anal Biochem 2019; 564–565: 96–101

Harkke S, Laine M, Jalanko A. Aspartylglucosaminidase (AGA) is efficiently produced and endocytosed by glial cells: implication for the therapy of a lysosomal storage disorder. J Gene Med 2003; 5: 472–482

Hasegawa T, Oka T, Son HG, Oliver-García VS, Azin M, Eisenhaure TM, Lieb DJ, Hacohen N, Demehri S. Cytotoxic CD4+ T cells eliminate senescent cells by targeting cytomegalovirus antigen. Cell 2023; 186: 1417-1431.e20

Hayflick L, Moorhead PS. The serial cultivation of human diploid cell strains. Exp Cell Res 1961; 25: 585–621

He S, Sharpless NE. Senescence in Health and Disease. Cell 2017; 169: 1000–1011

Herbig U, Ferreira M, Condel L, Carey D, Sedivy JM. Cellular senescence in aging primates. Science 2006; 311: 1257

Hernandez-Segura A, de Jong TV, Melov S, Guryev V, Campisi J, Demaria M. Unmasking Transcriptional Heterogeneity in Senescent Cells. Curr Biol 2017; 27: 2652-2660.e4

Hernandez-Segura A, Nehme J, Demaria M. Hallmarks of Cellular Senescence. Trends Cell Biol 2018; 28: 436–453

Hou Y, Dan X, Babbar M, Wei Y, Hasselbalch SG, Croteau DL, Bohr VA. Ageing as a risk factor for neurodegenerative disease. Nat Rev Neurol 2019; 15: 565–581

Ibáñez-Navarro M, Fernández A, Escudero A, Esteso G, Campos-Silva C, Navarro-Aguadero MÁ, Leivas A, Caracuel BR, Rodríguez-Antolín C, Ortiz A, Navarro-Zapata A, Mestre-Durán C, Izquierdo M, Balaguer-Pérez M, Ferreras C, Martínez-López J, Valés-Gómez M, Pérez-Martínez A, Fernández L. NKG2D-CAR memory T cells target pediatric T-cell acute lymphoblastic leukemia in vitro and in vivo but fail to eliminate leukemia initiating cells. Front Immunol 2023; 14: 1187665

Jain K, Verma PJ, Liu J. Isolation and handling of mouse embryonic fibroblasts. Methods Mol Biol 2014; 1194: 247–252

Jakob F, Seefried L, Schwab M. [Age and osteoporosis. Effects of aging on osteoporosis, the diagnostics and therapy]. Internist (Berl) 2014; 55: 755–761

Jeon OH, Kim C, Laberge R-M, Demaria M, Rathod S, Vasserot AP, Chung JW, Kim DH, Poon Y, David N, Baker DJ, van Deursen JM, Campisi J, Elisseeff JH. Local clearance of senescent cells attenuates the development of post-traumatic osteoarthritis and creates a pro-regenerative environment. Nat Med 2017; 23: 775–781

Jeyapalan JC, Ferreira M, Sedivy JM, Herbig U. Accumulation of senescent cells in mitotic tissue of aging primates. Mech Ageing Dev 2007; 128: 36–44

Jia L-J, Krüger T, Blango MG, von Eggeling F, Kniemeyer O, Brakhage AA. Biotinylated Surfome Profiling Identifies Potential Biomarkers for Diagnosis and Therapy of Aspergillus fumigatus Infection. mSphere 2020; 5: e00535-20

Jie Y, Liu G, Feng L, Li Y, E M, Wu L, Li Y, Rong G, Li Y, Wei H, Gu A. PTK7-Targeting CAR T-Cells for the Treatment of Lung Cancer and Other Malignancies. Front Immunol 2021; 12: 665970

Jin HJ, Kwon JH, Kim M, Bae YK, Choi SJ, Oh W, Yang YS, Jeon HB. Downregulation of Melanoma Cell Adhesion Molecule (MCAM/CD146) Accelerates Cellular Senescence in Human Umbilical Cord Blood-Derived Mesenchymal Stem Cells. Stem Cells Transl Med 2016; 5: 427–439

Jin J, Ryu HS, Lee KB, Jang J-J. High expression of protein tyrosine kinase 7 significantly associates with invasiveness and poor prognosis in intrahepatic cholangiocarcinoma. PLoS One 2014; 9: e90247

Jung EM, Kwon O, Kwon K-S, Cho YS, Rhee SK, Min J-K, Oh D-B. Evidences for correlation between the reduced VCAM-1 expression and hyaluronan synthesis during cellular senescence of human mesenchymal stem cells. Biochem Biophys Res Commun 2011; 404: 463–469

Justice JN, Nambiar AM, Tchkonia T, LeBrasseur NK, Pascual R, Hashmi SK, Prata L, Masternak MM, Kritchevsky SB, Musi N, Kirkland JL. Senolytics in idiopathic pulmonary fibrosis: Results from a first-in-human, open-label, pilot study. EBioMedicine 2019; 40: 554–563

Kang HT, Park JT, Choi K, Kim Y, Choi HJC, Jung CW, Lee Y-S, Park SC. Chemical screening identifies ATM as a target for alleviating senescence. Nat Chem Biol 2017; 13: 616–623

Kim KM, Noh JH, Bodogai M, Martindale JL, Yang X, Indig FE, Basu SK, Ohnuma K, Morimoto C, Johnson PF, Biragyn A, Abdelmohsen K, Gorospe M. Identification of senescent cell surface targetable protein DPP4. Genes Dev 2017; 31: 1529–1534

Kim KM, Noh JH, Bodogai M, Martindale JL, Pandey PR, Yang X, Biragyn A, Abdelmohsen K, Gorospe M. SCAMP4 enhances the senescent cell secretome. Genes Dev 2018; 32: 909–914

Kim M-S, Pinto SM, Getnet D, Nirujogi RS, Manda SS, Chaerkady R, Madugundu AK, Kelkar DS, Isserlin R, Jain S, Thomas JK, Muthusamy B, Leal-Rojas P, Kumar P, Sahasrabuddhe NA, Balakrishnan L, Advani J, George B, Renuse S, Selvan LDN, Patil AH, Nanjappa V, Radhakrishnan A, Prasad S, Subbannayya T, Raju R, Kumar M, Sreenivasamurthy SK, Marimuthu A, Sathe GJ, Chavan S, Datta KK, Subbannayya Y, Sahu A, Yelamanchi SD, Jayaram S, Rajagopalan P, Sharma J, Murthy KR, Syed N, Goel R, Khan AA, Ahmad S, Dey G, Mudgal K, Chatterjee A, Huang T-C, Zhong J, Wu X, Shaw PG, Freed D, Zahari MS, Mukherjee KK, Shankar S, Mahadevan A, Lam H, Mitchell CJ, Shankar SK, Satishchandra P, Schroeder JT, Sirdeshmukh R, Maitra A, Leach SD, Drake CG, Halushka MK, Prasad TSK, Hruban RH, Kerr CL, Bader GD, Iacobuzio-Donahue CA, Gowda H, Pandey A. A draft map of the human proteome. Nature 2014; 509: 575–581

Kim TW, Kim HJ, Lee C, Kim HY, Baek S-H, Kim JH, Kwon K-S, Kim J-R. Identification of replicative senescence-associated genes in human umbilical vein endothelial cells by an annealing control primer system. Exp Gerontol 2008; 43: 286–295

Kim Y, Born C, Bléry M, Steinle A. MICAgen Mice Recapitulate the Highly Restricted but Activation-Inducible Expression of the Paradigmatic Human NKG2D Ligand MICA. Front Immunol 2020; 11: 960

Kirkland JL, Tchkonia T. Cellular Senescence: A Translational Perspective. EBioMedicine 2017; 21: 21–28

Kritsilis M, V Rizou S, Koutsoudaki PN, Evangelou K, Gorgoulis VG, Papadopoulos D. Ageing, Cellular Senescence and Neurodegenerative Disease. Int J Mol Sci 2018; 19: 2937

Krizhanovsky V, Yon M, Dickins RA, Hearn S, Simon J, Miething C, Yee H, Zender L, Lowe SW. Senescence of activated stellate cells limits liver fibrosis. Cell 2008; 134: 657–667

Ksiazek K, Mikuła-Pietrasik J, Catar R, Dworacki G, Winckiewicz M, Frydrychowicz M, Dragun D, Staniszewski R, Jörres A, Witowski J. Oxidative stress-dependent increase in ICAM-1 expression promotes adhesion of colorectal and pancreatic cancers to the senescent peritoneal mesothelium. Int J Cancer 2010; 127: 293–303

Kuhlmann L, Cummins E, Samudio I, Kislinger T. Cell-surface proteomics for the identification of novel therapeutic targets in cancer. Expert Rev Proteomics 2018; 15: 259–275

Kuilman T, Michaloglou C, Mooi WJ, Peeper DS. The essence of senescence. Genes Dev 2010; 24: 2463–2479

Lee BY, Han JA, Im JS, Morrone A, Johung K, Goodwin EC, Kleijer WJ, DiMaio D, Hwang ES. Senescence-associated beta-galactosidase is lysosomal beta-galactosidase. Aging Cell 2006; 5: 187–195

Lee J-J, Park IH, Kwak MS, Rhee WJ, Kim SH, Shin J-S. HMGB1 orchestrates STING-mediated senescence via TRIM30α modulation in cancer cells. Cell Death Discov 2021; 7: 28

Lee JY, Jonus HC, Sadanand A, Branella GM, Maximov V, Suttapitugsakul S, Schniederjan MJ, Shim J, Ho A, Parwani KK, Fedanov A, Pilgrim AA, Silva JA, Schnepp RW, Doering CB, Wu R, Spencer HT, Goldsmith KC. Identification and targeting of protein

tyrosine kinase 7 (PTK7) as an immunotherapy candidate for neuroblastoma. Cell Rep Med 2023; 4: 101091

Levi N, Papismadov N, Solomonov I, Sagi I, Krizhanovsky V. The ECM path of senescence in aging: components and modifiers. FEBS J 2020; 287: 2636–2646

Liadi I, Singh H, Romain G, Rey-Villamizar N, Merouane A, Adolacion JRT, Kebriaei P, Huls H, Qiu P, Roysam B, Cooper LJN, Varadarajan N. Individual Motile CD4(+) T Cells Can Participate in Efficient Multikilling through Conjugation to Multiple Tumor Cells. Cancer Immunol Res 2015; 3: 473–482

Liadi I, Singh H, Romain G, Roysam B, Cooper LJ, Varadarajan N. Defining potency of CAR+ T cells: Fast and furious or slow and steady. Oncoimmunology 2019; 8: e1051298
Longo M, Bellastella G, Maiorino MI, Meier JJ, Esposito K, Giugliano D. Diabetes and Aging: From Treatment Goals to Pharmacologic Therapy. Front Endocrinol (Lausanne) 2019; 10: 45

López-Otín C, Blasco MA, Partridge L, Serrano M, Kroemer G. Hallmarks of aging: An expanding universe. Cell 2023; 186: 243–278

de Magalhães JP, Curado J, Church GM. Meta-analysis of age-related gene expression profiles identifies common signatures of aging. Bioinformatics 2009; 25: 875–881

Matias I, Diniz LP, Damico IV, Araujo APB, Neves L da S, Vargas G, Leite REP, Suemoto CK, Nitrini R, Jacob-Filho W, Grinberg LT, Hol EM, Middeldorp J, Gomes FCA. Loss of lamin-B1 and defective nuclear morphology are hallmarks of astrocyte senescence in vitro and in the aging human hippocampus. Aging Cell 2022; 21: e13521

Mc Auley MT, Guimera AM, Hodgson D, Mcdonald N, Mooney KM, Morgan AE, Proctor CJ. Modelling the molecular mechanisms of aging. Biosci Rep 2017; 37: BSR20160177

McCormick R, Vasilaki A. Age-related changes in skeletal muscle: changes to life-style as a therapy. Biogerontology 2018; 19: 519–536

Merkin J, Russell C, Chen P, Burge CB. Evolutionary dynamics of gene and isoform regulation in Mammalian tissues. Science 2012; 338: 1593–1599

Miguel-Hidalgo JJ, Nithuairisg S, Stockmeier C, Rajkowska G. Distribution of ICAM-1 immunoreactivity during aging in the human orbitofrontal cortex. Brain Behav Immun 2007; 21: 100–111

Mijit M, Caracciolo V, Melillo A, Amicarelli F, Giordano A. Role of p53 in the Regulation of Cellular Senescence. Biomolecules 2020; 10: 420

Mohamad Kamal NS, Safuan S, Shamsuddin S, Foroozandeh P. Aging of the cells: Insight into cellular senescence and detection Methods. Eur J Cell Biol 2020; 99: 151108

Molofsky AV, Slutsky SG, Joseph NM, He S, Pardal R, Krishnamurthy J, Sharpless NE, Morrison SJ. Increasing p16INK4a expression decreases forebrain progenitors and neurogenesis during ageing. Nature 2006; 443: 448–452

Mrazkova B, Dzijak R, Imrichova T, Kyjacova L, Barath P, Dzubak P, Holub D, Hajduch M, Nahacka Z, Andera L, Holicek P, Vasicova P, Sapega O, Bartek J, Hodny Z. Induction, regulation and roles of neural adhesion molecule L1CAM in cellular senescence. Aging (Albany NY) 2018; 10: 434–462

Muñoz-Espín D, Serrano M. Cellular senescence: from physiology to pathology. Nat Rev Mol Cell Biol 2014; 15: 482–496

Muñoz-Espín D, Cañamero M, Maraver A, Gómez-López G, Contreras J, Murillo-Cuesta S, Rodríguez-Baeza A, Varela-Nieto I, Ruberte J, Collado M, Serrano M. Programmed cell senescence during mammalian embryonic development. Cell 2013; 155: 1104–1118

Nagano K, Shinkawa T, Kato K, Inomata N, Yabuki N, Haramura M. Distinct cell surface proteome profiling by biotin labeling and glycoprotein capturing. J Proteomics 2011; 74: 1985–1993

Niccoli T, Partridge L. Ageing as a risk factor for disease. Curr Biol 2012; 22: R741-752
North BJ, Sinclair DA. The intersection between aging and cardiovascular disease. Circ Res 2012; 110: 1097–1108

O'Sullivan ED, Hughes J, Ferenbach DA. Renal Aging: Causes and Consequences. J Am Soc Nephrol 2017; 28: 407–420

Ovadya Y, Landsberger T, Leins H, Vadai E, Gal H, Biran A, Yosef R, Sagiv A, Agrawal A, Shapira A, Windheim J, Tsoory M, Schirmbeck R, Amit I, Geiger H, Krizhanovsky V. Impaired immune surveillance accelerates accumulation of senescent cells and aging. Nat Commun 2018; 9: 5435

Palumbo A, Atzeni F, Murdaca G, Gangemi S. The Role of Alarmins in Osteoarthritis Pathogenesis: HMGB1, S100B and IL-33. Int J Mol Sci 2023; 24: 12143

Pauwels J, Fijałkowska D, Eyckerman S, Gevaert K. Mass spectrometry and the cellular surfaceome. Mass Spectrom Rev 2022; 41: 804–841

Pellegatta S, Savoldo B, Di Ianni N, Corbetta C, Chen Y, Patané M, Sun C, Pollo B, Ferrone S, DiMeco F, Finocchiaro G, Dotti G. Constitutive and TNFα-inducible expression of chondroitin sulfate proteoglycan 4 in glioblastoma and neurospheres: Implications for CAR-T cell therapy. Sci Transl Med 2018; 10: eaao2731

Peri G, Introna M, Corradi D, Iacuitti G, Signorini S, Avanzini F, Pizzetti F, Maggioni AP, Moccetti T, Metra M, Cas LD, Ghezzi P, Sipe JD, Re G, Olivetti G, Mantovani A, Latini R. PTX3, A prototypical long pentraxin, is an early indicator of acute myocardial infarction in humans. Circulation 2000; 102: 636–641

Poblocka M, Bassey AL, Smith VM, Falcicchio M, Manso AS, Althubiti M, Sheng X, Kyle A, Barber R, Frigerio M, Macip S. Targeted clearance of senescent cells using an antibody-drug conjugate against a specific membrane marker. Sci Rep 2021; 11: 20358

Prajapati K, Perez C, Rojas LBP, Burke B, Guevara-Patino JA. Functions of NKG2D in CD8+ T cells: an opportunity for immunotherapy. Cell Mol Immunol 2018; 15: 470–479

Purvis JE, Karhohs KW, Mock C, Batchelor E, Loewer A, Lahav G. p53 dynamics control cell fate. Science 2012; 336: 1440–1444

Qu A, Wu X, Li S, Sun M, Xu L, Kuang H, Xu C. An NIR-Responsive DNA-Mediated Nanotetrahedron Enhances the Clearance of Senescent Cells. Adv Mater 2020; 32: e2000184

Raulet DH. Roles of the NKG2D immunoreceptor and its ligands. Nat Rev Immunol 2003; 3: 781–790

Reina M, Espel E. Role of LFA-1 and ICAM-1 in Cancer. Cancers (Basel) 2017; 9: 153

Rodier F, Muñoz DP, Teachenor R, Chu V, Le O, Bhaumik D, Coppé J-P, Campeau E, Beauséjour CM, Kim S-H, Davalos AR, Campisi J. DNA-SCARS: distinct nuclear structures that sustain damage-induced senescence growth arrest and inflammatory cytokine secretion. J Cell Sci 2011; 124: 68–81

Roos CM, Zhang B, Palmer AK, Ogrodnik MB, Pirtskhalava T, Thalji NM, Hagler M, Jurk D, Smith LA, Casaclang-Verzosa G, Zhu Y, Schafer MJ, Tchkonia T, Kirkland JL, Miller JD. Chronic senolytic treatment alleviates established vasomotor dysfunction in aged or atherosclerotic mice. Aging Cell 2016; 15: 973–977

Rovira M, Sereda R, Pladevall-Morera D, Ramponi V, Marin I, Maus M, Madrigal-Matute J, Díaz A, García F, Muñoz J, Cuervo AM, Serrano M. The lysosomal proteome of senescent cells contributes to the senescence secretome. Aging Cell 2022; 21: e13707

Sagiv A, Krizhanovsky V. Immunosurveillance of senescent cells: the bright side of the senescence program. Biogerontology 2013; 14: 617–628

Sagiv A, Burton DGA, Moshayev Z, Vadai E, Wensveen F, Ben-Dor S, Golani O, Polic B, Krizhanovsky V. NKG2D ligands mediate immunosurveillance of senescent cells. Aging (Albany NY) 2016; 8: 328–344

Sah E, Krishnamurthy S, Ahmidouch MY, Gillispie GJ, Milligan C, Orr ME. The Cellular Senescence Stress Response in Post-Mitotic Brain Cells: Cell Survival at the Expense of Tissue Degeneration. Life (Basel) 2021; 11: 229

Schafer MJ, White TA, Iijima K, Haak AJ, Ligresti G, Atkinson EJ, Oberg AL, Birch J, Salmonowicz H, Zhu Y, Mazula DL, Brooks RW, Fuhrmann-Stroissnigg H, Pirtskhalava T, Prakash YS, Tchkonia T, Robbins PD, Aubry MC, Passos JF, Kirkland JL, Tschumperlin DJ, Kita H, LeBrasseur NK. Cellular senescence mediates fibrotic pulmonary disease. Nat Commun 2017; 8: 14532

Schildge S, Bohrer C, Beck K, Schachtrup C. Isolation and culture of mouse cortical astrocytes. J Vis Exp 2013;50079

Schwartz RE, Shokhirev MN, Andrade LR, Gutkind JS, Iglesias-Bartolome R, Shadel GS. Insights into epithelial cell senescence from transcriptome and secretome analysis of human oral keratinocytes. Aging (Albany NY) 2021; 13: 4747–4777

Scifo E, Szwajda A, Soliymani R, Pezzini F, Bianchi M, Dapkunas A, Dębski J, Uusi-Rauva K, Dadlez M, Gingras A-C, Tyynelä J, Simonati A, Jalanko A, Baumann MH, Lalowski M. Proteomic analysis of the palmitoyl protein thioesterase 1 interactome in SH-SY5Y human neuroblastoma cells. J Proteomics 2015; 123: 42–53

Sherr CJ, Beach D, Shapiro GI. Targeting CDK4 and CDK6: From Discovery to Therapy. Cancer Discov 2016; 6: 353–367

Shin JH, Zhang L, Murillo-Sauca O, Kim J, Kohrt HEK, Bui JD, Sunwoo JB. Modulation of natural killer cell antitumor activity by the aryl hydrocarbon receptor. Proc Natl Acad Sci U S A 2013; 110: 12391–12396

Sommermeyer D, Hudecek M, Kosasih PL, Gogishvili T, Maloney DG, Turtle CJ, Riddell SR. Chimeric antigen receptor-modified T cells derived from defined CD8+ and CD4+ subsets confer superior antitumor reactivity in vivo. Leukemia 2016; 30: 492–500

Song P, An J, Zou M-H. Immune Clearance of Senescent Cells to Combat Ageing and Chronic Diseases. Cells 2020; 9: 671

Soriani A, Zingoni A, Cerboni C, Iannitto ML, Ricciardi MR, Di Gialleonardo V, Cippitelli M, Fionda C, Petrucci MT, Guarini A, Foà R, Santoni A. ATM-ATR-dependent up-regulation of DNAM-1 and NKG2D ligands on multiple myeloma cells by therapeutic agents results in enhanced NK-cell susceptibility and is associated with a senescent phenotype. Blood 2009; 113: 3503–3511

Souza DG, Bellaver B, Souza DO, Quincozes-Santos A. Characterization of adult rat astrocyte cultures. PLoS One 2013; 8: e60282

Storer M, Mas A, Robert-Moreno A, Pecoraro M, Ortells MC, Di Giacomo V, Yosef R, Pilpel N, Krizhanovsky V, Sharpe J, Keyes WM. Senescence is a developmental mechanism that contributes to embryonic growth and patterning. Cell 2013; 155: 1119–1130

Suda M, Shimizu I, Katsuumi G, Yoshida Y, Hayashi Y, Ikegami R, Matsumoto N, Yoshida Y, Mikawa R, Katayama A, Wada J, Seki M, Suzuki Y, Iwama A, Nakagami H, Nagasawa A, Morishita R, Sugimoto M, Okuda S, Tsuchida M, Ozaki K, Nakanishi-Matsui M, Minamino T. Senolytic vaccination improves normal and pathological age-related phenotypes and increases lifespan in progeroid mice. Nat Aging 2021; 1: 1117–1126

Tanaka T, Biancotto A, Moaddel R, Moore AZ, Gonzalez-Freire M, Aon MA, Candia J, Zhang P, Cheung F, Fantoni G, CHI consortium, Semba RD, Ferrucci L. Plasma proteomic signature of age in healthy humans. Aging Cell 2018; 17: e12799

Tang H, Geng A, Zhang T, Wang C, Jiang Y, Mao Z. Single senescent cell sequencing reveals heterogeneity in senescent cells induced by telomere erosion. Protein Cell 2019; 10: 370–375

Tarantino U, Greggi C, Cariati I, Visconti VV, Gasparini M, Cateni M, Gasbarra E, Botta A, Salustri A, Scimeca M. The Role of PTX3 in Mineralization Processes and Aging-Related Bone Diseases. Front Immunol 2020; 11: 622772

Tchkonia T, Zhu Y, van Deursen J, Campisi J, Kirkland JL. Cellular senescence and the senescent secretory phenotype: therapeutic opportunities. J Clin Invest 2013; 123: 966–972

Titorenko VI. Aging and Age-related Disorders: From Molecular Mechanisms to Therapies. Int J Mol Sci 2019; 20: 3280

Triposkiadis F, Xanthopoulos A, Butler J. Cardiovascular Aging and Heart Failure: JACC Review Topic of the Week. J Am Coll Cardiol 2019; 74: 804–813

Turtle CJ, Hanafi L-A, Berger C, Gooley TA, Cherian S, Hudecek M, Sommermeyer D, Melville K, Pender B, Budiarto TM, Robinson E, Steevens NN, Chaney C, Soma L, Chen X, Yeung C, Wood B, Li D, Cao J, Heimfeld S, Jensen MC, Riddell SR, Maloney DG. CD19 CAR-T cells of defined CD4+:CD8+ composition in adult B cell ALL patients. J Clin Invest 2016; 126: 2123–2138

Tuttle CSL, Waaijer MEC, Slee-Valentijn MS, Stijnen T, Westendorp R, Maier AB. Cellular senescence and chronological age in various human tissues: A systematic review and meta-analysis. Aging Cell 2020; 19: e13083

Tyrrell DJ, Goldstein DR. Ageing and atherosclerosis: vascular intrinsic and extrinsic factors and potential role of IL-6. Nat Rev Cardiol 2021; 18: 58–68

VanSeggelen H, Hammill JA, Dvorkin-Gheva A, Tantalo DGM, Kwiecien JM, Denisova GF, Rabinovich B, Wan Y, Bramson JL. T Cells Engineered With Chimeric Antigen Receptors Targeting NKG2D Ligands Display Lethal Toxicity in Mice. Mol Ther 2015; 23: 1600–1610

Wang B, Wang L, Gasek NS, Zhou Y, Kim T, Guo C, Jellison ER, Haynes L, Yadav S, Tchkonia T, Kuchel GA, Kirkland JL, Xu M. An inducible p21-Cre mouse model to monitor and manipulate p21-highly-expressing senescent cells in vivo. Nat Aging 2021; 1: 962–973

Wang C, Jurk D, Maddick M, Nelson G, Martin-Ruiz C, von Zglinicki T. DNA damage response and cellular senescence in tissues of aging mice. Aging Cell 2009; 8: 311–323
Wang D, Aguilar B, Starr R, Alizadeh D, Brito A, Sarkissian A, Ostberg JR, Forman SJ, Brown CE. Glioblastoma-targeted CD4+ CAR T cells mediate superior antitumor activity. JCI Insight 2018; 3: e99048, 99048

Weiss T, Weller M, Guckenberger M, Sentman CL, Roth P. NKG2D-Based CAR T Cells and Radiotherapy Exert Synergistic Efficacy in Glioblastoma. Cancer Res 2018; 78: 1031–1043

Wiley CD, Campisi J. The metabolic roots of senescence: mechanisms and opportunities for intervention. Nat Metab 2021; 3: 1290–1301

Wiley CD, Flynn JM, Morrissey C, Lebofsky R, Shuga J, Dong X, Unger MA, Vijg J, Melov S, Campisi J. Analysis of individual cells identifies cell-to-cell variability following induction of cellular senescence. Aging Cell 2017; 16: 1043–1050

Woischke C, Blaj C, Schmidt EM, Lamprecht S, Engel J, Hermeking H, Kirchner T, Horst D. CYB5R1 links epithelial-mesenchymal transition and poor prognosis in colorectal cancer. Oncotarget 2016; 7: 31350–31360

Xu P, Wang M, Song W-M, Wang Q, Yuan G-C, Sudmant PH, Zare H, Tu Z, Orr ME, Zhang B. The landscape of human tissue and cell type specific expression and co-regulation of senescence genes. Mol Neurodegener 2022; 17: 5

Xu T, Wang C, Wang X, Wang E, Wang B, Sun M. A novel TREM1/DAP12-based multiple chain CAR-T cell targets PTK7 in ovarian cancer therapy. Med Oncol 2023; 40: 226

Yang D, Sun B, Li S, Wei W, Liu X, Cui X, Zhang X, Liu N, Yan L, Deng Y, Zhao X. NKG2D-CAR T cells eliminate senescent cells in aged mice and nonhuman primates. Sci Transl Med 2023; 15: eadd1951

Yun J, Hansen S, Morris O, Madden DT, Libeu CP, Kumar AJ, Wehrfritz C, Nile AH, Zhang Y, Zhou L, Liang Y, Modrusan Z, Chen MB, Overall CC, Garfield D, Campisi J, Schilling B, Hannoush RN, Jasper H. Senescent cells perturb intestinal stem cell differentiation through Ptk7 induced noncanonical Wnt and YAP signaling. Nat Commun 2023; 14: 156

Zarei M, Abdoli S, Farazmandfar T, Shahbazi M. Lenalidomide improves NKG2D-based CAR-T cell activity against colorectal cancer cells invitro. Heliyon 2023; 9: e20460

Zhang H, Zhao P, Huang H. Engineering better chimeric antigen receptor T cells. Exp Hematol Oncol 2020a; 9: 34

Zhang L, Pitcher LE, Prahalad V, Niedernhofer LJ, Robbins PD. Targeting cellular senescence with senotherapeutics: senolytics and senomorphics. FEBS J 2023; 290: 1362–1383

Zhang P, Kishimoto Y, Grammatikakis I, Gottimukkala K, Cutler RG, Zhang S, Abdelmohsen K, Bohr VA, Misra Sen J, Gorospe M, Mattson MP. Senolytic therapy

alleviates Aβ-associated oligodendrocyte progenitor cell senescence and cognitive deficits in an Alzheimer's disease model. Nat Neurosci 2019; 22: 719–728

Zhang R, Chen W, Adams PD. Molecular dissection of formation of senescence-associated heterochromatin foci. Mol Cell Biol 2007; 27: 2343–2358

Zhang T, Lemoi BA, Sentman CL. Chimeric NK-receptor-bearing T cells mediate antitumor immunotherapy. Blood 2005; 106: 1544–1551

Zhang W, Gou P, Dupret J-M, Chomienne C, Rodrigues-Lima F. Etoposide, an anticancer drug involved in therapy-related secondary leukemia: Enzymes at play. Transl Oncol 2021a; 14: 101169

Zhang X, Shao S, Li L. Characterization of Class-3 Semaphorin Receptors, Neuropilins and Plexins, as Therapeutic Targets in a Pan-Cancer Study. Cancers (Basel) 2020b; 12: 1816

Zhang Y, Liu T, Wang J, Zou B, Li L, Yao L, Chen K, Ning L, Wu B, Zhao X, Wang D. Cellinker: a platform of ligand-receptor interactions for intercellular communication analysis. Bioinformatics 2021b; btab036

Zhu Y, Tchkonia T, Pirtskhalava T, Gower AC, Ding H, Giorgadze N, Palmer AK, Ikeno Y, Hubbard GB, Lenburg M, O'Hara SP, LaRusso NF, Miller JD, Roos CM, Verzosa GC, LeBrasseur NK, Wren JD, Farr JN, Khosla S, Stout MB, McGowan SJ, Fuhrmann-Stroissnigg H, Gurkar AU, Zhao J, Colangelo D, Dorronsoro A, Ling YY, Barghouthy AS, Navarro DC, Sano T, Robbins PD, Niedernhofer LJ, Kirkland JL. The Achilles' heel of senescent cells: from transcriptome to senolytic drugs. Aging Cell 2015; 14: 644–658

Zingoni A, Molfetta R, Fionda C, Soriani A, Paolini R, Cippitelli M, Cerboni C, Santoni A. NKG2D and Its Ligands: "One for All, All for One." Front Immunol 2018; 9: 476

9. Acknowledgements

First, I would like to express my sincerest gratitude to my supervisor, Dr. Dan Ehninger, for giving me the opportunity to work in his research group and for providing consistent encouragement and support throughout my PhD. I would also like to thank Prof. Johannes Oldenburg for acting as my second examiner, as well as Prof. Gabor Petzold and Prof. Sybille Krauß for acting as my dissertation committee.

Secondly, my sincerest thanks go to the current and former members of the “Translational Biogerontology lab” for their friendship, constant help, support, and advice. I am particularly grateful to Dr. Avadh Kumar, who mentored me in the “CAR-T cell” work. He has patiently taught me, allowing me to grow independent in formulating my own ideas. Special thanks also go to Dr. Kan Xie and Dr. Kristina Schaaf, who guided and assisted me with the mouse work, and provided valuable suggestions and feedback to improve my study. I am also grateful to Dr. Enzo Scifo for teaching me proteomics and guiding me on the proteomics project, and to Ms. Ting Liu for her consistent support throughout the proteomics project. My gratitude extends to all of them for their insightful discussions throughout my study and for reviewing the manuscripts. Furthermore, My PhD career would not have been possible without the financial support from the China Scholarship Council (CSC).

I also express my gratitude to the other research groups. To Dr. Armin Ehninger at AvenCell for his valuable technical and scientific support for the “CAR-T cell” project. To AG Beyer and AG Salomoni at DZNE for providing me the opportunity to work on the FACS and Incucyte, respectively. My thanks also go to the animal caretakers, the LMF at DZNE, as well as the coordinators of BIGS Neuroscience.

And finally, I have reached this point in my life, all thanks to the deep love and unwavering support from my family and my friends. They are crucial in helping me through pivotal life decisions, recover from my low points, and share joy in even the smallest of my achievements!

10. List of publications

Parts of this thesis are based on the following publications:

Deng Y, Liu T, Scifo E, Li T, Xie K, Taschler B, Morsy S, Schaaf K, Ehninger A, Bano D, Ehninger D. Analysis of the senescence-associated cell surfaceome reveals potential senotherapeutic targets. Aging Cell. 2024 Dec;23(12):e14312. DOI: 10.1111/acel.14312. Epub 2024 Sep 3.

Deng Y, Kumar A, Xie K, Schaaf K, Scifo E, Morsy S, Li T, Ehninger A, Bano D, Ehninger D. Targeting senescent cells with NKG2D-CAR T cells. Cell Death Discov. 2024 May 4;10(1):217. DOI: 10.1038/s41420-024-01976-7.

Other publications:

Xie K, Fuchs H, Scifo E, Liu D, Aziz A, Aguilar-Pimentel JA, Amarie OV, Becker L, da Silva-Buttkus P, Calzada-Wack J, Cho YL, **Deng Y**, Edwards AC, Garrett L, Georgopoulou C, Gerlini R, Hölter SM, Klein-Rodewald T, Kramer M, Leuchtenberger S, Lountzi D, Mayer-Kuckuk P, Nover LL, Oestereicher MA, Overkott C, Pearson BL, Rathkolb B, Rozman J, Russ J, Schaaf K, Spielmann N, Sanz-Moreno A, Stoeger C, Treise I, Bano D, Busch DH, Graw J, Klingenspor M, Klopstock T, Mock BA, Salomoni P, Schmidt-Weber C, Weiergräber M, Wolf E, Wurst W, Gailus-Durner V, Breteler MMB, Hrabě de Angelis M, Ehninger D. Deep phenotyping and lifetime trajectories reveal limited effects of longevity regulators on the aging process in C57BL/6J mice. Nat Commun. 2022 Nov 11;13(1):6830. DOI: 10.1038/s41467-022-34515-y.

Deng Y, Zheng M, He L, Yang J, Yu G, Wang J. A Head-to-Head Comparison of Percutaneous Mastoid Electrical Stimulator and Supraorbital Transcutaneous Stimulator in the Prevention of Migraine: A Prospective, Randomized Controlled Study. Neuromodulation. 2020 Aug;23(6):770-777. DOI: 10.1111/ner.13127. Epub 2020 Feb 25.

Deng Y, Wang J, He G, Qu F, Zheng M. Mobilization of endothelial progenitor cell in patients with acute ischemic stroke. Neurol Sci. 2018 Mar;39(3):437-443. DOI: 10.1007/s10072-017-3143-y. Epub 2017 Nov 16.

Deng Y, He L, Yang J, Wang J. Serum D-dimer as an indicator of immediate mortality in patients with in-hospital cardiac arrest. Thromb Res. 2016 Jul;143:161-5. DOI: 10.1016/j.thromres.2016.03.001. Epub 2016 Mar 5.

Deng Y, Lu X, Wang L, Li T, Ding Y, Cao H, Zhang Y, Guo X, Yu G. Curcumin inhibits the AKT/NF-κB signaling via CpG demethylation of the promoter and restoration of NEP in the N2a cell line. AAPS J. 2014 Jul;16(4):649-57. DOI: 10.1208/s12248-014-9605-8. Epub 2014 Apr 23.